Spring 4-22-2009

Exchange Coupling at Cobalt/ Nickel Oxide Interfaces

Andrew G. Baruth
University of Nebraska at Lincoln, Andrew.Baruth@huskers.unl.edu

Baruth, Andrew G., "Exchange Coupling at Cobalt/ Nickel Oxide Interfaces" (2009). *Theses, Dissertations, and Student Research: Department of Physics and Astronomy*. 5.
http://digitalcommons.unl.edu/physicsdiss/5

EXCHANGE COUPLING AT COBALT/ NICKEL OXIDE INTERFACES

by

Andrew Gerald Baruth

A DISSERTATION

Presented to the Faculty of

The Graduate College at the University of Nebraska

In Partial Fulfillment of Requirements

For the Degree of Doctor of Philosophy

Major: Physics and Astronomy

Under the Supervision of Professor Shireen Adenwalla

Lincoln, Nebraska

May, 2009

EXCHANGE COUPLING AT COBALT/ NICKEL OXIDE INTERFACES

Andrew Gerald Baruth, Ph.D.

University of Nebraska, 2009

Adviser: Shireen Adenwalla

Spin arrangement at interfaces in layered magnetic materials is of vital importance to the emerging field of spintronics. Knowledge of how and why the interfacial spins behave in a certain way will aid in the development of future magnetic-based memories.

Much exploration has taken place in the interlayer exchange coupling (IEC) of ferromagnetic heterostructures with in-plane anisotropy. Only recently has it become apparent that to achieve the goals of increased areal density in magnetic memory a push for exploring magnetic materials with perpendicular magnetic anisotropy (PMA) must occur. An interesting and promising candidate for such a magnetic system is [Co/Pt]/NiO/[Co/Pt], where two [Co/Pt] multilayers with PMA are separated by a thin, insulating, antiferromagnetic NiO layer and display oscillatory coupling with NiO thickness. This magnetic heterostructure displays an entirely new IEC where the Ni spins within the NiO layer cant in concert with the adjacent [Co/Pt] layers, causing the periodicity of the oscillatory coupling to coincide with the NiO antiferromagnetic ordering parameter. The strength and sign of this coupling, either positive (favoring parallel alignment) or negative (favoring anti-parallel alignment), can be tuned with slight

changes in the NiO layer thickness. The origin of the oscillatory IEC was investigated using advanced microscopy and spectroscopy techniques.

For antiferromagnetically coupled [Co/Pt] layers, the competition between magnetostatic coupling and IEC gives rise to a region of overlapping domains (resulting in a ferromagnetically coupled stripe). Discovered with high resolution magnetic force microscopy and quantitatively modeled with micromagnetic simulation, the width of this overlap region scales inversely with the IEC.

Heterostructures of Co/NiO/[Co/Pt], where the Co ([Co/Pt]) has in-plane (out-of-plane) anisotropy, allow for isothermal tuning of the hysteresis loop shift along the applied field axis at room temperature, as well as display a greatly enhanced blocking temperature (increase of more than 175K). The presence of the [Co/Pt] multilayer with PMA is responsible for the enhancement. In addition, these structures display temperature dependent exchange bias training effects, which have been successfully modeled using a phenomenological thermodynamic approach.

Acknowledgments

There are many friends, colleagues and family that I would like to thank for their continued support and guidance throughout my graduate school experience.

First and foremost, I would like to express my sincere appreciation to my adviser, Professor Shireen Adenwalla. Not only did she give important encouragement at the start of my graduate career that kept me focused on what I truly wanted out of my experience, but she continues to be a guide and support as both a friend and role model. I have enjoyed our discussions over the past 6 years and am grateful for her patient training.

I would like to thank Professor Evgeny Tsymbal, Professor Christian Binek, Professor Jeff Shield and Dr. David Keavney for serving on my supervisory committee. Their thoughtful and critical reading of this dissertation is appreciated.

Specifically, I would like to thank Dr. David Keavney for his guidance and patience while I was working at the Advanced Photon Source. He has continually gone out of his way to better my understanding of not only the equipment but also the physics involved. I have fond memories of our late-night beamline discussions (those who have worked on a beamline will understand) and it was while working with him during my first APS visit that I knew, for certain, that I wanted to be an experimental physicist. Without his dedicated support and gifting of beam time, the results of Chapter 3 would not have been possible. In addition, I would like to thank Professor Evgeny Tsymbal, and his students, Dr. J. D. Burton and Ms. Karolina Janicka, for taking time and energy to guide a wandering experimentalist and for providing insight into projects that would likely have been lost without their thoughtful assistance, in particular the theoretical results found in Chapters 3 and 4.

I owe a huge debt of gratitude to Professor Sy-Hwang Liou, with help from his former student, Dr. Lu Yuan, for the use of his Magnetic Force Microscope, and the use of his beautiful tips. The brilliant images that came out of his lab made the physics I was interested in easy to sell to others. Check out Chapters 3, 4 and 5; the MFM images are truly a work of art and they would not have been possible without his assistance and equipment.

As for my research group, I would like to thank past and current members: Mr. David Kim, Mr. Manuel Diaz, Dr. Marcus Natta, Mr. Dan Williams, Mr. Cody Mart, Mr. Abhijit Mardana, Mr. Sam Davis, Dr. Ellen Day and Ms. Nina Hong. You've all had an impact on my graduate experience both individually and collectively.

In addition to those previously mentioned, I would also like to thank the following people for helpful discussions, support, and in some cases being a useful study buddy: Dr. Vicki Plano Clark, Dr. Andrei Sokolov, Mr. Brian Jones, Professor Roger Kirby, Dr. Steven Michalski, Professor Stephen Ducharme, Dr. Lee Robertson, Dr. Lanping Yue, Mr. Tom George, Mr. Shawn Hilbert, Mr. Kayle DeVaughan, Mr. Shawn Langan, Mr. Srinivas Polisetty, Mr. Stephen Rosenboom, Mr. Dale Johnston, Dr. Anthony Caruso, Dr. David Wisbey, Dr. Timothy Reece, Dr. Dave Schmitter and Dr. Brett Barwick.

Special thanks goes to the support staff that made my life run more smoothly. For help with instrumentation – Michael J. Jensen, Les Marquart, Keith A. Placek, Pat Pribil and Robert L. Rhynalds; electronics – Dr. John R. Kelty and Brian Farleigh; and support management – Theresa Sis, Kay Haley, Jenny Becic, Joyce McNeil and Patty Christen.

For encouraging me to attend graduate school in physics and guiding me down this path I enjoy so much, I owe special appreciation to Dr. Mark Plano Clark and Dr. Christopher D. Wentworth of Doane College.

The work presented in this dissertation was supported by the National Science Foundation (grants Nos. MRSEC DMR-0213808 and 0820521 and DMR-0203359), the Nebraska Research Initiative and Seagate Research. Use of the Advanced Photon Source was supported by the U.S. Department of Energy, Office of Science, Office of Basic Energy Sciences, under Contract No. W-31-109-ENG-38.

On a more personal note, nobody told me that when I chose to go into experimental physics it would be so advantageous to make friends with a theorist, but it has proven to be a very wise decision. With that, I owe a vast amount of appreciation to my good friend Dr. J. D. Burton. Not only has our friendship inspired some beautiful physics, but he has always been a huge source of support, guidance and the often needed study break.

Finally, but above all else, I dedicate this work to my family. For my parents and brothers, I'll always remember the 'Baruth Rule'… that it is the job of the teachers to answer all of your questions and that I should never be afraid to ask them. They have always inspired me to keep asking questions and given me the courage to seek out answers. It is that attitude that has brought me to this day. For this loving guidance and support, I am grateful. For my wife Becky, I never would have achieved this without her love and support. As my guide, my rock, my editor (yes, she reads all of my papers – including this entire dissertation) and my wife, she has inspired me to not only be better at my career, but also to be the best all-around person I could be. With the addition of our son Ryan, she has given me a beautiful reminder of why I’ve worked so hard. She has encouraged me, whatever the decision, and has always been there for me when I needed it most. For that, and many other reasons, I love you Becky and Ryan and I am so thankful for you.

Contents

List of Figures x

List of Tables xxvii

Chapter 1: Introduction 1

1.1 Coupling Across an Interlayer 2

1.2 Exchange Bias 13

1.2(a) Exchange Field 15

1.2(b) High Field Rotational Hysteresis 16

1.2(c) Enhanced Coercivity 17

1.2(d) Asymmetric magnetization reversal 17

1.2(e) Exchange Bias Training Effect 22

1.3 NiO Crystalline and Magnetic Structure 25

1.4 References 28

Chapter 2: Sample Preparation and Characterization Techniques 38

2.1 Magnetron Sputtering 38

2.2 Photolithography 43

2.3 X-ray Diffraction 49

2.4 Magneto-Optic Kerr Effect (MOKE) 60

2.4a Longitudinal MOKE (LMOKE) 61

2.4b Transverse MOKE (TrMOKE) 61

2.4c Polar MOKE (PMOKE) 61

2.4d MOKE with PEM Derivation 63

2.5 Magnetic Force Microscopy (MFM) 67

2.6 X-ray Magnetic Circular Dichroism (XMCD) and XMCD-Photoemission Electron Microscopy (PEEM) 70

2.6a X-ray Absorption Spectroscopy (XAS) 71

2.6b XMCD 73

2.6c XMCD-PEEM 75

2.7 Alternating Gradient Force Magnetometry (AGFM) 77

2.8 Neutron Diffraction 79

2.9 References 80

Chapter 3: Origin of Interlayer Exchange Coupling in [Co/Pt]/NiO/[Co/Pt] multilayers studied with XAS, XMCD, and micromagnetic modeling 84

3.1 Introduction 84

3.2 Sample Preparation and Experimental Techniques 87

3.3 XAS and XMCD Measurements at Co and Ni Resonant Energies 92

3.3a XAS 92

3.3b XMCD Hysteresis Loops and Electron Attenuation Length in NiO 94

3.3c Ni Canting 102

3.4. Domain Structures using XMCD-PEEM and MFM 106

3.4a Coincidence of domains in NiO and Co: XMCD-PEEM measurements 106

3.4b Variation in domain size with coupling strength: XMCD PEEM images at Co L_3 edge 108

3.4c MFM images of varying NiO thickness 111

3.5 Temperature Dependence and Oxidation/Reduction Reactions at the Interface .. 117

3.5a Temperature induced irreversibility 117

3.5b Temperature dependence of the minor loop shift 120

3.6 Conclusions 125

3.7 Acknowledgements 127

3.8 References 127

Chapter 4: Domain overlap in exchange-coupled [Co/Pt]/NiO/[Co/Pt] multilayers 132

4.1 Introduction 132

4.2 Sample Preparation and Experimental Techniques 133

4.3 Experimental Results and Discussion 136

4.4 Theoretical Analysis of Domain Overlap 138

4.5 Conclusions 143

4.6 Acknowledgments 143

4.7 References 143

Chapter 5: Domain size and structure in exchange-coupled [Co/Pt]/NiO/[Co/Pt] multilayers 145

5.1 Introduction 145

5.2 Sample Preparation and Experimental Techniques 146

5.3 Bulk Magnetometry and MFM Measurements 147

5.4 Discussion of Domain Size versus Coupling 152

5.5 Discussion of Domain Size for weak Interlayer Exchange Coupling 154

5.6 Conclusion 158

5.7 Acknowledgements 159

5.8 References 159

Chapter 6: Enhanced blocking temperature and isothermal control of hysteresis loop shifts in Co/NiO/[Co/Pt] heterostructures with orthogonal easy axes 161

6.1 Introduction 161

6.2 Experimental Techniques 162

6.3 Loop Shifts at Room Temperature and Below 164

6.4 Discussion 170

6.5 Conclusion 176

6.6 Acknowledgements 176

6.7 References 176

Chapter 7: Temperature and set field dependence of exchange bias training effects in Co/NiO/[Co/Pt] heterostructures with orthogonal easy axes 180

7.1 Introduction 180

7.2 Experimental Techniques 182

7.3 Measurements of the Training Effect 186

7.4 Conclusion 198

7.5 Acknowledgements 201

7.6 References 201

Selected Presentations 205

Publications 209

List of Figures

Figure 1.1: GMR based spin-valve 3

The structure of a proto-typical spin-valve is given in the upper panel, where the NiFe/Cu/NiFe acts as a giant magneto-resistance (GMR) device and the NiFe/FeMn bilayer is pinned due to exchange bias (EB). In the lower panel, the magnetization curve (a) and relative change in magneto-resistance (b) for Si (NiFe 150Å)/(Cu 26Å)/(NiFe 150Å)/(FeMn (FeMn 100Å)/(Ag 20Å) is given. The field is applied parallel to the exchange bias field created by the FeMn. The current is flowing perpendicular to this direction. (Figure adapted from Ref. 1.5).

Figure 1.2: Oscillatory coupling for metallic interlayers 4

Antiferromagnetic coupling srength of J_{AF} vs t_{Cr} for (211) and (100) oriented Fe(14Å)/Cr(t_{Cr}) supperlattices measured at room temperature (Figure taken from Ref. 1.8).

Figure 1.3: GMR of Fe/Cr superlattices 5

Magnetoresistance of three [(Fe 30Å)/(Cr 9Å)]$_n$ supperlattices at 4.2 K. The current is along [110] and the field is in the layer plane along the current direction (Figure taken from Ref. 1.1).

Figure 1.4: Monotonic decay of coupling for insulating interlayers 6

The variation of the coupling strength J with the insulator MgO thickness. The experimental data is represented by empty squares. The line gives a theoretical estimation of **J** based on the framework of spin-polarized tunneling (Figure taken from Ref. 1.11).

Figure 1.5: TMR of CoFe/Al_2O_3/Co junction 7

Tunneling Magneto-resistance of CoFe/Al_2O_3/Co junction plotted as a function of H in the film plane, at 295 K. Also shown in the variations in the CoFe and Co film resistance. (Figure taken from Ref. 1.4).

Figure 1.6: Temperature dependence of IEC 9

Showing the temperature dependence of interlayer exchange coupling based on the model proposed by Bruno [1.32], decreasing for metals ($T/\sinh T$) and increasing for insulators ($T/\sin T$).

Figure 1.7: XMCD of NiFe/NiO/Co trilayer 11

Element specific hysteresis curves obtained with XMCD for Co (open circles, right-hand y axis) and NiFe (fill squares, left-hand y axis) with the field applied parallel (a) and perpendicular (b) to the Co easy-axis for a (NiFe 10nm)/(NiO 8nm)/(Co 2nm) trilayer. (Figure taken from Ref. 1.46).

Figure 1.8: Slonczeski Proximity Model 12

Illustration of the Slonczewski Proximity Model. For ideal interfaces (left panel), the coupling will oscillate with the number of antiferromagnetic monolayers, *i.e.* odd (even) layers leading to ferromagnetic (antiferromagnetic) coupling. For real interfaces with roughness (right panel), the magnetostatic energy density at the edge of the roughness (pink circles) is very large when the ferromagnetic layer is colinear with the antiferromagnet. To reduce this energy, the ferromagnetic easy axis rotates 90° with respect to the antiferromagnet axis.

Figure 1.9: Illustration of Exchange Bias 14

Illustration of exchange bias. Easy axis magnetization loops of a ferromagnetic (FM) film (left), a FM film grown on an antiferromagnet (AFM) (middle), and a FM/AFM bilayer prepared in a field cool $\boldsymbol{H}_{\text{set}}$ (right). In the right structure the ferromagnet is biased with a field $\boldsymbol{H}_{\text{EB}}$. The bias field points to the left, while the preferred direction of the ferromagnetic magnetization points to the right.

Figure 1.10: Torque curves on Co/CoO particles 16

Torque curves on CoO coated Co particles cooled in a field to 77 K, where θ is the angle between the cooling-field axis and the direction of the measureing field. Curves (a) and (b) are for rotations of decreasing and increasing θ, respectively. (Figure taken from Ref. 1.47)

Figure 1.11: Illustration of uncompensated and compensated AFM interfaces 18

Illustrations for uncompensated (left panel) and compensated (right panel) interfaces between ferromagnetic (blue) and antiferromagnetic (yellow) bilayers.

Figure 1.12: Atomic and magnetic structure of NiO 25

An eight unit cell magnetic diagram of face-centered cubic NiO. The Ni^{2+} spins reside at the cubic and face-centered sites and point along the $\langle 11\bar{2} \rangle$ axes (Figure taken from Ref. 1.85).

Figure 1.13: NiO domain walls 27

Description of domain walls in NiO. (a) There are three equivalent $\langle 11\bar{2} \rangle$ easy axes in the {111} planes (S domains). (b) T walls which are induced by the contractions along different $\langle 111 \rangle$ azes. The solid lines trace the spins in the ferromagnetic {111} planes. (c) $S_{\perp}$ domain walls in which the spin rotation occurs within the ferromagnetic {111} planes. (d) $S_{\parallel}$ domain walls in which the spin rotation occurs between adjacent {111} planes.

Figure 2.1.1: Magnetron sputtering diagram..40

A cross sectional schematic diagram of the magnetron sputtering process. The purple background represents the presence of the plasma made up of free electrons and Ar^+ ions.

Figure 2.1.2: Schematic of theAJA ATC-2000-V..42

Schematic of the AJA ATC-2000-V system with Phase II control, having both a load lock and main chamber separated by a gate valve. The guns are in a confocal setup with adjustable angle. The substrate holder can rotate a full 360° and also has a temperature stage (~600°C max). The Cassette holder is described in the text. The substrate is transferred from the Load Lock to the Main Chamber and back via the Transfer Arm (Figure modified from stock AJA schematic)

Figure 2.2.1: Photolithography lift-off process 45

Visual demonstration of the steps in the photolithography lift-off process using a two layered photo resist approach. Description of each step can be found in the text.

Figure 2.2.2 Photolithography etching process 47

Visual demonstration of the steps in the photolithography etching process using a single layered photo resist approach. Description of each step can be found in the text.

Figure 2.3.1: Bragg diffraction 51

Schematic of the diffraction by a crystal, which can be considered a set of parallel planes separated by a distance *d*. For an incident angle of θ for the incoming X-ray, the path difference between successive planes is given by $2d\sin\theta$. If this path difference in equal to $n\lambda$ constructive interference will occur.

Figure 2.3.2: Simple cubic lattice showing (111) Miller indices 52

Simple cubic lattice showing the Miller (111) indices for the shown plane coincide with the normal vector <111> to this plane. The basis vectors a_1, a_2 and a_3 represent the 3 simple cubic lattice parameters. For a simple cubic lattice the magnitude for each is the same and the directions are all orthogonal.

Figure 2.3.3: Snell's law...56

Refraction of X-rays at the interface between two media of different refractive indices, with $n < n_0$. Since the velocity is higher in the second medium, the angle of refraction θ_t is less than the angle of incidence θ_i; that is, the ray in the lower-index medium is further away from the normal (notice that the angle convention is different from the traditional explanation of Snell's law). This implies that there is a critical incident angle, where any incidence at an angle below this angle will result in total external reflection.

Figure 2.4.1: MOKE configurations..........60

Three MOKE configurations – Longitudinal, Transverse and Polar, where the red arrows represent the propagation direction of the light and the black arrows represent the axis in which the external magnetic field is applied.

Figure 2.4.2: Experimental configuration for longitudinal MOKE..........62

Experimental configuration for longitudinal MOKE (similar for perpendicular MOKE if the applied field H was out of the page). The light passes from the laser through the polarizer at either 0 or 90°, depending on whether the user wants **s** or **p** polarization. The light is then reflected from the magnetic sample surface with the addition of a polarization rotation θ_k and change in ellipticity ε_k. It then passes through the photoelastic modulator and another polarizer at 45° before it is measured with a photodiode.

Figure 2.5.1: Schematic of MFM..........67

Schematic view of magnetic force microscopy for films with in-plane and out-of-plane easy axes.

Figure 2.6a.1: X-ray Absorption Spectroscopy..........72

X-ray Absorption Spectra for Co and Ni about the L_3 and L_2 peaks. The metallic Co and Ni have two broad peaks, while the oxides CoO and NiO show multiplet structure in both the L_3 and L_2 peaks [Figure taken from J. Stöhr, Ref 2.13].

Figure 2.6b.1: X-ray magnetic circular dichroism 74

(a) Electronic transitions in conventional L-edge X-ray absorption, (b) and (c) X-ray magnetic circular dichroism, illustrated in a one-electron model. The transitions occur from the spin orbit split 2p core shell to empty conduction band states above the Fermi level. In conventional X-ray absorption the transition intensity measured as the white line intensity L_3+L_2 is proportional to the number of d holes, N. By use of circularly polarized X-rays the spin moment (b), and orbital moment (c), can be determined from the dichroic difference intensities A and B, as explained in the text [Figure taken from Reference 2.15].

Figure 2.6c.1: Photoemission electron microscopy 76

Magnetic imaging by means of PEEM. A layer in the sample is selected by tuning the X-ray energy to the desired element. X-ray polarization contrast at an absorption peak is used for imaging contrast. The local electron yield from a sample region, imaged by PEEM, depends on the relative orientation of the magnetic direction or axis and the polarization [Figure taken from J. Stöhr, Ref. 2.13].

Figure 2.7.1: Alternating Gradient Force Magnetomter 78

Schematic of the Alternating Gradient Force Magnetometer.

Figure 3.1:..89

a) Room temperature XAS spectra at the Ni and Co $L_{3,2}$ resonances indicate no evidence of multiplet splitting at the Co $L_{3,2}$ peaks, as would be expected if CoO were present, and the Ni L_2 peak reveals a doublet splitting, as expected for Ni^{2+} in NiO. b) The major and minor hysteresis loops at room temperature for a sample with a NiO thickness of 8Å, which was measured using polar MOKE. For measurement of the minor loop a large field was applied to saturate the sample; the field was then decreased until the top [Co/Pt] multilayer reversed. Then the field was again increased to complete the loop, during this entire loop the bottom [Co/Pt] multilayer does not switch. c) The room temperature minor loop shift is a measure of the interlayer exchange coupling, thus the variation in coupling with NiO thickness is given. The coupling oscillates with NiO thickness from antiferromagnetic to ferromagnetic coupling.

Figure 3.2 96

a) Element-specific magnetization loops for Co and Ni taken with X-ray magnetic circular dichroism in total electron yield mode at 175K on a ferromagnetically coupled, series 2 sample with a 10Å thickness of NiO. b) Possible NiO spin configuration for a ferromagnetically coupled sample in the *antiferromagnetic* state (①) and *ferromagnetic* state (②), leading to the net Ni out-of-plane magnetization presented in a) – See section 3.3C in the text for details on exchange coupling at the Co/NiO interface. c) Element-specific magnetization loops for Co and Ni taken with X-ray magnetic circular dichroism in total fluorescence yield mode at 154K on an antiferromagnetically coupled, series 1 sample with a 12Å thickness of NiO. d) Possible NiO spin configuration for an antiferromagnetically coupled sample in the *antiferromagnetic* state (③) and *ferromagnetic* state (④), leading to the net Ni out-of-plane magnetization presented in c).

Figure 3.3 99

Measurement of the secondary electron attenuation length in NiO. The total electron yield signal arising from the Co L_3 resonance on a $[Co/Pt]_3/NiO/Cu$ sample is measured at room temperature, where the NiO thickness varies with position. The exponential fit indicates an attenuation length for secondary electrons in NiO of 3.9Å. The inset shows the profile of the NiO wedge, characterized with low-angle x-ray reflectivity.

Figure 3.4 103

XMCD signal at the Ni L_3 resonance for the 8, 10, 11 and 12Å samples, taken at 175K. The integral over this signal gives a measure of the net out-of-plane magnetization in the antiferromagnetic NiO. Inset: The magnitude of the integral over the dichroism signal versus the magnitude of the coupling strength for the given sample. A larger out-of-plane signal arises for the AFM coupled samples when compared to the FM coupled sample.

Figure 3.5 107

X-ray magnetic circular dichroism – photoemission electron microscopy images taken at room temperature at the Co and Ni L_3 resonances on a virgin, antiferromagnetically coupled, 8Å sample from series 2. This technique images ferromagnetic domains in both the top Co and buried NiO layers. There is exact coincidence in the domain structure of the Co and NiO. Arrows indicate the position of coincident domains.

Figure 3.6 110

XMCD-PEEM images taken at room temperature at the Co L_3 resonance on virgin samples representing various NiO and Pt thicknesses. Due to attenuation, this measurement is only sensitive to the top Co layers. The top two images represent two Pt thicknesses (5.1 and 11.8Å), where the NiO thickness was set to 8Å. The lower 5 images represent varying NiO thicknesses (8, 9.5, 10.5, 11 and 12Å). The plot shows the average domain size of these samples as a function of their coupling strength. The average domain size tends to increase with increasing coupling strength, no matter how this variation in coupling is attained (varying NiO or Pt thickness).

Figure 3.7 112

Room temperature MFM images of samples with 8, 10.5, 11 and 12Å NiO thicknesses. The 8 and 12Å samples are antiferromagnetically coupled, up and down domains disappear and only a domain overlap region is observed. The 10.5Å sample is ferromagnetically coupled and only up and down domains are observed. The 11Å is very weakly coupled (slightly antiferromagnetic). The domain overlap that occurs in the antiferromagnetically coupled samples grows with decreasing coupling strength, where the 8Å is the strongest and 12Å is the most weakly coupled sample. The orientation flips from up to down along the overlap to minimize magnetostatic energy.

Figure 3.8 113

The model domain structure for the two [Co/Pt] multilayers. The view is in the plane of the film along the stripe domains. The dimensions are defined in the text.

Figure 3.9 115

The dependence of the equilibrium domain overlap δ on the interlayer exchange coupling J_{IEC}. The open circles are results of the numerical calculation for periodic stripe domains, and the curve calculated directly from Eq. 3.11. Arrows indicate specific values for J_{IEC} as defined in the inset. The closed circles show the measured δ values for the 12 and 8Å samples, as defined in the text. Inset: The variation in the total energy versus the overlap δ for 3 J_{IEC} values (a) 0.015, (b) 0.033 and (c) 0.1 erg/cm^2, where (a) and (b) correspond to the coupling for the 12 and 8Å samples, respectively.

Figure 3.10 118

a) A plot of the room temperature minor loop shift after heating to a specified temperature, indicated on the horizontal axis. This indicates permanent, irreversible changes in the exchange coupling due to heating, where these changes increase with increased heating. b) Low-angle x-ray reflectivity taken on an 8Å sample from series 2 before and after a 468K heating showing minimal change in the multilayer structure due to diffusion and no evidence of increased roughness. The inset of b) shows no change in the intensity of the x-ray diffraction at the NiO fcc(111) peak before, at and after a 468K heating. c) XAS data taken at the Co L_3 resonance before (c) and after (d) heating to 468K. The presence of CoO after heating is evident in (d).

Figure 3.11 122

Interlayer exchange coupling as a function of temperature for the 8 and 12Å samples, which couple antiferromagnetically. Two plots are given for the 8Å sample. The H_{REV} data are the reversible component of the temperature dependence, obtained as explain in the text. The 8 and 12Å samples exhibit a decrease in interlayer exchange coupling with increasing temperature.

Figure 4.1 135

MFM images of coupled Co/Pt multilayers, with different thicknesses of the NiO interlayer corresponding to the IEC values listed. In the images, light colored areas indicate a magnetization out of the page. Each image is 5µm x 5µm in size.

Figure 4.2 137

Representative line scans for the 7.5, 9 and 11.5Å samples. The left panels show the region where the lines scans were performed, the black box indicates the region used for averaging and the red lines indicate the average domain overlap width. Each image is 1.25µm x 1.25µm in size.

The right panel shows the corresponding lines scans, averaged over the region enclosed in the black box. The red arrows indicate the location of the red lines in the left panel and represent the FWHM of the features.

Figure 4.3 139

Magnetostatic energy density for antiparallel-aligned domains with no overlap (a) and with overlap δ (b) for $t = 3$nm, $d = 1$nm, and $\delta = 4$nm.

Figure 4.4 142

Domain overlap width as a function of the coupling strength. Closed circles give the compiled line scan data for all samples. 15nm error bars account for MFM resolution. The solid line indicates the best fit to Eq. 4.2. The fit parameters are discussed in the text. The arrow corresponds to the coupling strength for the 11Å sample.

Figure 5.1 148

Room temperature J_{IEC} values, based on minor loop shifts, are given for a variety of NiO thicknesses along the sample wedge (as indicated in the illustration). Above 8Å NiO thickness, the coupling smoothly oscillates with NiO thickness from antiferromagnetic to ferromagnetic coupling – the coupling disappears below 8Å due to pin-holes. This oscillation in coupling obeys a simple cosine function with an exponential damping.

Figure 5.2 150

MFM images of coupled [Co/Pt] multilayers, with different thicknesses of the NiO layer corresponding to the position along the wedge. The strength of the interlayer exchange coupling listed (in units of merg/cm^2) is based on PMOKE data taken at each position. In the images, light colored areas indicate a magnetization out of the page. Each image is 5 x 5 μm^2 in size.

Figure 5.3 152

Average up domain size is given as a function of $J_{IEC.}$ The average domain size increases monotonically with increased coupling strength. An assumed linear fit is presented, where the minimum domain size (i.e. zero IEC) is found to be 0.19 μm^2. Domain size error bars give an indication of the spread in sizes amongst the various up domains.

Figure 5.4 155

MFM images of weakly coupled [Co/Pt] multilayers, with slightly different thicknesses of the NiO layer corresponding to the position along the wedge. Each image corresponds to a 0.1 mm step along the wedge in the transition region from AFM to FM coupling. The total change in NiO thickness for the entire series is ~0.2Å. In this region, the domain size increases slightly while the structure appears to be consistent. Each image is 5 x 5 μm^2 in size.

Figure 5.5 157

Average up domain size is given as a function of position along the wedge in the vicinity of $t_{NiO} = 11.6Å_.$ The average up domain size increases with the slight increase in FM coupling. Domain size error bars give an indication of the spread in sizes amongst the various up domains.

Figure 6.1 165

In-plane magnetization curves for samples b and c at room temperature. The thin films structures are also indicated. The Co/Pt layer has the expected hard axis s-shaped curve with a non-zero remanence value that is ~26% of saturation. The Co loop is square and is symmetric about the magnetization axis.

Figure 6.2 166

Two minor in-plane, [Co/Pt]/NiO magnetization loops, one from +3.5kOe to -250 Oe and one from +500 Oe to -250 Oe. The asymmetry in the in-plane magnetization increases with increasing set field.

Figure 6.3 168

In-plane exchange bias of the Co/NiO/[Co/Pt] heterostructure as a function of H_{set}, where the structure is indicated in the upper left inset. The H_c for the upper and lower branch is also given; notice the lower branch shows no change until 2.75 kOe, above which the upper and lower branches show equal but opposite changes. Two representative loops taken at different H_{set} are shown in the upper right inset.

Figure 6.4 170

Co loop shift as a function of temperature. The loop shift decreases linearly with temperature, with a T_B of 225 K. The inset shows the hysteresis loop at three representative temperatures (150 - black, 225 - red, 300 K - green)

Figure 7.1 185

(a) A series of ten 250 Oe in-plane magnetization loops of sample A following the application of a 3.5 kOe in-plane set field. Following the initial loop, the [Co/Pt] magnetization displays negligible training effects. (b) Average [Co/Pt] in-plane remanance, M_R, as a function of the set field, H_{set}. M_R increases with increasing H_{set}, saturating at $H_{set} \cong 2.75\,\mathrm{kOe}$. The sample schematic is given in the inset.

Figure 7.2 187

Room temperature training data as a function of set field, H_{set}. The solid symbols represent the Co layer loop shift as a function of loop iteration number. Each colored series represents the corresponding H_{set} before the training data was taken. For $H_{set} \geq 3\,\mathrm{kOe}$, the data are identical for all set fields. The open circles represent the best fit using the L-K theory, described in the text.

Figure 7.3 188

The effect of the set field, H_{set}, on the upper and lower branch coercivities and the loop shift for the initial n=1 (top panel) and the final n=20 (bottom panel) hysteresis loops. For both series, a loop shift is observed that increases with increasing set field until 3 kOe, above which it remains constant. Note that both coercivities continue to increase above $H_{set} = 3\,\mathrm{kOe}$.

Figure 7.4 191

The training effect as a function of temperature. All data were taken after application of an in-plane $\mathrm{H_{set} = 3.5\,kOe}$ at room temperature. The solid symbols correspond to the Co layer loop shift as a function of loop iteration number. Each colored series represents the temperature at which the training data was obtained. The open circles represent the best fit using the L-K theory, described in the text.

Figure 7.5 194

The training effect parameter, γ, as a function of temperature. γ is obtained from fitting eqn. 7.1 to the training data in figure 7.4. The line is a best parameter fit to eqn. 7.2. The fit parameters C and T_B are displayed.

Figure 7.6 196

The training effect parameter, γ, vs. [Co/Pt] in-plane remanance, M_R. γ is obtained from fitting eqn. 1 to the training data in figure 2. The line represents the best fit to eqn. 4, where fitting parameters are described in the text. **Inset**: The black diamonds indicate the relationship between the equilibrium loop shift, H_{eb}^{e}, and M_R. The red line is the best linear fit to the data, giving a slope of $-0.75\,\mathrm{Oe}/\mu\mathrm{emu}$ with an R^2 value of 0.96. The blue triangles show the relationship between the blocking temperature, T_B, and M_R. The blue line is a guide to the eye.

List of Tables

Table 3.1..101

Comparison of expected and experimental TEY ratios from the upper and lower [Co/Pt] multilayers. For details see text.

Chapter 1

Introduction

The exchange interaction occurring at the interface between ferromagnets and antiferromagnets has attracted intense research over several decades. It has led to interesting and important properties including the interlayer exchange coupling of trilayer and superlattice structures as well as exchange bias in bi-layer structures. To date, much of the investigation into these phenomena has occurred on magnetic structures with in-plane easy axes. A push for higher areal densities and hence smaller magnetic elements has led to the need for exploiting magnetic elements with a perpendicular geometry. This thesis presents a study of various heterostructures that exploit the useful properties of the insulating antiferromagnet, NiO, in structures that exhibit perpendicular magnetic anisotropy.

The current interest in exchange bias and interlayer exchange coupling stems primarily from the discovery of the magnetoresistance (MR) associated with both conductive (giant magnetoresistance – GMR) [1.1,1.2] and insulating (tunneling magnetoresistance – TMR) barriers [1.3,1.4]. These phenomena have moved to the forefront of current materials research and have become a staple of modern approaches to spintronics. In general, both approaches utilize the electron spin scattering associated with ferromagnetic electrodes that have either parallel or antiparallel alignment. Spin scattering is typically low (high) in the parallel (antiparallel) case leading to a high (low) conduction or tunneling pathway. Thus, the measured resistance depends on the magnetic state of the ferromagnetic electrode layers. In typical MR-based devices, one ferromagnetic electrode is either a 'harder' magnet or is pinned to an antiferromagnet (*i.e.*

exchange bias) to ensure that it is not easily switched in the presence of a magnetic field. The other ferromagnetic layer, or ‘sensing’ layer, is a ‘soft’ ferromagnetic layer that can switch with very little applied field. Because reading a voltage (or resistance) is easier than measuring stray fields, MR-based devices (referred to as spin-valves) have become the basic principle of operation for hard-drive read heads, allowing for very sensitive measurement of the stray fields corresponding to bits within magnetic hard disks. Beyond using GMR and TMR for hard-drive read heads, spintronic devices based on this phenomena could eventually replace today’s semiconductor electronics due to their ability to exploit the extra degrees of freedom provided by the electron spin.

This thesis is organized as follows: Chapter 1 serves as an introduction into the effects studied; including a brief history of interlayer exchange coupling across a variety of spacer materials, interfacial exchange coupling (*i.e.* exchange bias) and a discussion of NiO atomic and magnetic structure. Chapter 2 describes the experimental methods used to study these effects, including sample preparation and characterization. Finally, Chapters 3-7 describe the various studies performed and primarily stem from published or submitted journal articles.

1.1 Coupling Across an Interlayer

The investigation of the coupling of ferromagnetic films across non-ferromagnetic spacers has resulted in a spectrum of scientific discoveries as well as technologically useful devices (Figure 1.1) [1.5]. The first evidence of antiferromagnetic coupling across a metallic layer was seen in 1986 by Grünberg [1.6]. It was later shown that this coupling was in fact oscillatory with thickness of the interlayer (Figure 1.2) [1.7, 1.8].

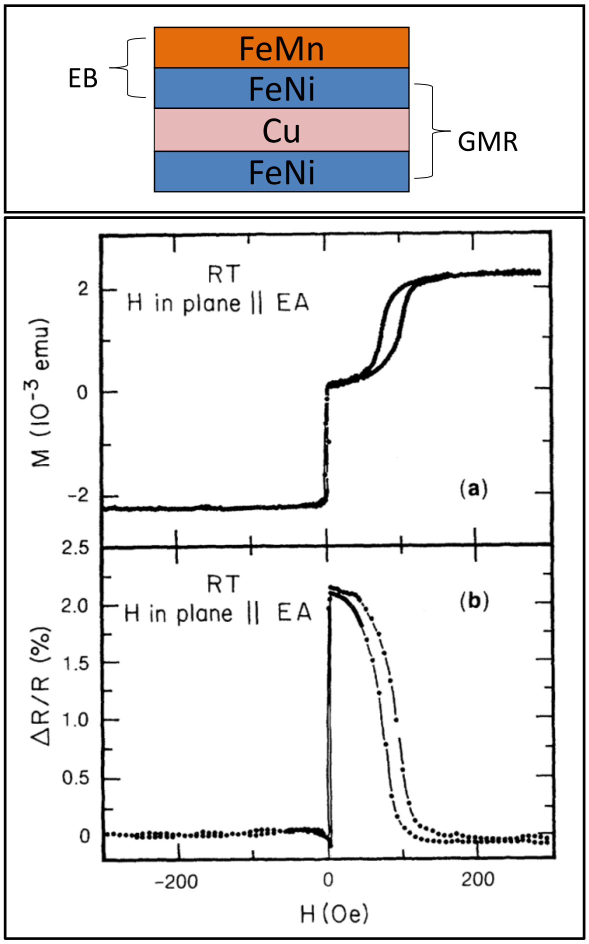

Figure 1.1: GMR based spin-valve

The structure of a proto-typical spin-valve is given in the upper panel, where the NiFe/Cu/NiFe acts as a giant magneto-resistance (GMR) device and the NiFe/FeMn bilayer is pinned due to exchange bias (EB). In the lower panel, the magnetization curve (a) and relative change in magneto-resistance (b) for Si (NiFe 150Å)/(Cu 26Å)/(NiFe 150Å)/(FeMn (FeMn 100Å)/(Ag 20Å) is given. The field is applied parallel to the exchange bias field created by the FeMn. The current is flowing perpendicular to this direction. (Figure adapted from Ref. 1.5).

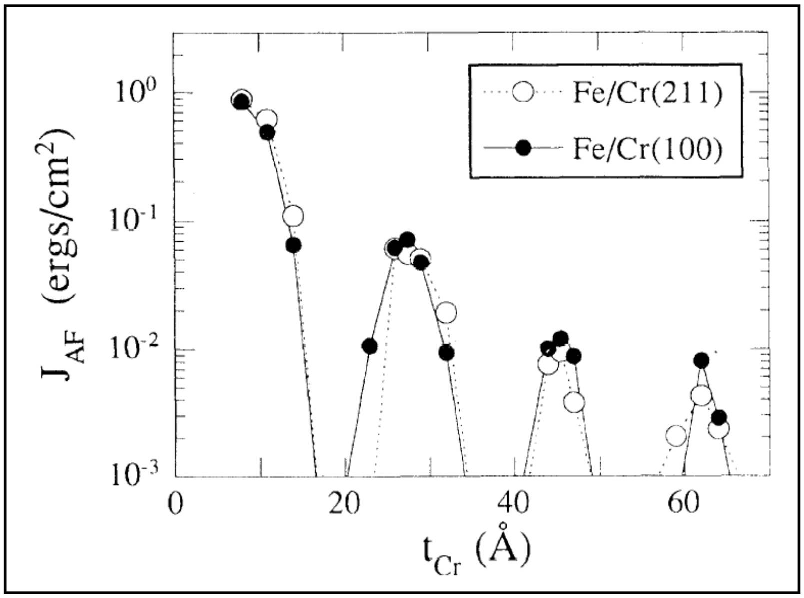

Figure 1.2: Oscillatory coupling for metallic interlayers

Antiferromagnetic coupling srength of J_{AF} vs t_{Cr} for (211) and (100) oriented Fe(14Å)/Cr(t_{Cr}) supperlattices measured at room temperature (Figure taken from Ref. 1.8).

A huge push for the investigation of such structures has been motivated by the discovery of giant magnetoresistance, observed in antiferromagnetically coupled magnetic layers in 1988 by Baibich *et al.* [1.1]. At the time, they were investigating the antiferromagnetic interlayer exchange coupling of ferromagnetic Fe layers separated by Cr layers, and they discovered a magnetoresistance of over 50% at 4.2K (Figure 1.3), which was much larger than any previously observed magnetoresistive effect (usually around 1-2%).

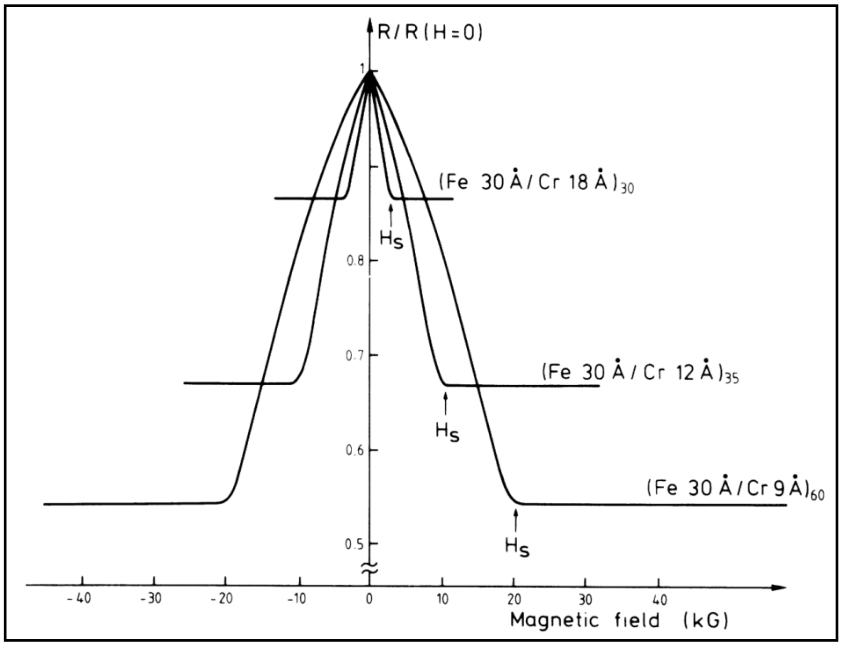

Figure 1.3: GMR of Fe/Cr superlattices

Magnetoresistance of three [(Fe 30Å)/(Cr 9Å)]$_n$ supperlattices at 4.2 K. The current is along [110] and the field is in the layer plane along the current direction (Figure taken from Ref. 1.1).

This was the first magnetoresistive effect that would actually allow one to measure a large, easily detectable signal based on the devices response to an external magnetic field. The oscillatory behavior for transition metal spacers, increasing in strength from 5d to 4d to 3d metals, was later shown to be a general phenomena by S.S. Parkin regardless of crystal structure [1.9]. It was also shown that the interlayer exchange coupling decreased with an increase in temperature.

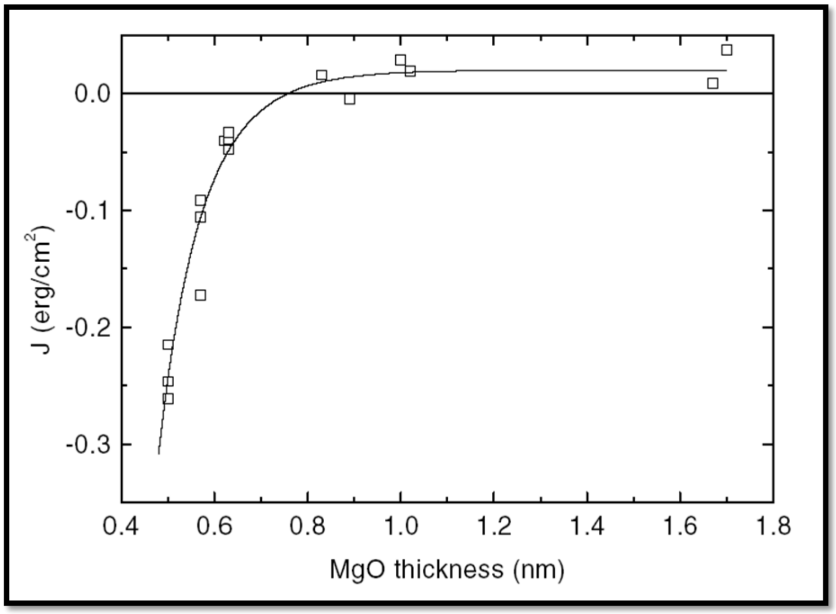

Figure 1.4: Monotonic decay of coupling for insulating interlayers

The variation of the coupling strength J with the insulator MgO thickness. The experimental data is represented by empty squares. The line gives a theoretical estimation of J based on the framework of spin-polarized tunneling (Figure taken from Ref. 1.11).

A subsequent discovery was made by Toscano *et al.*, where they showed the existence of interlayer exchange coupling between two ferromagnetic layers (with in-plane easy axes) across a non-magnetic, non-metallic spacer layer [1.10]. A monotonic decay of the coupling with spacer layer thickness was observed in an Fe/MgO/Fe trilayer many years later (Figure 1.4) [1.11]. In contrast to a metallic spacer, an insulating barrier showed a coupling dependence that increased with increasing temperature. The interest in the insulating barrier has been pushed forward due to the discovery of tunneling magnetoresistance, displayed first by the group of J. Moodera in 1995 [1.4] for an Al_2O_3 tunneling barrier, showing a 24% change in magnetoresistance at 4.2K (Figure 1.5). This value has steadily increased since this discovery, where changes in magnetoresistance of hundreds of percent at room temperature in MgO tunneling barrier structures are now displayed [1.12-1.18].

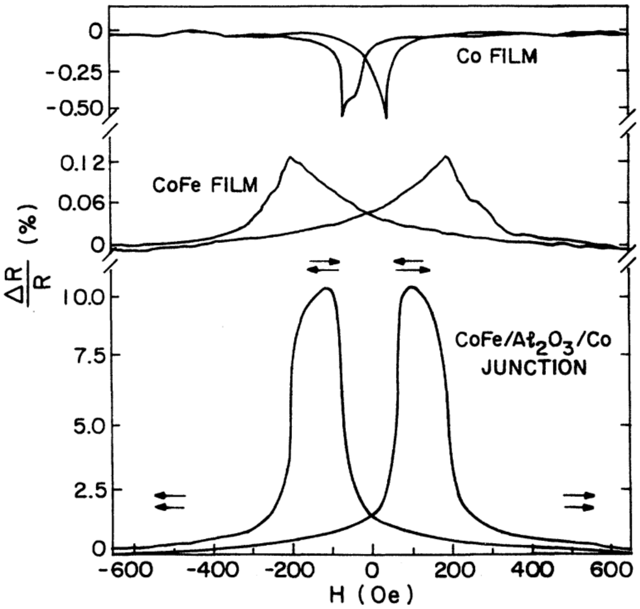

Figure 1.5: TMR of CoFe/Al_2O_3/Co junction

Tunneling Magneto-resistance of CoFe/Al_2O_3/Co junction plotted as a function of H in the film plane, at 295 K. Also shown in the variations in the CoFe and Co film resistance. (Figure taken from Ref. 1.4).

A series of theoretical models have been proposed to explain the interlayer exchange coupling across both metallic and insulating spacer layers. For metallic layers: (1) the RKKY model [1.19-1.22], in which the FM layers are represented by arrays of localized spins interacting with electrons through a contact exchange potential; (2) the free-electron model [1.23-1.26]; (3) the tightbinding model or hole confinement model [1.27-1.28], which considers spin-dependent potential steps; (4) the sd-mixing model

[1.29-1.31]; and (5) the quantum interference model [1.32], in which multiple reflection of electron waves at the ferromagnetic/spacer interfaces and their interference are considered. All these models have related the oscillatory period of interlayer exchange coupling in metals to the Fermi surface of the bulk spacer material in the limit of large spacer thickness.

In Bruno's quantum interference model both metallic and insulating spacers can be treated simultaneously with the introduction of a complex Fermi surface for the insulating layer, where

$$J_{IEC}(T) = -\frac{1}{4\pi^2}\frac{\hbar^2\kappa_F^2}{mD^2}\,\mathrm{Im}\left(\Delta r^2 e^{\,2i\kappa_F D}\right) \times \frac{\frac{2\pi k_B TDm}{\hbar^2\kappa_F}}{\sinh\left(\frac{2\pi k_B TDm}{\hbar^2\kappa_F}\right)}. \tag{1.1}$$

Notice that there is an imaginary part, noted by the Im. k_B is the Boltzmann constant, *D* is the spacer thickness, m is the electron mass, $\hbar$ is the Planck constant, *T* is the temperature and Δr^2 is determined by the sign of the coupling as *r* is the complex electronic reflection amplitude. κ_F is a wavevector determined by the Fermi level ε_F of the ferromagnetic layers and the potential barrier *U* representing the spacer, where

$$\kappa_F = \sqrt{2m(\varepsilon_F - U)/\hbar^2} \tag{1.2}$$

for metallic spacers with $\varepsilon_F > U$ and

$$\kappa_F = i\sqrt{2m(U-\varepsilon_F)/\hbar^2} \tag{1.3}$$

for insulating spacers with $\varepsilon_F < U$. Then, the real κ_F for metallic spacers implies a coupling that oscillates with thickness and decreases with increasing temperature (See Figure 1.6). In contrast, the imaginary κ_F for insulating spacers suggests a non-oscillatory exponential decay of coupling with thickness, because (substituting in an imaginary κ_F)

$$J_{IEC}(T) = -\frac{1}{4\pi^2}\frac{\hbar^2\kappa_F^2}{mD^2}\mathrm{Im}(\Delta r^2 e^{-2\kappa_F D}) \times \frac{\frac{2\pi k_B TDm}{\hbar^2\kappa_F}}{\sin\left(\frac{2\pi k_B TDm}{\hbar^2\kappa_F}\right)}, \tag{1.4}$$

as

$$\frac{ix}{\sinh\ ix} = \frac{x}{\sin\ x}. \tag{1.5}$$

This implies that the coupling will increase with increasing temperature (See Figure 1.6).

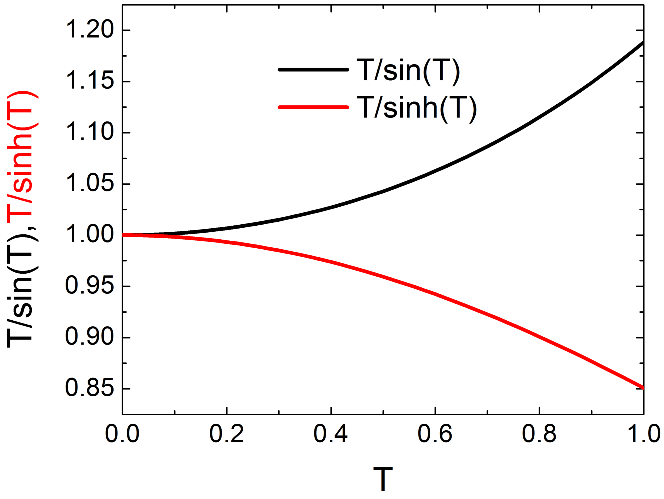

Figure 1.6: Temperature dependence of IEC

Showing the temperature dependence of interlayer exchange coupling based on the model proposed by Bruno [1.32], decreasing for metals ($T/\sinh T$) and increasing for insulators ($T/\sin T$).

This temperature dependence model by Bruno can be understood qualitatively by considering the following. With increasing temperature the smearing of the Fermi surface in metals causes a decrease in the coupling [1.33-1.34]. In insulators, the increase in temperature increases the availability of carriers leading to an increase in the coupling

[1.35]. In addition, the predictions of this model proposed by Bruno have been repeatedly confirmed experimentally [1.36-1.37].

Moving on, the coupling across an antiferromagnetic interlayer with ferromagnetic electrodes having in-plane easy axes will be discussed. For a more detailed review of antiferromagnets and in particular NiO, see Chapter 1.3. In the case of some coupled systems, non-collinear alignment of the two ferromagnetic layers was observed. Due to the presence of this non-collinear alignment it was necessary to introduce a biquadratic coupling term into the energy equation of the system. This approach could phenomenologically reproduce the non-collinear coupling, thus several models were proposed [See, for instance, Ref 1.38, and references therein]. However, when the spacer layer is antiferromagnetic, both the spins within the ferromagnetic layers and the spins within the antiferromagnetic layer must be considered [1.39-1.40]. This potentially leads to coupling that occurs where the angle between the two ferromagnetic magnetizations will vary depending on the nature of the spin structure in the antiferromagnet.

Early studies on Mn [1.41,1.42] and NiO [1.43] interlayers showed a 90° interlayer exchange coupling, as expected from the Slonczewski’s Proximity Model [1.39]. In addition, studies with FeMn, showed a variety of angles between the two ferromagnetic magnetization directions dependent on the FeMn thickness [1.44,1.45]. The 90° coupling for a NiO spacer was shown unambiguously with the use of X-ray Magnetic Circular Dichroism (see Chapter 2.6 for a review on XMCD) on a Co/NiO/NiFe structure [1.46]. In this structure, the NiFe layer grown on a Cu seed layer has no in-plane anisotropy, *i.e.* permalloy is a very soft magnet. The NiO was then sputtered at an oblique angle, which is known to then create an in-plane uniaxial anisotropy in the subsequently sputtered Co layer with the easy-axis of magnetization in the direction perpendicular to the plane of incidence of the sputtered NiO. Although the native NiFe layer had no in-plane anisotropy as grown on Cu, after growth of the NiO and Co layers one can see a well defined in-plane easy axis and hard axis, dependent on the measurement direction. These easy and hard directions, as indicated by the squareness of the hysteresis loops, are at 90° to those seen for the Co layer (See Figure 1.7).

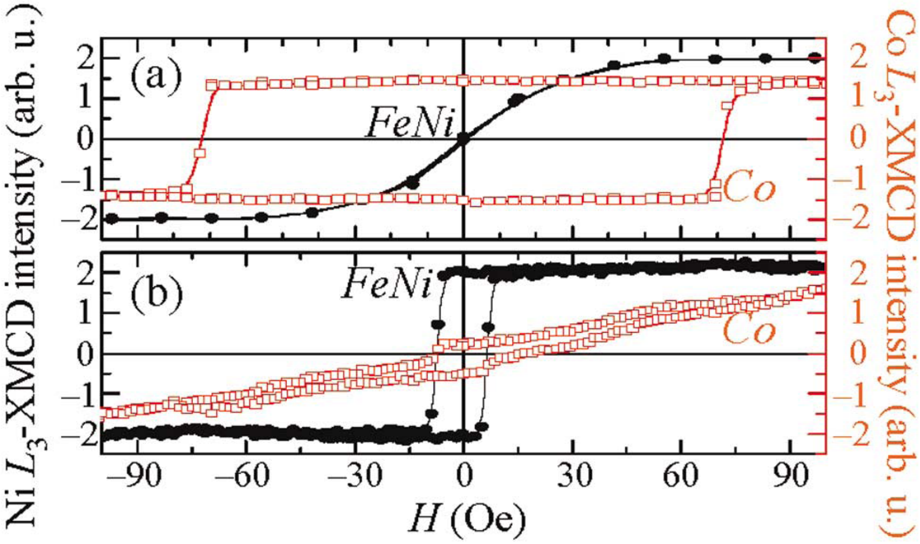

Figure 1.7: XMCD of NiFe/NiO/Co trilayer

Element specific hysteresis curves obtained with XMCD for Co (open circles, right-hand y axis) and NiFe (fill squares, left-hand y axis) with the field applied parallel (a) and perpendicular (b) to the Co easy-axis for a (NiFe 10nm)/(NiO 8nm)/(Co 2nm) trilayer. (Figure taken from Ref. 1.46).

This result falls perfectly in line with Slonczewski's Proximity Model [1.39], where he proposed that if the interfaces between the ferromagnet and antiferromagnet were perfect (*i.e.* chemically and structurally distinct interfaces that were atomically flat) the coupling would oscillate with the thickness of the interlayer, with a periodicity matching the antiferromagnetic ordering parameter (the atomic spacing between similarly aligned planes), meaning an odd (even) number of monolayers would lead to ferromagnetic (antiferromagnetic) coupling (Figure 1.8). However, in real systems, where even the best grown structures can have atomic layer roughness, a new phenomenon occurs. In the vicinity of the roughness, the magnetostatic energy density is quite large (Figure 1.8) if the NiFe layer lies collinear with the Co layer (NiO uniaxial anisotropy direction); to minimize this energy the NiFe layer rotates 90° from the Co easy axis, as observed experimentally [1.46].

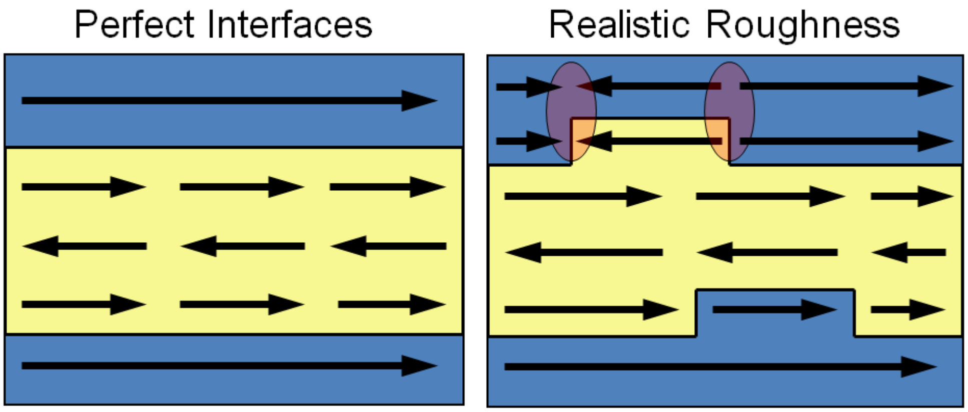

Figure 1.8: Slonczeski Proximity Model

Illustration of the Slonczewski Proximity Model. For ideal interfaces (left panel), the coupling will oscillate with the number of antiferromagnetic monolayers, *i.e.* odd (even) layers leading to ferromagnetic (antiferromagnetic) coupling. For real interfaces with roughness (right panel), the magnetostatic energy density at the edge of the roughness (pink circles) is very large when the ferromagnetic layer is colinear with the antiferromagnet. To reduce this energy, the ferromagnetic easy axis rotates 90° with respect to the antiferromagnet axis.

As stated, the history of interlayer exchange coupling is based upon magnetic heterostructures with in-plane easy axes. In this thesis, we explore the unique advantages and interesting material science when considering structures with perpendicular anisotropy.

1.2 Exchange Bias

Exchange bias, sometimes referred to as uniaxial or exchange anisotropy, refers to a preferred direction of magnetization of a ferromagnet in contact with an antiferromagnet. A shift along the applied field axis of the hysteresis loop (magnetization versus applied magnetic field) occurs when cooling (or growing) the sample in an external field (field-cooling) to below the antiferromagnet's ordering (Néel) temperature (Figure 1.9). Magnetic devices based on exchange bias are of considerable commercial importance for data storage, but the mechanism behind it has been up for debate for more than 50 years. Exchange biasing was first discovered in 1956 by Meiklejohn and Bean with Co particles in contact with the native antiferromagnetic oxide CoO [1.47]. Since that time, a huge amount of experimental and theoretical effort has gone into further exploring the mechanism causing this phenomenon for both a fundamental understanding as well as potential application [1.48 gives an excellent review].

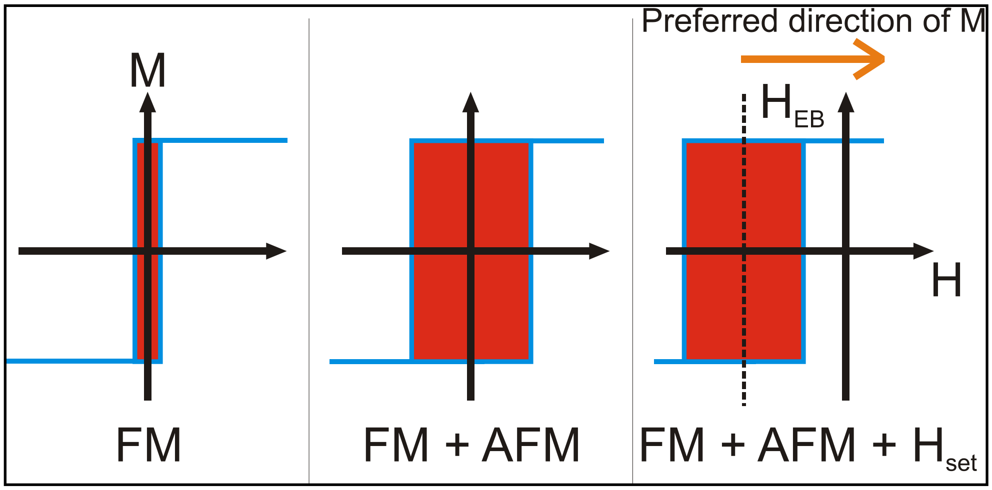

Figure 1.9: Illustration of Exchange Bias

Illustration of exchange bias. Easy axis magnetization loops of a ferromagnetic (FM) film (left), a FM film grown on an antiferromagnet (AFM) (middle), and a FM/AFM bilayer prepared in a field cool $\boldsymbol{H}_{\text{set}}$ (right). In the right structure the ferromagnet is biased with a field $\boldsymbol{H}_{\text{EB}}$. The bias field points to the left, while the preferred direction of the ferromagnetic magnetization points to the right.

From a scientific point of view, the exchange bias phenomenon has been so fascinating because it clearly cannot be a bulk effect because an antiferromagnet has no bulk magnetization, but the effect must be due to the magnetic structure at the bilayer interface. For example, when a ferromagnet is grown on top of an antiferromagnet (in the absence of an applied field) the exchange coupling between the two systems leads to an increased coercivity of the ferromagnet. This is usually attributed to the increased coercivity of "interfacial spins" which need to be dragged around by the external field. In this case, the ferromagnetic hysteresis loop is still symmetric, indicating two equivalent easy directions. If, on the other hand, the bilayer system is grown in a magnetic field or after growth is annealed in a magnetic field to temperatures above the Néel temperature, the hysteresis loop becomes asymmetric and is shifted from zero, indicating pinning by the antiferromagnet into this direction. Since the antiferromagnet is magnetically neutral it is not affected by an external magnetic field; thus, it retains a uniaxial anisotropy pinning the ferromagnet along this preferred direction. Although, the shift in the hysteresis loop along the applied field axis is the most easily observable signature of exchange bias, such systems display many unique signatures.

1.2(a) Exchange Field

When the hysteresis loop of a bilayer system is measured along the unidirectional axis, it is shifted away from the zero field axis by an amount known as the exchange field, H_E (See Figure 1.9, right panel). H_E is related to the exchange biasing energy per unit area, J_{EB}, at the interface by the expression

$$J_{EB} = H_E M_S t_F. \tag{1.6}$$

where M_S and t_F are the saturation magnetization and thickness of the ferromagnetic layer, respectively. Experimental evidence supports the $1/t_F$ dependence of the exchange field, and therefore provides strong evidence for an interfacial effect. There exists a critical temperature known as the blocking temperature T_B, above which the exchange bias disappears. Generally, T_B is lower than the Néel temperature T_N of the antiferromagnetic material.

1.2(b) High Field Rotational Hysteresis

High-field rotational hysteresis persists to fields far higher than the anisotropy field of the ferromagnet. It is measured while rotating the bilayer system in a field high enough to saturate the sample, giving information about the anisotropies present. The presence of a $\sin\theta$ component in the high field hysteresis confirms the presence of unidirectional anisotropy (Figure 1.10) [1.49-1.53].

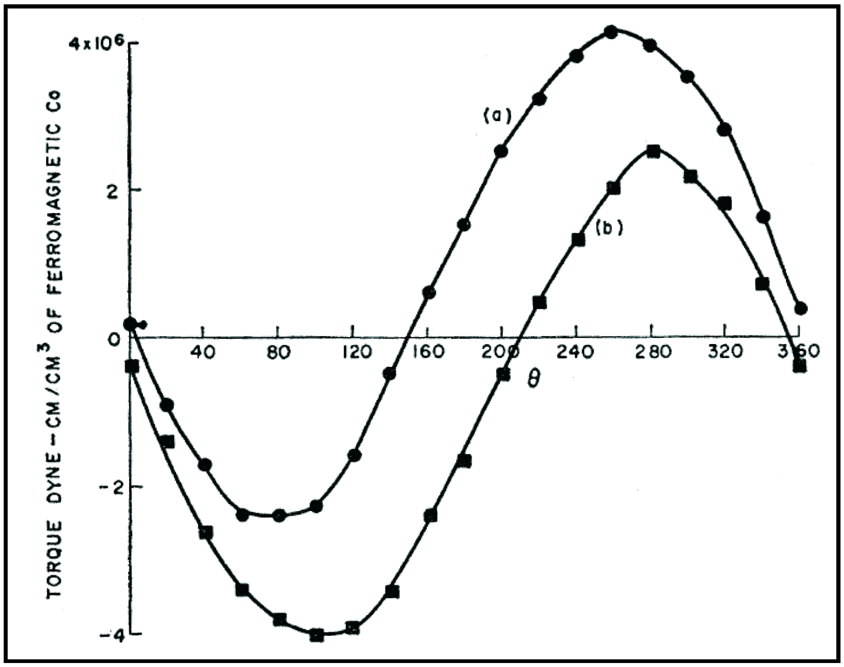

Figure 1.10: Torque curves on Co/CoO particles

Torque curves on CoO coated Co particles cooled in a field to 77 K, where θ is the angle between the cooling-field axis and the direction of the measureing field. Curves (a) and (b) are for rotations of decreasing and increasing θ, respectively. (Figure taken from Ref. 1.47)

1.2(c) Enhanced Coercivity

An enhancement of the coercive field of the ferromagnet material below the antiferromagnet Néel temperature T_N is indicative of exchange coupling and is observed regardless of whether the sample is field cooled or grown in zero field (See Figure 1.9, center panel). Also, the enhancement in coercivity persists above the blocking temperature T_B.

1.2(d) Asymmetric magnetization reversal

Due to the interfacial exchange biasing, the spin arrangement at the interfaces of these bilayer systems can strongly affect the domain wall formation in the ferromagnetic layer, thus influencing the magnetization reversal. The significant macroscopic feature of this effect is the asymmetric loop shape for exchange biased systems. Therefore, investigations on the magnetization reversal of exchange-biased ferromagnetic layer can offer indirect information of the interfacial spin structures.

The interfacial nature of the coupling implies that the exchange field H_E must be strongly dependent on the spin configuration at the interface, which is difficult to determine experimentally. In general, it is assumed that the antiferromagnetic layer maintains its bulk spin configuration due to the antiferromagnetic ordering parameter (or anisotropy), and the antiferromagnetic spins remain fixed during the coherent rotation of the ferromagnetic spins. A simplistic model for exchange bias invokes ideal, perfectly flat interfaces with no interdiffusion or mixing. This model gives unrealistically large exchange values and provides sharp differentiation between compensated and uncompensated interfaces [see 1.54-1.57].

For an ideal compensated antiferromagnetic interface, there is no net magnetization (Figure 1.11, right panel). Therefore, no H_E is expected. In contrast, for an ideal uncompensated antiferromagnetic interface, there is a net interface magnetization (Figure 1.11, left panel).

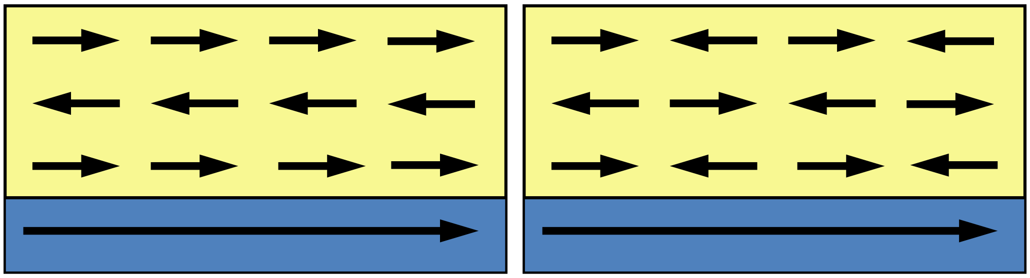

Figure 1.11: Illustration of uncompensated and compensated AFM interfaces

Illustrations for uncompensated (left panel) and compensated (right panel) interfaces between ferromagnetic (blue) and antiferromagnetic (yellow) bilayers.

The exchange interaction energy per unit area between the ferromagnetic and antiferromagnetic interfacial spins is given by

$$J_{EB} = \frac{2J_{ex}\,\mathbf{S}_{AFM} \cdot \mathbf{S}_{FM}}{a^2} \tag{1.7}$$

where J_{ex} is the exchange interaction between the interfacial spins, $\mathbf{S}_{AFM}$ and $\mathbf{S}_{FM}$ are the interfacial spins from the antiferromagnet and ferromagnet, respectively, and a is the spacing between the spins (lattice parameter). The exchange biasing can then be determined experimentally by combining equations 1.6 and 1.7 to get

$$H_E = \frac{J_{EB}}{M_s t_{FM}} = \frac{2J_{ex}\,\mathbf{S}_{AFM} \cdot \mathbf{S}_{FM}}{a^2 M_s t_{FM}}. \tag{1.8}$$

In reality, the experimentally measured values for J_{ex} are substantially different than these models for ideal interfaces. In fact, for compensated interfaces, finite values for exchange bias have been measured [1.58-1.72]. This even includes single crystal antiferromagnets with a deposited ferromagnetic layer [1.67-1.73]. For uncompensated interfaces, the values for J_{EB} are vastly different for experimental (~0.1 erg/cm^2) and theoretical (~10 erg/cm^2) approaches. Therefore, the interfacial coupling between the ferromagnet and antiferromagnet implies non-perfect interfaces (*i.e.* roughness, impurities, disorder) and led to explorations of different mechanisms for exchange bias. In general, theoretical models to resolve this discrepancy in coupling energies rely on the formation of a domain wall within the antiferromagnet (either parallel or perpendicular to the sample surface dependent on the ferromagnetic magnetization), which relaxes some of this energy into the bulk of the antiferromagnet [1.74-1.78].

One current and widely used model for exchange bias in polycrystalline antiferromanet-ferromagnet bilayers was developed by Stiles and McMichael and describes the creation of a domain wall within an ensemble of antiferromagnetic grains, as well as the corresponding temperature dependence and enhancement of coercivity [1.57,1.79,1.80]. In their model they include the coupling energy from three contributions: direct coupling of the ferromagnet to the net moment at the interface of the antiferromagnet grain, spin-flop coupling, and partial domain walls in the antiferromagnet. In addition to these energy terms, they include the possibility of instabilities in the antiferromagnet. They found that the existence of a unidirectional anisotropy occurs without the contribution of spin-flop coupling; however, the other energy terms are significant. The direct coupling between the ferromagnet and antiferromagnet has been discussed (*i.e.* Eqns.1.7 and 1.8); however, further insight into exchange bias arises when considering the properties of the domain walls that form in the antiferromagnet. The properties of these domain walls are determined by the antiferromagnet's exchange coefficient, A_{AF}, and anisotropy energies, K_u. For uniaxial anisotropy, the domain-wall energy per unit area is

$$\sigma = 4\sqrt{A_{AF}K_u} \tag{1.9}$$

and the domain wall width is the given by

$$\delta = \pi\sqrt{A_{AF}/K_u}. \tag{1.10}$$

The exchange coefficient, A_{AF}, is related to the exchange constant, J_{AF}, by

$$A_{AF} = fJ_{AF}S_{AF}^2/a, \tag{1.11}$$

where f is a numerical factor of order unity that depends on the crystal structure, a is a lattice constant and S_{AF} is the magnitude of the antiferromagnetic spin. When the thickness of the antiferromagnetic layer is thin compared to a domain-wall width, a partial domain wall will extend to the back side of the film and unwind itself, removing the bias effect. Thus, eqn. 1.10 gives a critical thickness for the antiferromagnet, about 40 nm in NiO, to observe exchange bias and presents a viable method of relaxing the energy of the interfacial coupling into the bulk of the antiferromagnet ($\sigma \sim 100$ erg/cm^2), resolving the energy disparity between theoretical and experimental results. This model also gives an explanation for irreversible effects during field cycling, where a critical angle, α, is the most a domain wall can wind during the ferromagnetic reversal before the uniaxial anisotropy of the antiferromagnet switches by 180° - adding work to the system. In subsequent papers, Stiles and McMichael describe the temperature dependence, based on the thermal instabilities of the antiferromagnetic grains [1.79], and the enhanced coercivity, which is attributed to inhomogeneous reversal and irreversible transitions in the antiferromagnetic grains [1.80].

The domain state model was further explored by Nowak *et al.* in a series of both theoretical [1.76] and experimental [1.81] papers. In general, previous approaches to the domain state model assumed the creation of domain walls due to roughness at the interface [1.75] or assumed coupling between the ferromagnet and individual antiferromagnetic grains with small or vanishing intergrain coupling [1.57]; however, Nowak *et al.* placed defects within the bulk of the antiferromagnet (referred to as dilution) and saw a strong dependence of the exchange bias field on this dilution. This result suggests the importance of the bulk of the antiferromagnet playing a large role. Based on this discovery they modified previous models to explain a variety of typical effects associated with exchange bias, *i.e.* positive bias, temperature and time dependencies, the thickness dependence of the antiferromagnetic layer, as well as providing an explanation for the exchange bias training effect (see Chapter 1.2(e)). The combined experimental and theoretical findings suggest that the origin of exchange bias in the proto-typical Co/CoO bilayer structure results from a domain state in the volume part of the antiferromagnet stabilized by disorder and defects. The disorder can result from interfacial roughness, defects in the volume part of the antiferromagnet, grain boundaries, or from other sources. Because the exchange bias in this model is so heavily dependent on disorder and defects, this model ties together multiple approaches and experimental results for a variety of systems because any change of interface roughness due to variations in the preparation parameters, such as growth or annealing temperature, most likely also results in a change of defect structure and domain configuration in the antiferromagnetic layer. The interrelation of these defects with the exchange bias is still not quite understood; however, strong support is given to this picture by experiments in which nonmagnetic impurities are added in a systematic and controlled way to the antiferromagnetic layer [1.77, 1.82-1.84] to form and influence domains.

These two contemporary models by Stiles and McMichael [1.57] and Nowak *et al.* [1.76, 1.78] will be used extensively throughout the remainder of this thesis when considering the origin of exchange bias. In particular, the idea explored by Stiles and McMichael that the thickness of the antiferromagnet must be large enough to sustain a domain wall will be a crucial argument and fully explored in the Co/NiO/[Co/Pt] system described in detail in Chapters 6 and 7.

1.2(e) Exchange Bias Training Effect

Many complex phenomena have been observed in exchange biased systems since its discovery, one of the most challenging to understand is the training effects that occur. The training of exchange bias refers to a monotonic decrease of the exchange field, H_E, upon successive field cycling in an isothermal hysteresis loop measurement. This effect has been observed in a wide variety of materials [see the review article Ref 1.48 and the recent work in Ref 1.85 and references there-in] and gives further insight into the interface spin structure of both the ferromagnet and antiferromagnet. The effect is often associated with the asymmetric magnetization reversal (see Chapter 1.2(d)) in exchange biased layers [1.86-1.93]. The conventional view of exchange bias training attributes the effect to a gradual change in the antiferromagnetic spin structure upon repeated field cycling, where H_E originates from a finite density of uncompensated antiferromagnetic spins (as described in Chapter 1.2). Then, the training can be understood as a thermally activated process leading to a gradual depinning of these uncompensated antiferomagnetic spins. This depining leads to a reduction in the unidirectional anisotropy.

There have been a variety of approaches to explain this phenomenon. In particular, approaches based upon the domain state model, already discussed, from Stiles and McMichael [1.57] and Nowak *et al.* [1.76, 1.78] are considered. According to the domain state model, the training effect is due to a rearrangement of the antiferromagnetic domain structure, which results in a partial loss of the interface magnetization of the antiferromagnet during field cycling [1.76]. Once it was established that the training effect was due to this reduction in interface magnetization, various models have arisen that simply look at this relaxation, no longer considering the complicated nature of the bulk of the antiferromagnet.

At present there are two competing approaches: 1) developed by A. Hoffman [1.94] and recently further considered by C. Leighton *et al*. [1.85], which assumes two distinct contributions to the training effect in polycrystalline bilayers and 2) an analytic approach developed by C. Binek using the discretized Landau-Khalatnikov equation [1.95], which describes the relaxation of the interfacial spins of the antiferromagnet. Both approaches provide good modeling to experimental data; however, there is a stark difference in the approach taken by these two models. In the first approach, A. Hoffmann found that biaxial antiferromagnetic anisotropy leads to antiferromagnetic spins freezing into a stable noncollinear configuration, which is relaxed after a single field cycle. C. Leighton *et al.* later includes antiferromagnets with any higher order anisotropy. This results in a single cycle training effect that is quite large and accompanies an assymetric magnetization reversal. Beyond this initial cycle, the subsequent loop effects are quite small and follow the phenomenological $H_E \propto 1/\sqrt{n}$ relationship, where n is the number of field cycles. In contrast, the model proposed by C. Binek is intended to deduce the simple $H_E \propto 1/\sqrt{n}$ relationship using a spin relaxation model based on the Landau-Khalatnikov equation. This phenomenological approach not only describes the training for $n > 1$, but also for $n \geq 1$, combining the full set of training loops into a single model. This model also gives physical insight into the origin of the phenomenological power law observed for loops corresponding to $n > 1$. Assuming the origin of the mechanism in exchange bias training is based on non-equilibrium thermodynamics, the model proposed by C. Binek offers unique insight into the temperature dependence of the effect as well [1.96]. This model has also successfully been applied to antiferromagnetically coupled ferromagnetic layers [1.97] (including temperature dependence [1.98]), dynamic enhancement of the training effect [1.99], and gives a successful model for the scaling behavior of the training effect with thickness [1.100]. This approach by C. Binek, including the temperature dependence of training, will be used extensively in chapter 7 to analyze the temperature and set field training dependence for our Co/NiO/[Co/Pt] structures.

1.3 NiO Crystalline and Magnetic Structure

NiO is an antiferromagnetic insulator with a critical temperature (called the Néel temperature) in the bulk crystal of T_N = 523 K. Above T_N, NiO has a perfect cubic rocksalt (NaCl) structure, having Ni^{2+} ions at the cubic and face-centered sites (Figure 1.12).

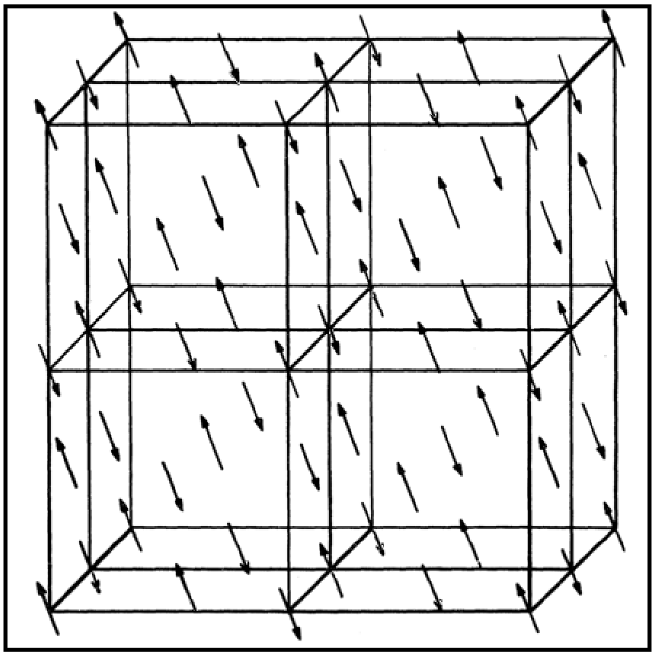

Figure 1.12: Atomic and magnetic structure of NiO

An eight unit cell magnetic diagram of face-centered cubic NiO. The Ni^{2+} spins reside at the cubic and face-centered sites and point along the $\langle 11\bar{2}\rangle$ axes (Figure taken from Ref. 1.85).

However, cooling below T_N leads to a slight rhombohedral deformation of the cubic crystal, which is composed of a contraction of the original cubic unit cell along the $\langle 111\rangle$ axes [1.101]. This distortion results in a change in the unit cell angle from 90° above T_N

to 90°4' at 297K and 90°6' at 78K [1.102,1.103]. Because there are four distinct $\langle 111\rangle$ directions, this will lead to the formation of four T (twin) domains. As determined from neutron diffraction [1.104,1.105] and X-ray magnetic linear dichroism [1.106], the spins lie ferromagnetically ordered within the $\{111\}$ planes, where each $\{111\}$ plane stacks antiferromagnetically along the $\langle 111\rangle$ axes. In adjacent T domains the spin direction changes continuously from one domain to another without alteration of spin directions in the T domain wall (Figure 1.13).

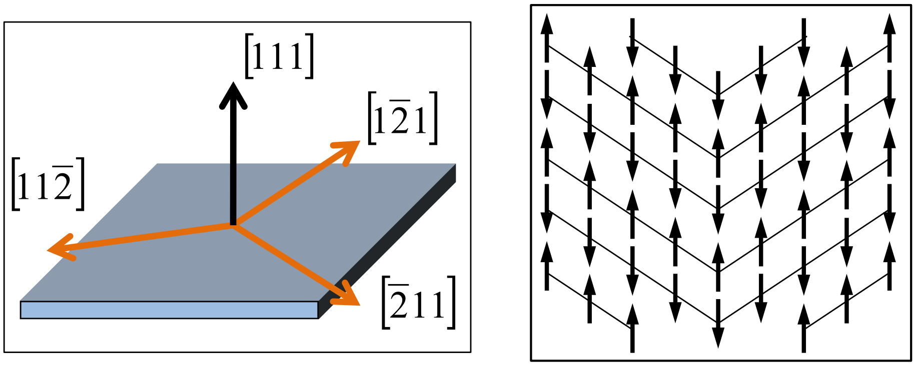

(a) Equivalent Easy Axes (S Domains)

(b) T domain wall

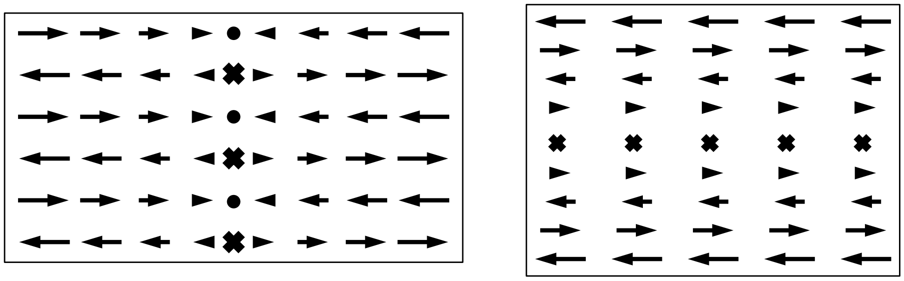

(d) $S_{\perp}$domain wall

(d) $S_{||}$ domain wall

Figure 1.13: NiO domain walls

Description of domain walls in NiO. (a) There are three equivalent $\langle 11\bar{2}\rangle$ easy axes in a particular $\{111\}$ plane (S domains). (b) T walls which are induced by the contractions along different $\langle 111\rangle$ axes. The solid lines trace the spins in the ferromagnetic $\{111\}$ planes. (c) $S_{\perp}$

domain walls in which the spin rotation occurs within the ferromagnetic $\{111\}$ planes. (d) $S_{\parallel}$ domain walls in which the spin rotation occurs between adjacent $\{111\}$ planes.

In addition, the spins within the $\{111\}$ plane lie parallel to the $\langle 11\bar{2}\rangle$ axes. Thus, in total there are three equivalent easy axes within the $\{111\}$ planes, *i.e.* $[11\bar{2}]$, $[\bar{2}11]$, and $[1\bar{2}1]$, leading to three possible S (spin) domains with each T domain. The boundaries between adjacent S domains are termed S domain walls, in which the spins rotate away from the $\langle 11\bar{2}\rangle$ axes. There are two possible rotations of spin directions within S domain walls, these two types are $S_{\perp}$ and $S_{\parallel}$. In the $S_{\perp}$ domain wall, the spins rotate within the $\{111\}$ plane (Figure 1.13). In the $S_{\parallel}$ domain wall, the spins rotate between adjacent $\{111\}$ planes (Figure 1.13). Including all of these easy axes, there are a possible 24 kinds of domains in NiO in total. As discussed in Chapter 1.2, the existence of domain walls within the NiO layer is a necessary condition for the presence of exchange bias [1.107,1.108]. For the sputtered thin films considered in this thesis, a lack of in-plane anisotropy leads to all possible spin orientations existing within the plane. This will be further discussed in subsequent chapters.

The Néel temperature is remarkably different from the bulk when considering the NiO thin film case. It is very difficult to ascertain experimentally the Néel temperature of a very thin antiferromagnetic film, particularly in a ferromagnet/antiferromagnet/ferromagnet trilayer; however, previous experiments have led to some insight. Previous measurements on epitaxial thin films of NiO indicate Néel temperatures of ~300K for a 5 ML sample [1.108], a dramatic reduction from the bulk.

It's expected that a polycrystalline sputtered film may be even further reduced from the bulk. However, when the antiferromagnet is placed in close proximity to a ferromagnet, ferrimagnet or antiferromagnet with a higher Néel temperature, an enhancement of the Néel temperature is observed. For example, neutron scattering studies on both Fe_3O_4/NiO [1.109] and Fe_3O_4/CoO superlattices [1.110] show that the ferrimagnetic ordering of the Fe_3O_4 stabilizes the antiferromagnetic ordering of the antiferromagnet, leading to Néel temperatures well over the bulk Néel temperature. In addition, in many magnetic superlattices, only a single transition temperature (the Curie and/or the Néel temperature) exists for the entire structure [1.110-1.112].

Given these details, NiO is a unique 'playground' for magnetic studies of interfacial interactions (*i.e.* interlayer exchange coupling or exchange bias) due to the strongly differing anisotropy constants for in-plane and out-of-plane rotations. For NiO, the anisotropy constant for in-plane rotation (within the {111} planes) is suggested to be ~5% of the out-of plane rotation (perpendicular to the {111} planes), $K_1=3.32\times10^6$ erg/cm^3 [1.101, 1.112]. This huge variation implies a higher blocking temperature (see Chapter 1.2) for out-of-plane exchange bias, compared to in-plane. Also, it implies a unique canting model of Ni spins in and out of the plane due to the presence of adjacent ferromagnets, which will be discussed in great detail in the remainder of this thesis.

1.4 References

1.1. M. N. Baibich, J. M. Broto, A. Fert, F. Nguyen Van Dau, F. Petroff, P. Etienne, G. Creuzet, A. Friederich, and J. Chazelas, Phys. Rev. Lett. **61**, 2472 (1988).

1.2. G. Binasch, P. Grünberg, F. Saurenbach, and W. Zinn, Phys. Rev. B **39**, 4828 (1989).

1.3. T. Miyazaki and N. Tezuka, J. Magn. Magn. Mater. **139**, L231 (1995).

1.4. J. S. Moodera, Lisa R. Kinder, Terrilyn M. Wong, and R. Meservey, Phys. Rev. Lett. **74**, 3273 (1995).

1.5. B. Dieny, V. S. Speriosu, S. S. P. Parkin, B. A. Gurney, D. R. Wilhoit, and D. Mauri, Phys. Rev. B **43** , 1297 (1991).

1.6. P. Grünberg, R. Schreiber, Y. Pang, M. B. Brodsky and H. Sowers, Phys. Rev. Lett. **57**, 2442 (1986).

1.7. S. S. P. Parkin, N. More, and K. P. Roche, Phys. Rev. Lett. **64**, 2304 (1990).

1.8. Eric E. Fullerton, M. J. Conover, J. E. Mattson, C. H. Sowers, and S. D. Bader, Phys. Rev. B **48**, 15755 (1993).

1.9. S. S. P. Parkin, Phys. Rev. Lett. **67**, 3598 (1991).

1.10. S. Toscano, B. Briner, and M. Landolt, in Magnetism and Structure in Systems of Reduced Dimensions, edited by R.F.C. Farrow, B. Dieny, M. Donath, A. Fert, and B.D. Hermsmeier, Vol.309 of NATO Advanced Study Institute, Series B: Physics (Plenum Press, New York, 1993), P. 257.

1.11. J. Faure-Vincent, C. Tiusan, C. Bellouard, E. Popova, M. Hehn, F. Montaigne, and A. Schuhl, Phys. Rev. Lett. **89**, 107206 (2002).

1.12. S. Yuasa, T. Nagahama, A. Fukushima, Y. Suzuki, and K. Ando, Nature Mater. **3**, 868 (2004).

1.13. C. Tiusan, J. Faure-Vincent, C. Bellouard, M. Hehn, E. Jouguelet, and A. Schuhl, Phys. Rev. Lett. **93**, 106602 (2004).

1.14. R. Guerrero, D. Herranz, F. G. Alieva, F. Greullet, C. Tiusan, M. Hehn, and F. Montaigne, Appl. Phys. Lett. **91**, 132504 (2007).

1.15. Wenhong Wang, Hiroaki Sukegawa, Rong Shan, and Koichiro Inomata, Appl. Phys. Lett. **93**, 182504 (2008).

1.16. S. Ikeda, J. Hayakawa, Y. Ashizawa, Y. M. Lee, K. Miura, H. Hasegawa, M. Tsunoda, F. Matsukura, and H. Ohno, Appl. Phys. Lett. **93**, 082508 (2008)

1.17. S. G. Wang, R. C. C. Ward, G. X. Du, X. F. Han, C. Wang, and A. Kohn, Phys. Rev. B **78**, 180411 (2008).

1.18. S. S. Parkin, C. Kaiser, A. Panchula, P. M. Rice, B. Hughes, M. Samant, and S. H. Yang, Nature Mater. **3**, 862 (2004).

1.19. Y. Yafet, Phys. Rev. B **36**, 3948 (1987).

1.20. C. Chappert and J.P. Renard, Europhys. Lett. **15**, 553 (1991).

1.21. P. Bruno and C. Chappert, Phys. Rev. Lett. **67**, 1602 (1991); Phys. Rev. Lett **67**, 2592(E) (1991); Phys. Rev. B **46**, 261 (1992).

1.22. R. Coehoorn, Phys. Rev. B **44**, 9331 (1991).

1.23. J. Barnas, J. Magn. Magn. Mater. **111**, L215 (1992).

1.24. R.P. Erickson, K.B. Hathaway, and J.R. Cullen, Phys. Rev. B **47**, 2626 (1993).

1.25. J.C. Slonczewski, J. Magn. Magn. Mater. **126**, 374 (1993).

1.26. E. Bruno and B.L. Gyorffy, J. Phys. Condens Mat. **5**, 2109 (1993); Phys. Rev. Lett. **71**, 181 (1993).

1.27. D.M. Edwards, J. Mathon, R.B. Muniz, and M.S. Phan, Phys. Rev. Lett. **67**, 493 (1991).

1.28. J. Mathon, M. Villeret, and D.M. Edwards, J. Phys. Condens. Matt. **4**, 9873 (1992).

1.29. Y. Wang, P.M. Levy, and J.L. Fry, Phys. Rev. Lett. **65**, 2732 (1990).

1.30. Z.P. Shi, P.M. Levy, and J.L. Fry, ibid. **69**, 3678 (1992).

1.31. P. Bruno, J. Magn. Magn. Mater. **116**, L13 (1992).

1.32. P. Bruno, J. Magn. Magn. Mater. **121**, 248 (1993); Europhys. Lett. **23**, 248 (1993); Phys. Rev. B **49**, 13231 (1994); Phys. Rev. B **52**, 52 (1995).

1.33. Z. Zhang, L. Zhou, P. E. Wigen, and K. Ounadjela, Phys. Rev. Lett. **73**, 336 (1994).

1.34. N. Persat and A. Dinia, Phys. Rev. B **56**, 2676 (1997).

1.35. P. Bruno, Phys. Rev. B **52**, 411 (1994).

1.36. P.J.H. Bloemen, M.T. Johnson, M.T.H. van de Vorst, B. Coehoorn, J.J. de Vries, R. Jungblut, J. aan de Stegge, A. Reinders, and W.J.M. de Jonge, Phy. Rev. Lett. **72**, 764 (1994).

1.37. S.N. Okuno and K. Inomata, Phys. Rev. Lett. **72**, 1553 (1994).

1.38. S.O. Demokritov, J. Phys. D **31**, 925 (1998).

1.39. J. C. Slonczewski, J. Magn. Magn. Mater. **150**, 13 (1995).

1.40. H. Xi and R.M.White, Phys. Rev. B **62**, 3933 (2000).

1.41. M. E. Filipkowski, J. J. Krebs, C. J. Gutierrez, G. A. Prinz, Phys. Rev. Lett. **75**, 1847 (1995).

1.42. V. Chakarian, Y. U. Idzerda, H.-J. Lin, C. Gutierrez, G. A. Prinz, G. Meigs and C. T. Chen, Phys. Rev. B **53**, 11313 (1996).

1.43. P. A. A. van der Heijden, C. H. W. Swüste, W. J. M. de Jonge, J. M. Gaines, J. T. W. M. van Eemeren, and K. M. Schep, Phys. Rev. Lett. **82**, 1020 (2000).

1.44. S.-S. Yan, R. Schreiber, F. Voges, C. Osthöver, and P. Grünberg, Phys. Rev. B **59**, R11641 (1999).

1.45. F. H. Yang and C. L. Chien, Phys. Rev. Lett. **85**, 2597 (2000).

1.46. J. Camarero, Y. Pennec, J. Vogel, M. Bonfim, S. Pizzini, F. Ernult, F. Fettar, F. Garcia, F. Lançon, L. Billard, B. Dieny, A. Tagliaferri and N. B. Brookes, Phys. Rev. Lett. **91**, 027201-1 (2003).

1.47. W.H. Meihlejohn and C.P. Bean, Phys. Rev. **105**, 904 (1957).

1.48. J. Nogues and I.K. Schuller, J. Magn. Magn. Mater. **192**, 203 (1999).

1.49. D. Paccard, C. Schlenker, O. Massenet, R. Montmory, and A. Yelon, Phys. Status Solidi **16**, 301 (1966).

1.50. W. H. Meiklejohn, J. Appl. Phys. **33**, 1328 (1962).

1.51. C. Schlenker, J. Phys. (Paris), Colloq. **29**, C2-157 (1968).

1.52. M. Takahashi, A. Yanai, S. Taguchi, and T. Suzuki, Jpn. J. Appl. Phys. **19**, 1093 (1980).

1.53. C.-H. Lai, H. Matsuyama, R. L. White, T. C. Anthony, and G. G. Bush, J. Appl. Phys. **79**, 6389 (1996).

1.54. C. Tsang and K. Lee, J. Appl. Phys. **53**, 2605 (1982).

1.55. T. Ambrose and C. L. Chien, J. Appl. Phys. **83**, 7223 (1998).

1.56. J. Nogués, T. J. Moran, D. Lederman, Ivan K. Schuller, and K.V. Rao, Phys. Rev. B **59**, 6984 (1999).

1.57. M. D. Stiles and R. D. McMichael, Phys. Rev. B **59**, 3722 (1999).

1.58. P.J. van der Zaag, R.M. Wolf, A.R. Ball, C. Bordel, L.F. Feiner, and R. Jungblut, J. Magn. Magn. Mater. **148**, 346 (1995).

1.59. P.J. van der Zaag, A.R. Ball, L.F. Feiner, R.M. Wolf, and P.A.A. van der Heijden, J. Appl. Phys. **79**, 5103 (1996).

1.60. Y. Ijiri, J.A. Borchers, R.W. Erwin, S.H. Lee, P.J. van der Zaag, and R.M. Wolf, Phys. Rev. Lett. **80**, 608 (1998).

1.61. J.X. Shen and M.T. Kief, J. Appl. Phys. **79**, 5008 (1996).

1.62. D.H. Han, J.G. Zhu, and J.H. Judy, J. Appl. Phys. **81**, 4996 (1997).

1.63. D.H. Han, J.G. Zhu, J.H. Judy, and J.M. Sivertsen, J. Appl. Phys. **81**, 340 (1997).

1.64. D.H. Han, J.G. Zhu, J.H. Judy, and J.M. Sivertsen, J. Appl. Phys. **81**, 4519 (1997).

1.65. S.S. Lee, D.G. Hwang, C.M. Park, K.A. Lee, and J.R. Rhee, J. Appl. Phys. **81**, 5298 (1997).

1.66. H.S. Chopra, B.J. Hockey, P.J. Chen, R.D. Mcmichael, and W.F. Egelhoff Jr., J. Appl. Phys. **81**, 4017 (1997)

1.67. J. Nogues, T.J. Moran, D. Lederman, I.K. Schuller, and K.V. Rao, Phys. Rev. B **59**, 6984 (1999).

1.68. J. Nogues, T.J. Moran, D. Lederman, I.K. Schuller, and K.V. Rao, Appl. Phys. Lett. **68**, 3186 (1996).

1.69. J. Nogues, T.J. Moran, D. Lederman, and I.K. Schuller, Phys. Rev. Lett. **76**, 4624 (1996).

1.70. D. Lederman, J. Nogues, and I.K. Schuller, Phys. Rev. B **56**, 2332 (1997).

1.71. R. Jungblut, R. Coehoorn, M.T. Johnson, C. Sauer, P.J. van der Zaag, A.R. Ball, T.G.S.M. Rijks, J. aan de Stegge, and A. Reinders, J. Magn. Magn. Mater. **148**, 300 (1995).

1.72. C.M. Park, K.I. Min, and K.H. Shin, J. Appl. Phys. 79, 6228 (1996); R. Jungblut, R. Coehoorn, M.T. Johnson, J. aan de Stegge, and A. Reinders, J. Appl. Phys. **75**, 6659 (1994).

1.73. T.J. Moran, J.M. Gallego, and I.K. Schuller, J. Appl. Phys. **78**, 1887 (1995).

1.74. D. Mauri, H.C. Siegmann, P.S. Bagus, and E. Kay, J. Appl. Phys. **62**, 3047 (1987).

1.75. A.P. Malozemoff, Phys. Rev. B 35, 3679 (1987); J. Appl. Phys.**63**, 3874 (1988).

1.76. U. Nowak, K.D. Usadel, J. Keller, P. Miltenyi, B. Beschoten, and G. Guntherodt, Phys. Rev. B **66**, 014430 (2002).

1.77. P. Miltnyi, M. Gierlings, J. Keller, B. Beschoten, and G. Gntherodt U. Nowak and K. D. Usadel, Phys. Rev. Lett. **84**, 4224 (2000).

1.78. J. Keller, P. Miltenyi, B. Beschoten, and G. Guntherodt U. Nowak and K. D. Usadel Phys. Rev. B **66**, 014431 (2002).

1.79. M. D. Stiles and R. D. McMichael, Phys. Rev. B **60**, 12950 (1999).

1.80. M. D. Stiles and R. D. McMichael, Phys. Rev. B **63**, 064405 (2001).

1.81. J. Keller, P. Miltenyi, B. Beschoten, G. Guntherodt, U. Nowak, and K.D. Usadel, Phys. Rev. B **66**, 014431 (2002).

1.82. T. Mewes, R. Lopusnik, J. Fassbender, B. Hillebrands, M. Jung, D. Engel, A. Ehresmann, and H. Schmoranzer, Appl. Phys. Lett. **76**, 1057 (2000).

1.83. A. Mougin, T. Mewes, M. Jung, D. Engel, A. Ehresmann, H. Schmoranzer, J. Fassbender, and B. Hillebrands, Phys. Rev. B **63**, 060409 (2001).

1.84. H. T. Shi, D. Lederman, and E. E. Fullerton, J. Appl. Phys. **91**, 7763 (2002).

1.85. M. K. Chan, J. S. Parker, P. A. Crowell, and C. Leighton, Phys. Rev. B **77**, 014420 (2008).

1.86. V. I. Nikitenko, V. S. Gornakov, A. J. Shapiro, R. D. Shull, K. Liu, S. M. Zhou, and C. L. Chien, Phys. Rev. Lett. **84**, 765 (2000).

1.87. M. R. Fitzsimmons, P. Yashar, C. Leighton, I. K. Schuller, J. Nogués, C. F. Majkrzak, and J. A. Dura, Phys. Rev. Lett. **84,** 3986 (2000).

1.88. C. Leighton, M. R. Fitzsimmons, P. C. Yashar, A. Hoffmann, J. Nogués, J. A. Dura, C. F. Majkrzak, and I. K. Schuller, Phys. Rev. Lett. **86**, 4394 (2001).

1.89. H. D. Chopra, D. X. Yang, P. J. Chen, H. J. Brown, L. J. Swatzendruber, and W. F. Egelhoff, Jr., Phys. Rev. B 61, 15312 (2000).

1.90. T. Mewes, H. Nembach, M. Rickart, S. O. Demokritov, J. Fassbender, and B. Hillebrands, Phys. Rev. B **65**, 224423 (2002).

1.91. T. Mewes, H. Nembach, J. Fassbender, B. Hillebrands, J. V. Kim, and R. L. Stamps, Phys. Rev. B **67**, 104422 (2003).

1.92. X. Portier, A. K. Petford-Long, A. de Morais, N. W. Owen, H. Laidler, and K. O’Grady, J. Appl. Phys. **87**, 6412 (2000).

1.93. J. Camarero, J. Sort, A. Hoffmann, J. M. García-Martín, B. Dieny, R. Miranda, and J. Nogués, Phys. Rev. Lett. **95**, 057204 (2005).

1.94. A. Hoffmann, Phys. Rev. Lett. **93**, 097203 (2004).

1.95. C. Binek, Phys. Rev. B **70**, 014421 (2004).

1.96. Christian Binek, Xi He, and Srinivas Polisetty, Phys. Rev. B **72**, 054408 (2005).

1.97. Ch. Binek, S. Polisetty, Xi He, and A. Berger, Phys. Rev. Lett. **96**, 067201 (2006).

1.98. S. Polisetty, S. Sahoo, A. Berger, and Ch. Binek, Phys. Rev. B **78**, 184426 (2008).

1.99. S. Sahoo, S. Polisetty, Ch. Binek, A. Berger, J. Appl. Phys. **101**, 053902 (2007).

1.100. Srinivas Polisetty, Sarbeswar Sahoo, and Christian Binek, Phys. Rev, B **76**, 184423 (2007).

1.101. M. T. Hutchings and E. J. Samuelsen, Phys. Rev. B **6**, 3447 (1972).

1.102. N.C. Tombs and H.P. Rooksby, Nature **165**, 442 (1950).

1.103. G.A. Slack, I. Appl. Phys. **31**, 1571 (1960).

1.104. W.L. Roth, Phys. Rev. **110**, 1333 (1958); **111**, 772 (1958).

1.105. W.L. Roth and G.A. Slack, J. Appl. Phys. **31**, 3526 (1960).

1.106. W. Zhu, L. Seve, R. Sears, B. Sinkovic, and S.S. Parkin, Phys. Rev. Lett. **86**, 5389 (2001).

1.107. H. Ohldag, A. Scholl, F. Nolting, S. Anders, F.U. Hillebrecht, and J. Stohr, Phys. Rev. Lett. **86**, 2878 (2001).

1.108. D. Alders, L.H. Tjeng, F.C. Voogt, T. Hibma, G.A. Sawatzky, C.T. Chen, J. Vogel, M. Sacchi and S. Iacobucci, Phys. Rev. B **57**, 11623 (1998).

1.109. J. A. Borchers, R. W. Erwin, S. D. Berry, D. M. Lind, J. F. Ankner, E. Lochner, K. A. Shaw and D. Hilton, Phys. Rev. B **51**, 8276 (1995).

1.110. P. J. van der Zaag, Y. Ijiri, J. A. Borchers, L. F. Feiner, R. M. Wolf, J. M. Gaines, R. W. Erwin and M. A. Verheijen, Phys. Rev. Lett. **84**, 6102 (2000).

1.111. J. A. Borchers, M. J. Carey, R. W. Erwin, C. F. Majkrzak, and A. E. Berkowitz, Phys. Rev. Lett. **70**, 1878 (1993).

1.112. Ken Takano, Ph.D. Thesis, University of California-San Diego (1998).

Chapter 2

Sample Preparation and Characterization Techniques

This chapter outlines the sample fabrication and characterization techniques needed for this thesis work. Thin film samples were deposited by magnetron sputtering, which is a method of depositing both thin metal films and insulators onto a substrate without needing to heat the material being deposited (giving access to the deposition of alloys and insulators as composite materials). To produce micron-sized magnetic features photolithography was used. Throughout this study the characterization techniques fall into two categories: structural characterization and magnetic characterization. Structural characterization was accomplished with x-ray diffraction and x-ray reflectivity, which give access to the crystalline structure, thickness and local/ long-range roughness of the various constituent layers. Magnetic properties of the studied films were characterized using magneto-optical Kerr effect (MOKE), alternating gradient force magnetometry (AGFM), x-ray magnetic circular dichroism (XMCD), XMCD-photoemission electron microscopy (XMCD-PEEM), magnetic force microscopy (MFM) and neutron diffraction for antiferromagnetic materials.

2.1 Magnetron Sputtering

Sputtering is a powerful and flexible technique which can be used to deposit thin films of a wide range of materials, any solid metal or alloy and a variety of compounds, onto a substrate. At its core, sputtering is the removal of atomized material from the target due to energetic bombardment of its surface layers by accelerated ions. To accomplish this bombardment, an electric field is applied between the sample holder, which is grounded, and the target material. A flow of inert gas (in this case Ar) is passed into the chamber and free electrons within this gas (and newly created free electrons) are accelerated by the applied electric field and collide with the Ar atoms. When the electron energy is lower than 2 eV, the collisions between electrons and Ar atoms are elastic. When the electron energy is greater than 15 eV, the collisions become inelastic, resulting in the ionization of Ar atoms, which produce a plasma within the chamber by creating positive Ar ions and new free electrons. When the electron energy is between 2 and 15 eV, the collision process between electrons and Ar atoms is complicated, with a variety of inelastic collisions occuring.

In addition to the applied electric field, a magnetic field, produced with permanent magnets beneath the target material, exists just above the target material. Because the electric and magnetic fields are approximately perpendicular to each other, the electrons produced during the collisions propagate in helical orbits and are constrained above the targets, efficiently enhancing the further ionization of Ar atoms.

The positive Ar ions are accelerated by the applied electric field towards the target; upon impact these ions will transfer momentum to the atoms within the target material and these atoms will be ejected outward – some of which will strike the substrate surface (See Figure 2.1.1). By controlling the partial Ar gas pressure and the electric field above the target material, one can systematically control the growth conditions of sputtered thin films. Further details on magnetron sputtering can be found in references 2.1-2.3.

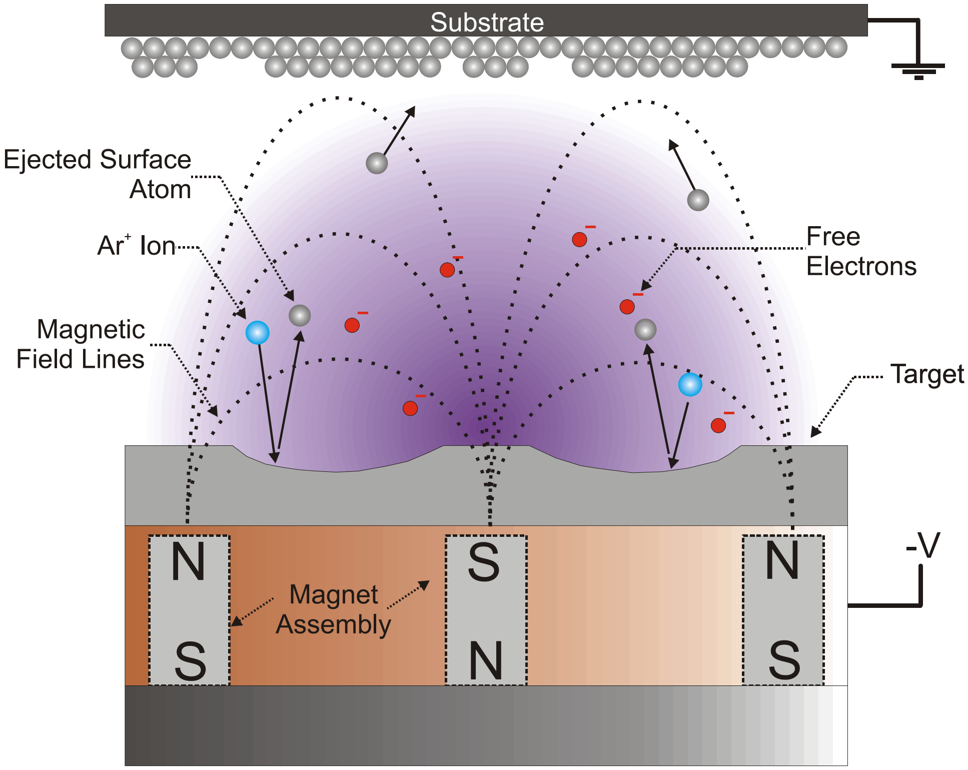

Figure 2.1.1: Magnetron sputtering diagram

A cross sectional schematic diagram of the magnetron sputtering process. The purple background represents the presence of the plasma made up of free electrons and Ar^+ ions.

The magnetron sputtering system used is an AJA ATC-2000-V system with Phase II control (Figure 2.1.2). This system consists of two chambers, a main deposition chamber and a load lock chamber. Both chambers are evacuated by separate turbo-molecular pumps backed by dry-scroll roughing pumps, achieving typical base pressures of ~ 2×10^{-8} Torr in the main chamber and ~ 6×10^{-8} Torr in the load lock chamber. The turbo-molecular pump for the main chamber is a Varian TV-551 Navigator, backed by an Alcatel ACP28 frictionless, multi-stage Roots design pump. The turbo-molecular pump for the load lock is a Varian TV-301 Navigator, backed by a Varian SH-110 Dry Scroll

Roughing pump. By utilizing the load lock chamber, it allows for multiple depositions without ever breaking the main chamber vacuum. The load lock can accommodate 6 or 12 substrates by utilizing two cassette-type holders. Also inside the load lock is a small station to change shadow masks, which allows for shadow-based patterning of thin films during deposition. With this mask changing station one can deposit a variety of patterned layers (up to 6) on a single substrate without breaking vacuum. Masks can also be rotated in 90 degree increments *in situ*. The main chamber consists of 4 sputtering guns mounted *con-focal* and equidistant from the substrate. Each gun angle can be adjusted to point directly towards the sample space or away for various deposition rates and thickness gradient effects. Two guns are set up for magnetic sputtering targets and two for other materials. The differences in these two types of guns are in the magnetic field configuration used to trap secondary electrons close to the target. The electrons follow helical paths around the magnetic field lines undergoing more ionizing collisions with the Ar^+ near the target than would otherwise occur. This enhances the ionization of the plasma near the target leading to a higher sputtering rate. It also means that the plasma can be sustained at a lower pressure. When dealing with magnetic or non-magnetic targets the configuration of these permanent magnets differs as stray magnetic fields emanating from ferromagnetic targets disturb the sputtering process, thus strong permanent magnets are used to compensate. There are two dc power supplies (Advanced Energy MDX 500) for depositing metallic films and two rf power supplies (Advanced Energy RF-5S) for depositing oxide or semiconducting films. An rf supply is necessary for insulators and semiconductors to avoid charge build-up at the surface, which would stall the sputtering process (*i.e.* the Ar^+ ions will be repelled).

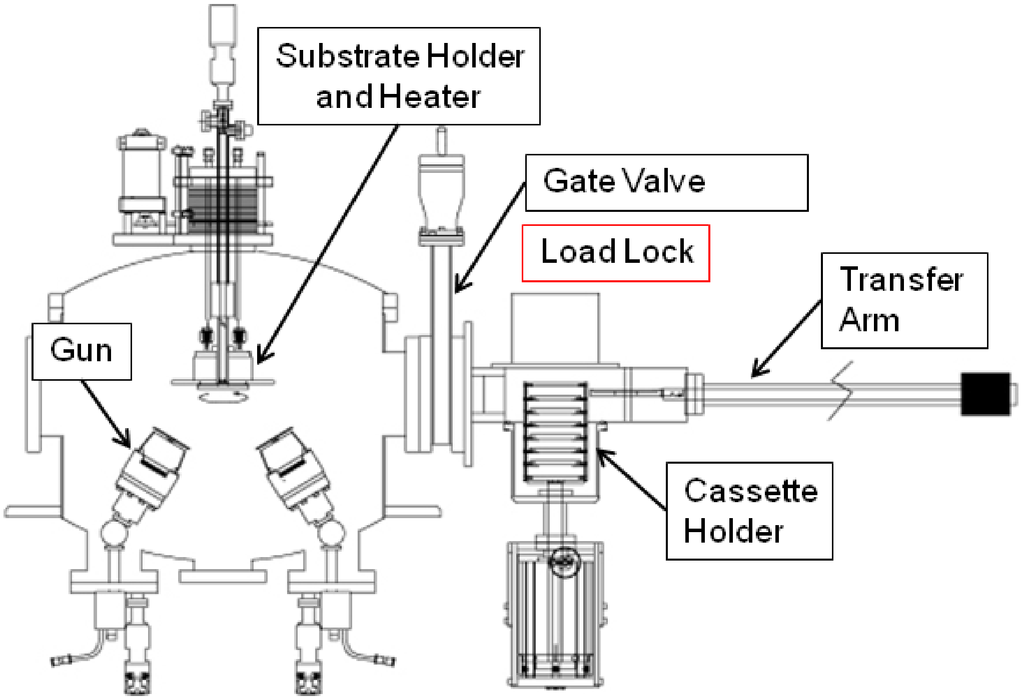

Figure 2.1.2: Schematic of theAJA ATC-2000-V

Schematic of the AJA ATC-2000-V system with Phase II control, having both a load lock and main chamber separated by a gate valve. The guns are in a confocal setup with adjustable angle. The substrate holder can rotate a full 360° and also has a temperature stage (~600°C max). The Cassette holder is described in the text. The substrate is transferred from the Load Lock to the Main Chamber and back via the Transfer Arm (Figure modified from stock AJA schematic)

There are three separate gas flow lines, which allow for non-reactive (inert gas only) or reactive (inert gas with the addition of a reactive gas) deposition. Two lines are mixed and go into the main chamber and the third line goes into one gun. Each line is controlled by a separate Mass Flow Controller. For most processes Argon is used as the sputtering gas with a typical pressure of 25 mTorr during the initial striking of the target and 2 mTorr during deposition (these values were found to be optimal for growth in this specific chamber). This sputtering chamber has the option to flow O_2 in partial pressure with the Ar gas for reactive sputtering. The main chamber also has an *in situ* Inficon XTM/2 quartz crystal thickness monitor, which can be moved in and out of the sample space and is used for quick calibration of thickness for the various targets. With a frequency resolution of 0.1 Hz in 250 milliseconds, the XTM/2 accurately displays deposition rate resolutions as small as 0.01 Angstroms per second [2.4]. The chamber also has the ability to rotate, heat, and cool the substrate during deposition using a dc electric motor rotation stage, a resistive heating plate (maximum temperature of 600°C) and a liquid N_2 dewar with copper backing plate, respectively.

2.2 Photolithography

Photolithography, or optical lithography, is a method to selectively remove sections of a thin film. Similar to photography, it uses light to transfer a pattern into a polymer-based photoresist. The pattern can either be transferred through a photomask, or similar to photography, by using a projected image. The structure size is limited by the wavelength of light used to expose the pattern, which is typically somewhere in the deep UV region, where

$$CD = k\lambda \,, \tag{2.2.1}$$

CD is the critical dimension, λ is the wavelength of light and k is a coefficient that takes into account all of the processing factors (typical values are ~0.4). For the purposes of this thesis the smallest feature size of 10 μm make this an approachable task with UV light in the 240-290 nm range. The only issues for ultimate values for *CD* arise from the presence of dust and the mask aligning procedure.

There are two possible approaches for photolithography, a lift-off process and an etching process (either wet or dry). In addition, both positive and negative resists exist. A positive resist will be removed where the light was exposed during development of the sample and a negative resist will remain where the light exposed the sample. For the lift off process, using a two resist approach makes the best features with the smoothest edge. Optimization of parameters led to the following successful recipe (see Figure 2.2.1):

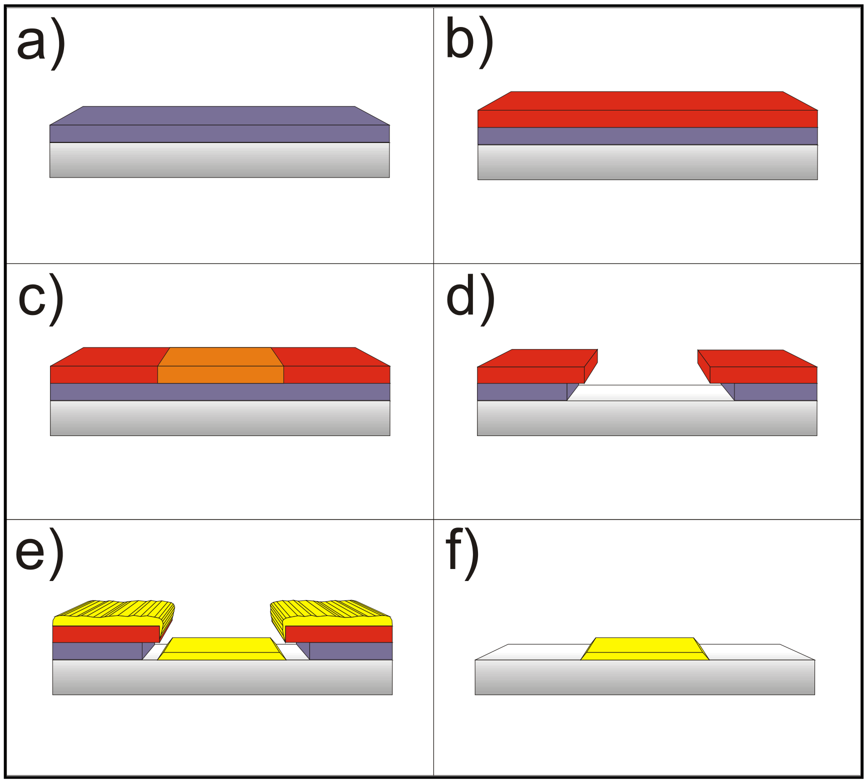

Figure 2.2.1: Photolithography lift-off process

Visual demonstration of the steps in the photolithography lift-off process using a two layered photo resist approach. Description of each step can be found in the text.

1. After the substrate is cleaned thoroughly (any dust at this stage will cause major problems for the later lift-off), a layer of the resist Microchem™ Nano™ PMGI-SF3 (a positive resist that will remove well with the developer) is spin coated onto the substrate – spinning at 3000 rpm for 30s. The sample is then baked for 15 minutes. On a Corning hot plate (or inside an oven in some cases), the resist is baked at a temperature of ~170° C – this was determined with trial and error (Figure 2.2.1.a).

2. The next layer of resist, Microposit™ S1813™ Positive Photo Resist, is spin coated onto the substrate – spinning at 3000 rpm for 30s. The sample is then baked for 90s at ~110° C on hot plate (or oven) (Figure 2.2.1.b).
3. The sample is transported to the mask aligner (hidden from external light with aluminum foil as the Microposit™ S1813™ Positive Photo Resist is very reactive with ambient light), where the sample and mask are aligned separately and then held together with a vacuum chuck, and is then exposed to UV light (200W) for ~18s (Figure 2.2.1.c).
4. The sample is then developed using the Microposit™ MF™-319 developer. The resist has a developing time of around 60s, giving a nice undercut into the lower resist layer leading to good lift-off. During this time it is possible to check the progress of the developing process using an optical microscope as long as a yellow light filter is in place (Figure 2.2.1.d).
5. At this point the sample is no longer light-sensitive and can be transported to the sputtering chamber to deposit the film (Figure 2.2.1.e). There are no restrictions on the sputtering parameters; however, the more orthogonal the sputtering gun is to the substrate the better the lift-off process.
6. The lift-off process uses acetone, which will remove the Microposit™ S1813™ Positive Photo Resist, along with the unwanted, deposited material. It is usually not necessary to ultrasonically clean the sample in acetone but may prove useful. However, one must take care not to lift-off everything with the ultrasonic approach (Figure 2.2.1.f).

7. The lower layer of Microchem™ PMGI-SF3 will still be present in the presence of acetone; this layer can be left on or removed with the Microchem™ Nano-PMG resist remover (Figure 2.2.1.f).

The etching procedure is similar, but it only uses a single resist layer. The procedure is as follows (see Figure 2.2.2):

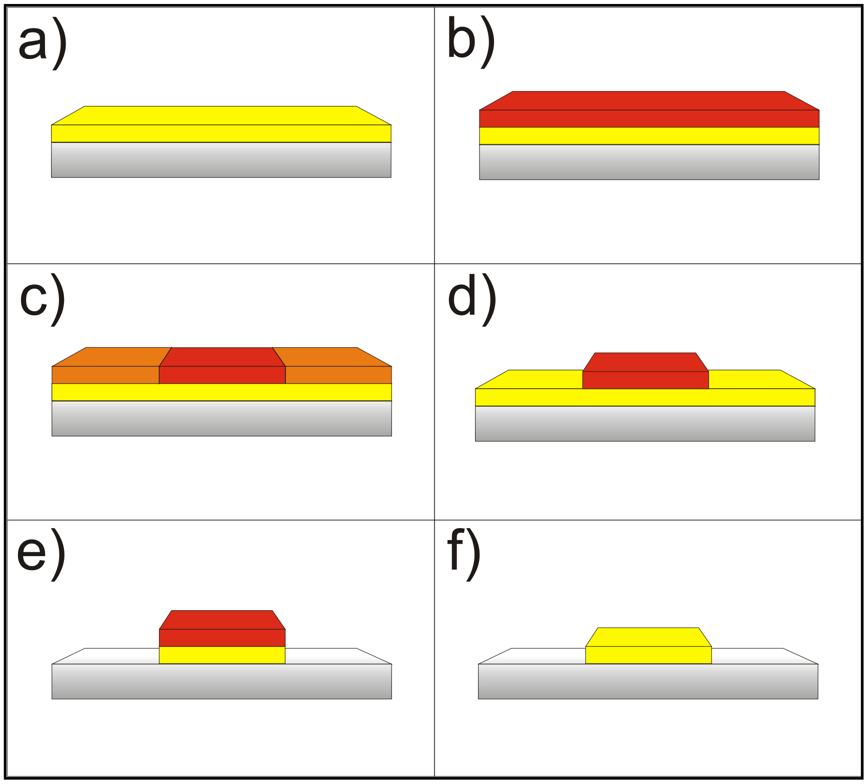

Figure 2.2.2: Photolithography etching process

Visual demonstration of the steps in the photolithography etching process using a single layered photo resist approach. Description of each step can be found in the text.

1. The material for the desired element is sputtered onto a clean substrate (Figure 2.2.2.a).
2. The layer of resist, Microposit™ S1813™ Positive Photo Resist, is spin coated onto the substrate – spinning at 3000 rpm for 30s. On a Corning hot plate (or inside an oven in some cases), the resist is baked at a temperature of ~170° C – this was determined with trial and error (Figure 2.2.2.b).
3. The sample is transported to the mask aligner (hidden from external light with aluminum foil as the Microposit™ S1813™ Positive Photo Resist is very reactive with ambient light), where the sample and mask are aligned separately and then held together with a vacuum chuck, and is then exposed to UV light for ~18s (Figure 2.2.2.c).
4. The sample is then developed using the Microposit™ MF™-319 developer. A developing time of around 60s gave nice sharp features while removing the unwanted resist. During this time it is possible to check the progress of the developing process using an optical microscope as long as a yellow light filter is in place (Figure 2.2.2.d).
5. At this point either a wet or dry etching procedure can be used. For dry etching, the sample is placed in an Argon plasma until the substrate is visible where the removed resist used to be (the sputtered material and hardened resist should remain), this is called Reactive Ion Etching (RIE). For wet etching, a chemical etchant is used (the type of etchant is dependant on the sputtered material). Again, observation of the areas that are intended for removal is achieved with optical

microscopy. Etching was continued until the substrate could be seen (Figure 2.2.2.e).

6. Finally, the resist that remains on top of our sputtered pattern can now be removed with acetone (Figure 2.2.2.f).

A comprehensive list of photolithography recipes and techniques can be found in the *Handbook of Thin Film Technology*, by Leon I. Maissel and Reinhard Glang [2.5].

2.3 X-ray Diffraction

To accurately describe the microscopic structure of solids in which interatomic distances are on the order of an angstrom an electromagnetic probe must have a wavelength of comparable size. Soft X-rays are electromagnetic radiation with a wavelength of 0.5-2.5Å, fulfilling this necessary condition. X-ray diffraction measurements carried out on both a Rigaku D/Max-B Diffractometer and Bruker-AXS D8 Discover High-Resolution Diffractometer with HI-STAR area detector use X-rays that are produced by the bombardment of electrons onto a metallic target. An X-ray tube consists of a source of electrons and two metallic electrodes. A voltage between the electrodes (typically tens of thousands of volts) accelerates electrons rapidly towards the anode. This bombardment of electrons on the anode with a sufficiently high velocity produces X-rays, consisting of a superposition of continuous and characteristic spectra. The continuous spectrum is produced by the rapid deceleration of electrons striking the anode; collisions with nuclei produce deflections of the beam electrons radiating X-ray photons (Bremstahlung radiation). If an electron bombarding the anode has enough energy, it can eject an electron out of the K shell (usually done with Cu, but holds true for other materials), leaving the anode atom in an excited state. One of the outer electrons (in the L, M,... shells) falls into the vacancy in the K shell, emitting a photon and producing one of the characteristic lines (Kα, Kβ,...), depending on where the electron came from. The intensity of ratios corresponds to $K\alpha_1$:$K\alpha_2$:K_β = 10:5:2, showing that only the core shell electrons are necessary for consideration. In fact, for practical purposes, only the $K\alpha_1$ is typically considered. For a Cu anode or target, the Kα (electron transitions from L to K edge) line has a wavelength of about 1.54Å, which is typically used in X-ray diffraction [2.6].

When looking at a crystalline solid, all atoms act as scattering centers for X-rays. If these atoms are regularly arranged, resonant processes can occur to give resonant-type peaks. There are two equivalent methods of interpreting the scattering of X-rays from a periodic structure, one proposed by Bragg and the other von Laue. This discussion will focus on the approach set forth by Bragg. Bragg found that for crystalline materials, intense peaks of scattered radiation were observed for certain sharply defined wavelengths and incident directions [2.7]. This was explained by considering a crystal as a set of parallel plans of atoms, spaced a distance d apart. When a beam of monochromatic X-rays is incident onto a periodic structure, the incident X-rays will be scattered by the atoms in all directions, for some of the incident directions the scattered X-ray beams will be specularly reflected by any one plane of atoms and the reflected rays from successive adjacent planes will interfere constructively. The path difference between these two rays is $2d\sin\theta$, where θ is the angle of incidence. For the rays to constructively interfere, this path difference must be an integral number of wavelengths, leading to

$$n\lambda = 2d\sin\theta, \tag{2.3.1}$$

known as the Bragg condition. In X-ray diffraction measurements, the angle between the diffracted beam and the transmitted beam is always *2θ*. This is known as the diffraction angle, and it is this angle, rather than *θ*, which is usually measured experimentally (Figure 2.3.1).

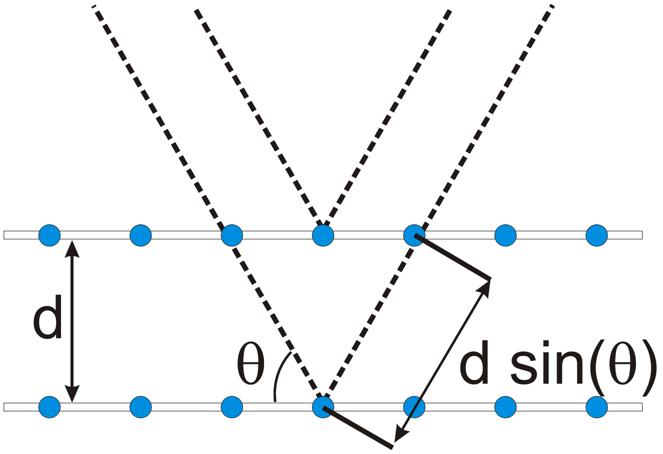

Figure 2.3.1: Bragg diffraction

Schematic of the diffraction by a crystal, which can be considered a set of parallel planes separated by a distance *d*. For an incident angle of θ for the incoming X-ray, the path difference between successive planes is given by $2d\sin\theta$. If this path difference in equal to $n\lambda$ constructive interference will occur.

A solid material can be defined as a crystal composed of atoms arranged in a three dimensional periodic pattern. This periodicity results in strong constructive interference peaks that occur for certain, specific directions. Following the Bragg formulation, one can describe the orientation of any plane produced by this ordered array of atoms by the vector normal to that plane. Since reciprocal lattice vectors, by definition, are normal to any family of lattice planes, it is convenient to pick a reciprocal lattice vector to represent the normal vector. To make the choice of reciprocal vector unique, the shortest vector is chosen, where the indices of the vector are referred to as Miller indices (hkl). For the easiest case of a simple cubic structure, the reciprocal lattice is also simple cubic, where the Miller indices refer to the vector normal to the identified plane. For example, the plane with normal vector <111> has Miller indices (111), as seen in Figure 2.3.2.

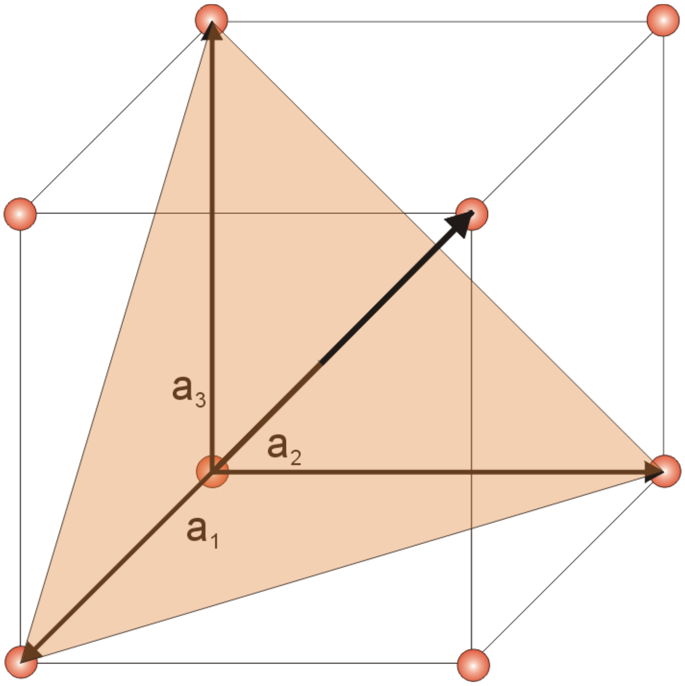

Figure 2.3.2: Simple cubic lattice showing (111) Miller indices

Simple cubic lattice showing the Miller (111) indices for the shown plane coincide with the normal vector <111> to this plane. The basis vectors a_1, a_2 and a_3 represent the 3 simple cubic lattice parameters. For a simple cubic lattice the magnitude for each is the same and the directions are all orthogonal.

Then, the distance between two hkl planes is given by

$$d_{hkl} = \frac{a}{\sqrt{h^2 + k^2 + l^2}} = \frac{n\lambda}{2\sin\theta}, \tag{2.3.2}$$

where a is the cubic lattice constant. In X-ray diffraction, peaks will occur when a particular lattice plane is normal to the scattering vector ($\mathbf{k}_F - \mathbf{k}_i$, perpendicular to sample surface for a specularly reflected beam) of the X-rays, where the position of the peak in 2θ will correspond to a distance d_{hkl}, the distance between planes, by equation 2.3.2. Thus, by identifying the diffraction peaks it is possible to determine the crystal structure of a sample. The intensities and widths of diffracted peaks can give you some information about the positions of atoms within the unit cell and grain size [2.6], where grain size is determined, in the simplest case, by the Debye-Scherrer equation

$$t = \frac{0.9\lambda}{\Delta\cos\theta}. \tag{2.3.3}$$

t is the grain size, λ is the wavelength of X-rays, Δ is the FWHM of the peak and θ is the peak location.

For the case of thin films, low angle X-ray diffraction can give insight into the thickness for single films, repeated bilayers and even more complicated thin-film structures (*i.e.* superlattices and other repeated structures). A change in material density (at an interface between two materials) leads to a change in the index of refraction, which will lead to reflection and transmission of the X-rays (for this reason this technique is often called X-ray reflectivity, XRR). The path difference between these interfaces also satisfies the Bragg condition and a value for *d*, the distance between the two interfaces, can be measured. For an infinitely thick sample with a perfectly flat interface, one sees the expected Fresnel reflectivity.

Fresnel Reflectivity

When an X-ray beam impinges on a flat material, part of the incoming intensity is reflected and part of it is transmitted through the material. If the surface of the reflecting material is flat, the reflected intensity will be confined in a direction symmetric from the incident one and will be labeled as specular. X-ray reflectivity validity is limited to small angles of incidence where it is possible to consider the electron density as continuous. In this approximation, the reflection can be treated as a classical problem of reflection of an electromagnetic wave at an interface. The reflected amplitude is obtained by writing the continuity of the electric field and of the magnetic field at the interface. This leads to the Fresnel relationship, which gives the reflection coefficient in amplitude for the **s** and **p** polarization. The reflectivity, which is the modulus square of this coefficient, can be formulated in the case of X-rays as

$$R(\theta) = rr^* = \left| \frac{\theta - \sqrt{\theta^2 - \theta_c^2 - 2i\beta}}{\theta + \sqrt{\theta^2 - \theta_c^2 - 2i\beta}} \right|^2 , \qquad (2.3.4)$$

where β is the absorption coefficient and θ_c is the critical angle. This expression is independent of the polarization [2.8].

For a thin film, oscillations occur in the reflectivity due to interference between reflections from the two interfaces, where these two interfaces will be the substrate/film and film/air interfaces. The difference in *2θ* between successive maxima (or minima) relates to the thickness of the film via Bragg's condition. With a wavelength of 1.54Å, this is an extremely accurate method for determining film thickness down to a few monolayers. In addition, this technique allows one to measure thickness and roughness of individual layers in a multilayer stack. [2.6]

Typically, XRR involves a complicated fitting routine done using fitting software with complicated algorithms; a software package from Bruker AXS called Leptos was used, which incorporates advanced X-ray scattering models and numerical methods into the package. This software allows for analysis of extremely complicated heterostructure materials, and can factor in density changes, interface roughness and instrument resolution that are difficult to analyze directly. However, for simple films there are many things that can be attained from a direct analysis, a brief example will show some of the parameters that can be obtained for a single thin film. Assuming a grazing incidence angle, the average scattering (the atoms are no longer considered discrete at small angles – but a continuous electron density) is measured and gives an index of refraction based on the electron density. The index of refraction for X-rays in any medium is always less than 1 and has both real and imaginary parts such that

$$n = 1 - \delta - i\beta, \tag{2.3.5}$$

with dispersion factor

$$\delta = \left(\frac{\lambda^2}{2\pi}\right) r_e N_a \rho \left(\frac{Z + f'}{A}\right) = \left(\frac{\lambda^2}{2\pi}\right) r_e \rho_e \tag{2.3.6}$$

and absorption factor

$$\beta = \left(\frac{\lambda^2}{2\pi}\right) r_e N_a \rho \left(\frac{f''}{A}\right) = \frac{\lambda}{4\pi}\mu. \tag{2.3.7}$$

λ is the X-ray wavelength, r_e is the classical electron radius, N_a is Avagadro's number, Z is the average atomic number, A is the average atomic mass, ρ_e the electron density, μ the linear absorption coefficient, and *f'* and *f''* are the real and imaginary part of the average dispersion corrections, respectively.

Then, according to Snell's law (see Figure 2.3.3)

$$\frac{\cos\theta_i}{\cos\theta_t} = \frac{n}{n_0}. \tag{2.3.8}$$

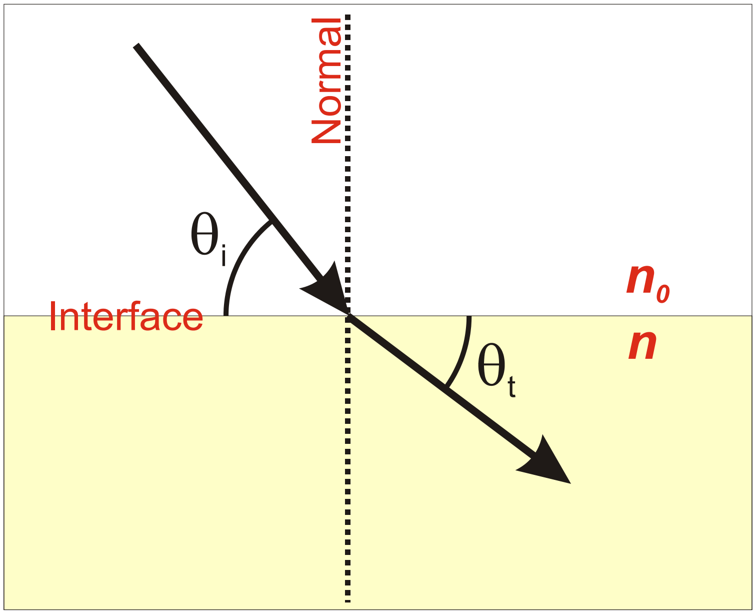

Figure 2.3.3: Snell's law

Refraction of X-rays at the interface between two media of different refractive indices, with $n < n_0$. Since the phase velocity is higher in the second medium, the angle of refraction θ_t is less than the angle of incidence θ_i; that is, the ray in the lower-index medium is further away

> from the normal (notice that the angle convention is different from the traditional explanation of Snell's law). This implies that there is a critical incident angle, where any incidence at an angle below this angle will result in total external reflection.

At the critical angle of total external reflection, $\theta_t = 0$ and $n_0 = 1$, then neglecting absorption,

$$n = 1 - \delta = \cos\theta_i = \cos\theta_c \,. \tag{2.3.9}$$

Expanding the cosine for small angles gives

$$\begin{aligned} \cos\theta_c &= 1 - \frac{\theta_c^2}{2} = 1 - \delta \\ \theta_c &= \sqrt{2\delta} \end{aligned} \,. \tag{2.3.10}$$

A simple approach to determine the critical angle from an XRR scan is to define the critical angle where the intensity of the reflected beam is at half intensity, or when $I = I_{\max}/2$. This will be located at or near the 'critical edge', which signifies a drop off in the Fresnel reflectivity at the critical angle.

From this determination of critical angle there are a variety of useful parameters of a single film sample that can be determined. First, the mass density can be determined experimentally from the critical angle using Eq. 2.3.6, where

$$\rho\left(\frac{g}{cm^3}\right) = \frac{\theta_c{}^2 \pi A}{N_a r_e (Z + f')\lambda^2} = 1.851 \times 10^5 \frac{\theta_c{}^2 A}{(Z + f')\lambda^2} \,, \tag{2.3.11}$$

and λ is in Angstroms. Next, the film thickness can be determined by using a modified Bragg condition. To determine thickness, the interference peak positions must be determined. Occasionally it is quite difficult to see the small oscillations on the Fresnel reflectivity background. For this reason it is often convenient to remove this contribution, which is often referred to as stripping off the K^4 signature, where K is the scattering vector, $K = (4\pi/\lambda)\sin\theta$. Thus, the modified reflected intensity I_{mod} is

$$I_{\text{mod}} \propto I \sin^4 \theta_i . \tag{2.3.12}$$

This scaling will make it significantly easier to identify the maxima and minima positions of the reflectivity data. Once the maxima or minima positions have been determined, the modified Bragg equation

$$(m + \Delta m)\lambda = 2t\sqrt{\sin^2 \theta_m - 2\delta} \tag{2.3.13}$$

allows for the calculation of both the thickness and potentially the critical angle (if the first order reflectivity peak is known – sometimes difficult to determine). Assuming the first order reflectivity peak is known exactly, then

$$(m + \Delta m)\lambda = 2t\sqrt{\sin^2 \theta_m - \theta_c^{\ 2}} \tag{2.3.14}$$

and assuming small angles

$$\sin^2 \theta_m = \theta_m^{\ 2} = \theta_c^{\ 2} + \frac{\lambda^2}{4t^2}(m + \Delta m)^2 , \tag{2.3.15}$$

where m is the exact reflection order (1,2,3,…) and Δm has values ½ for maxima and 0 for minima if $\rho_{\text{film}} > \rho_{\text{substrate}}$ and values 0 for maxima and ½ for minima if $\rho_{\text{substrate}} > \rho_{\text{film}}$. A $\theta_m^{\ 2}$ vs. $(m + \Delta m)^2$ plot can be made and the slope will reveal the thickness and the y-intercept gives the critical angle squared, where

$$t = \frac{\lambda}{2\sqrt{slope}} . \tag{2.3.16}$$

If one is unable to determine the first order peak, then the critical angle must be determined in another way (previously discussed methods) and then the modified Bragg condition can again be used, where

$$(m+\Delta m)=\frac{2t}{\lambda}\sqrt{\sin^2\theta_m-\theta_c{}^2}\,. \tag{2.3.17}$$

The slope of an $(m+\Delta m)$ vs $\frac{2}{\lambda}\sqrt{\sin^2\theta_m-\theta_c{}^2}$ plot reveals the thickness of the film. Again, these techniques are very simplified for single films but it gives an idea of the type of analysis required for films with even greater complexity.

Finally, in repeated bilayer structures, it is also possible to determine bilayer thickness based on a superlattice peak. For a particular angle in *2θ*, the contributions from the interference pattern in reflectivity for a repeated bilayer add up to give a peak. The intensity of this peak increases with an increasing number of bilayers. This superlattice peak satisfies the Bragg condition for the bilayer thickness, where the thickness of the bilayer is given by

$$t=\frac{n\lambda}{2\sin\theta}, \tag{2.3.18}$$

where n implies that there are multiple order superlattice peaks (the order of peaks gives insight into interface roughness between bilayers). Using an off-specular technique, where θ and 2θ have an offset (usually between 0.1 to 1 degrees), one can remove the thickness oscillations and be left with only the Fresnel reflectivity curve accompanied by the superlattice peaks. This approach is an extremely accurate method for determining film thicknesses.

2.4 Magneto-Optic Kerr Effect (MOKE)

When light is reflected off a magnetized surface a change in reflectivity, polarization and ellipticity occurs. This is identical to the Faraday Effect, except MOKE measures the reflected light as opposed to the transmitted light. Both effects occur due to off diagonal components of the dielectric tensor. For measurement in this setup, a lock-in technique is used with a photo-elastic modulator (PEM).

The Kerr effect is proportional to the component of magnetization along the propagation direction; in the first order approximation, a hysteresis loop of the magnetization can be obtained. There are three basic MOKE configurations that are used in determining the magnetic behavior of a thin-film sample; these three configurations are shown in figure 2.4.1 and described below.

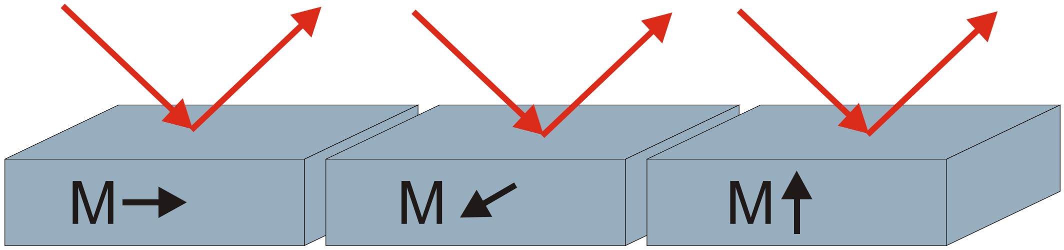

Figure 2.4.1: MOKE configurations

Three MOKE configurations – Longitudinal, Transverse and Polar, where the red arrows represent the propagation direction of the light and the black arrows represent the magnetization direction.

2.4a Longitudinal MOKE (LMOKE)

In LMOKE, the measured magnetization vector is parallel to the plane of the film and is parallel to the incident plane of light. When a beam of light with **s**-polarization (the electric field vector is perpendicular to the incident plane) or **p**-polarization (the electric field vector is parallel to the incident plane) is incident onto the sample surface, on reflection, the beam is converted to elliptically polarized light due to an additional component perpendicular to the incident electric field vector which is induced by the magnetization. For LMOKE the laser beam should be as far from normal incidence as possible, keeping in mind the spot size (foot print of the laser spot). This measures the largest component of magnetization vector assuming the magnetization has an in-plane easy axis or the applied field is sufficient to pull the magnetization into the plane. Obviously, no effect is observed for a normally incident beam (See Figure 2.4.2).

2.4b Transverse MOKE (TrMOKE)

In TrMOKE, the measured magnetization vector is parallel to the plane of the film and is perpendicular to the incident plane of light. TrMOKE only occurs for incident light with **p**-polarization. The reflected light is also **p**-polarized but there is a change in the reflected amplitude as the magnetization vector changes sign, where the reflectivity R changes from $R + \Delta R$ to $R - \Delta R$. Again, the laser beam is far from normal incidence.

2.4c Polar MOKE (PMOKE)

In PMOKE, the measured magnetization vector is perpendicular to the plane of the film and parallel to the incident plane of light. When a light beam with **s** or **p** polarization is incident on the sample surface, the reflected light will be elliptically polarized due to the induced Kerr component. For this measurement it is best to have the laser beam directly at normal incidence.

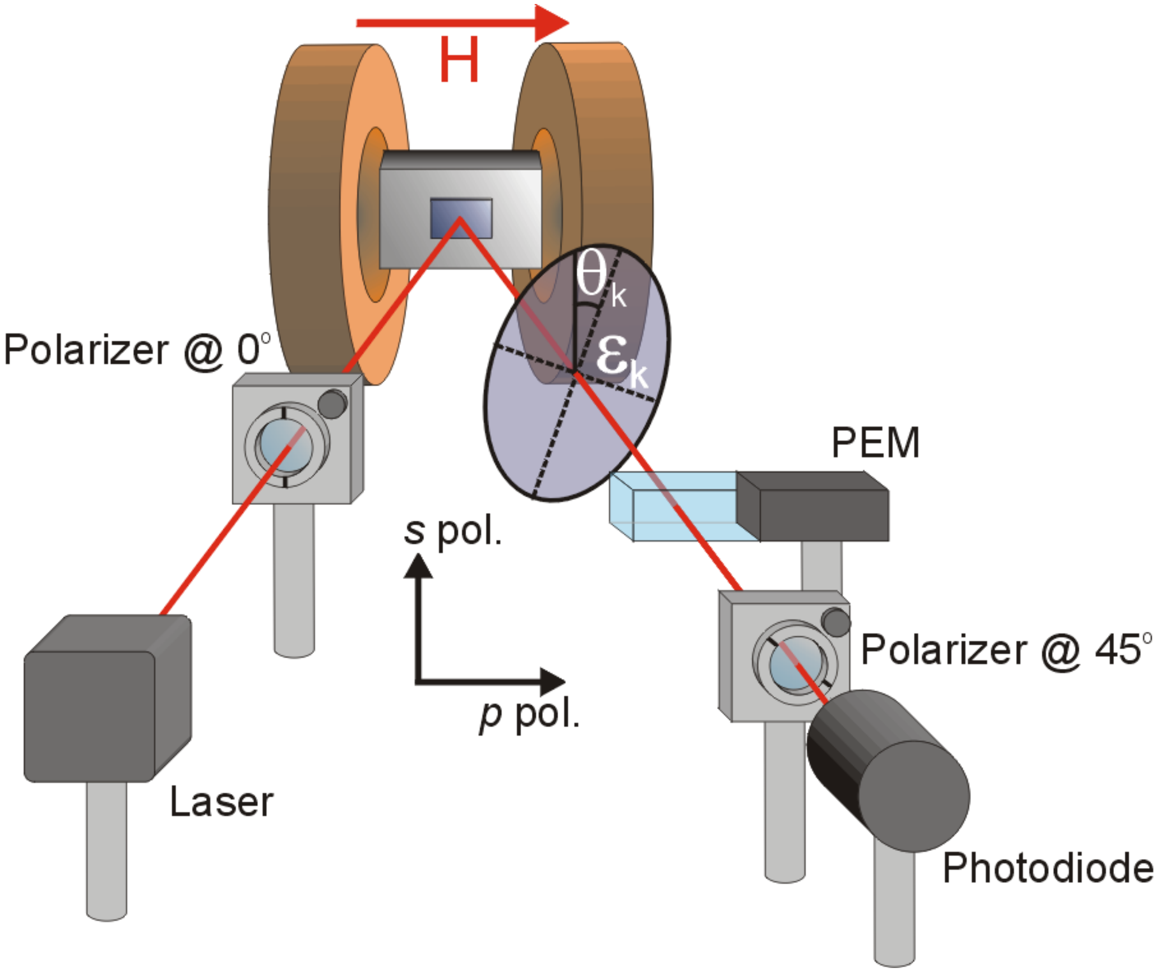

Figure 2.4.2: Experimental configuration for longitudinal MOKE

Experimental configuration for longitudinal MOKE (similar for perpendicular MOKE if the applied field H was out of the page). The light passes from the laser through the polarizer at either 0 or 90°, depending on whether the user wants **s** or **p** polarization. The light is then reflected from the magnetic sample surface with the addition of a polarization rotation θ_k

and change in ellipticity εk. It then passes through the photoelastic modulator (with principle axis along 0°) and another polarizer at 45° before it is measured with a photodiode.

2.4d MOKE with PEM Derivation

In both PMOKE and LMOKE the polarization of the reflected light is altered. Specifically, an ellipticity ε_k is introduced and the plane of polarization is rotated by an angle θ_k. Both of these values are exceedingly small, thus small angle approximations will be used.

Considering incident laser light with **p**-polarization, the Stokes vector $\mathbf{A_i}$ is

$$\mathbf{A_i} = \begin{bmatrix} 1 \\ 1 \\ 0 \\ 0 \end{bmatrix}. \tag{2.4d.1}$$

Upon reflection from the magnetic sample the plane or polarization is rotated by θ_k and ellipticity ε_k has been introduced. From Kliger, Lewis and Randall elliptically polarized light with rotation θ_k and ellipticity ε_k follows equations 5.48 and 5.49 [2.9]

$$\varepsilon_k = \tan\left[\frac{1}{2}\sin^{-1}\left(\frac{V}{I}\right)\right] \approx \frac{V}{2I} = \frac{v}{2} \tag{2.4d.2}$$

and

$$\theta_k = \frac{1}{2}\tan^{-1}\left(\frac{U}{Q}\right) \approx \frac{U}{2Q} = \frac{u}{2q}. \tag{2.4d.3}$$

I, Q, U and V are the components of the Stokes vector and q,u, and v are the normalized components where q=Q/I, etc. In the incident bean Q=1 and thus q =1. To first order, this is maintained in the reflected beam since θ_k and ε_k are very small. However, solving for u and v

$$u \approx 2\theta_k \tag{2.4d.4}$$

and

$$v \approx -2\varepsilon_k \,. \tag{2.4d.5}$$

This qualitatively makes sense as the formalism for Stokes vectors is

$$\mathbf{A} = \begin{bmatrix} P_{0^\circ} + P_{90^\circ} \\ P_{0^\circ} - P_{90^\circ} \\ P_{45^\circ} - P_{-45^\circ} \\ P_{RCP} + P_{LCP} \end{bmatrix}, \tag{2.4d.6}$$

where P is the intensity of the various polarization states. Introducing the Kerr components into the reflected beam defines the new reflected beam's Stokes vector $\mathbf{A}_{\mathbf{r1}}$, where

$$\mathbf{A}_{r1} = \begin{bmatrix} 1 \\ 1 \\ 2\theta_k \\ -2\varepsilon_k \end{bmatrix}. \tag{2.4d.7}$$

This reflected beam then travels through the PEM and finally a polarizer at 45°. The Mueller matrix for a PEM at 0° is

$$\mathbf{M}_{\mathbf{PEM}} = \begin{bmatrix} 1 & 0 & 0 & 0 \\ 0 & 1 & 0 & 0 \\ 0 & 0 & \cos(A) & \sin(A) \\ 0 & 0 & -\sin(A) & \cos(A) \end{bmatrix}, \tag{2.4d.8}$$

where $A = A_0 \sin(\omega t)$ is the time dependent (50 kHz) retardation of the PEM. Then, the light after passing through the PEM has Stokes vector

$$\mathbf{A}_{\mathbf{r2}} = \mathbf{M}_{\mathbf{PEM}} \mathbf{A}_{\mathbf{r1}} \begin{bmatrix} 1 \\ 1 \\ 2\cos(A)\theta_k - 2\sin(A)\varepsilon_k \\ -2\sin(A)\theta_k - 2\cos(A)\varepsilon_k \end{bmatrix}. \tag{2.4d.9}$$

The next component is the 45° polarizer, with Mueller matrix

$$\mathbf{M}_{+45} = \frac{1}{2} \begin{bmatrix} 1 & 0 & 1 & 0 \\ 0 & 0 & 0 & 0 \\ 1 & 0 & 1 & 0 \\ 0 & 0 & 0 & 0 \end{bmatrix}. \tag{2.4d.10}$$

Thus, the Stokes vector reaching the detector is

$$\mathbf{A}_{\mathbf{r3}} = \mathbf{M}_{+45} \mathbf{A}_{\mathbf{r2}} = \begin{bmatrix} \frac{1}{2} + \cos(A)\theta_k - \sin(A)\varepsilon_k \\ 0 \\ \frac{1}{2} + \cos(A)\theta_k - \sin(A)\varepsilon_k \\ 0 \end{bmatrix}. \tag{2.4d.11}$$

The first entry in A_{r3} is proportional to the intensity reaching the detector versus time. The average intensity is defined as I_0, then

$$I(t) = I_0\left[1 + 2\cos(A_0 \omega t)\theta_k - 2\sin(A_0 \omega t)\varepsilon_k\right]. \tag{2.4d.12}$$

Expanding in Fourier series,

$$\cos(A) = J_0(A_0) + 2J_2(A_0)\sin(2\omega t) + \cdots, \tag{2.4d.13}$$

$$\sin(A) = 2J_1(A_0)\sin(\omega t) + \cdots, \tag{2.4d.14}$$

then

$$I(t) \cong I_0\left[1 + 2\theta_k J_0(A_0) - 4\varepsilon_k J_1(A_0)\sin(\omega t) + 4\theta_k J_2(A_0)\cos(2\omega t) + \ldots\right], \tag{2.4d.15}$$

where ω is the angular frequency, $\omega = 2\pi f$, of the PEM, A_0 is the amplitude of retardation in the PEM and J_n are the Bessel functions. Choosing A_0 to be 2.405 radians eliminates the second term leaving a DC term ($V_{DC} = I_0$), a first harmonic term ($4\varepsilon_k J_1(A_0)\sin(\omega t)$), which determines the ellipticity, and a second harmonic term ($4\theta_k J_2(A_0)\cos(2\omega t)$), which determines rotation. Reading in voltages from each of these three contributions allows a direct measure of θ_k and ε_k, where

$$\theta_k = \frac{\sqrt{2}}{4J_2}\frac{V_{2f}}{V_{DC}} \text{ and } \varepsilon_k = \frac{\sqrt{2}}{4J_1}\frac{V_{1f}}{V_{DC}}. \qquad (2.4d.16)$$

The $\sqrt{2}$ factor assumes the lock-in gives the RMS voltage, while the theory presented assumes the voltage amplitude.

By plotting either of these two signals versus applied field, a magnetic hysteresis loop of the sample can be obtained. Plus, it's been shown that by making the proper choice of polarization and direction of the applied field, the in-plane and out-of-plane components of magnetization can be obtained separately. Since MOKE is not necessarily a quantitative approach to determine magnetization, the data is typically expressed as M/M_s. MOKE is an excellent approach to determine coercivity values and to determine loop shape.

To find the variation in magnetic properties with temperature, the use of a Janis closed-cycle refrigerator with polarization preserving optical windows was used (Model CCS-450). In practice, this allows MOKE data to be taken over a temperature range of 30K to 475K. However, the added constraint for laser light (getting the light into and out of the vacuum jacket) made it difficult to use this device along with the soft iron pole pieces of the electromagnet (used to enhance the magnetic field) in the LMOKE setup. Thus, a limit on applied field made it difficult to take measurements at the extremely low temperature range, where coercivities became too large. On the other hand, by drilling holes through the center of the pole pieces it was possible to use them in the PMOKE setup and we were able to take measurements throughout the entire temperature range.

2.5 Magnetic Force Microscopy (MFM)

Magnetic Force Microscopy (MFM) images the spatial variation of magnetization on a sample surface. This allows one to look at the local magnetic landscape on the nanometer scale, similar to a topographical landscape using known techniques in atomic force microscopy. With this spatial resolution it is possible to image naturally occurring or deliberately written magnetic domains.

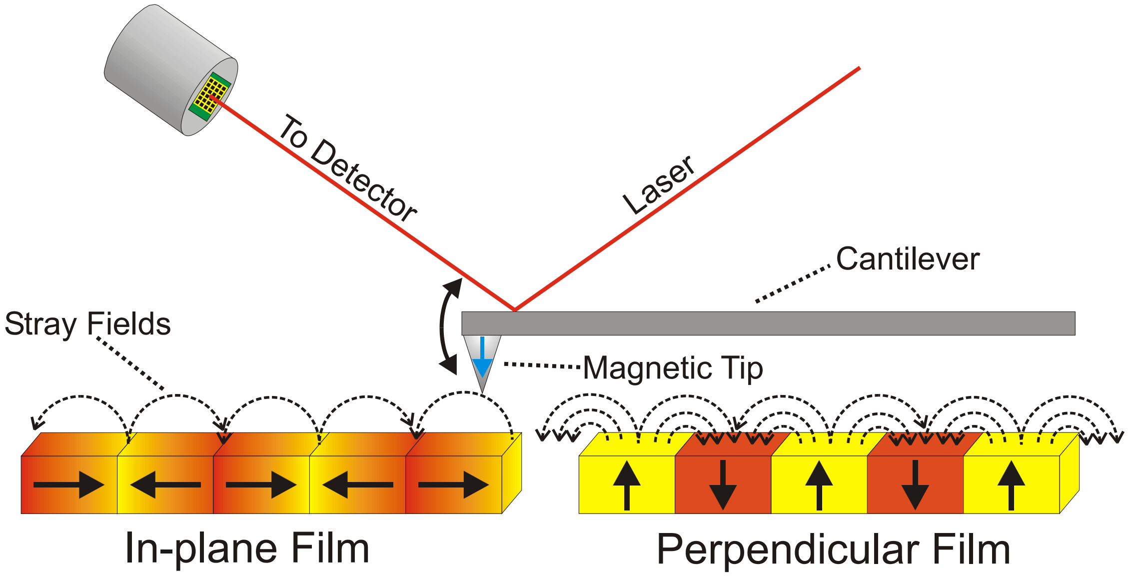

Figure 2.5.1: Schematic of MFM

Schematic view of magnetic force microscopy for films with in-plane and out-of-plane easy axes.

An MFM system consists of a flexible cantilever suspended from one end. On the free end, a small, sharp magnetic tip is mounted. When a magnetic sample is close to the tip, due to the stray fields induced by the nonuniform distribution of the magnetization in the sample, a magnetic force acts on the magnetic tip (See Figure 2.5.1). With this force a measurable change in the cantilever occurs, whether deflection or a shift in resonant frequency. Using a laser reflection technique off of the cantilever, deflection detection of the laser spot is used to measure cantilever motion and ultimately measure the force gradient. The forces attributable to topography and dispersive forces still apply. To form an image, the sample-tip interaction is mapped as a function of position by mechanically scanning the sample relative to the tip in a line-by-line pattern. Software separates the force contributions from the topography and the local magnetization, assuming relatively small topographical changes.

If the magnetic tip is considered a point dipole, then the force **F** acting on the tip is given by the gradient of the energy

$$\mathbf{F} = \int_V \nabla(\mathbf{M} \cdot \mathbf{H}) dV \tag{2.5.1}$$

where **M** is the magnetization of the tip, **H** is the stray field from the sample and *V* is the volume of the magnetic material on the tip. Since **M** is not well characterized, MFM is not a quantitative analysis. In the absence of currents $\nabla \times \mathbf{H} = 0$ and assuming the cantilever is constrained to be only in the z-direction, eqn. 2.5.1 can be rewritten as

$$F_z = \int_V M_z \frac{\partial H_z}{\partial z} dV \,. \tag{2.5.2}$$

This relates the measured force with the local stray fields. The simplest approach to determine the local magnetic force is to simply measure a static deflection of the cantilever at a particular position; however, since the magnetostatic forces between the magnetic tip and magnetic sample are long-range forces (10 to 100 nm), a more sensitive technique is necessary. As seen in eqn 2.5.2, the force is proportional to the first derivative of the stray fields; the force gradient is proportional to the second derivative of the individual components of the field. In practice, it is assumed that the tip's magnetic dipole moment is along the z-axis. Thus,

$$\mathbf{F}' = \frac{d\mathbf{F}}{dz} = \int_V M_z \frac{\partial^2 H_z}{\partial z^2} dV , \tag{2.5.3}$$

which is the most widely used relation for MFM contrast. MFM measures the force gradient by oscillating the cantilever normal to the surface at its resonant frequency. In the absence of magnetic force, the cantilever has a resonant frequency ω_0. In the presence of a magnetic force, this frequency is shifted by an amount $\delta\omega$, proportional to the vertical gradients in the magnetic force on the tip. The shifts in resonant frequency tend to be very small, typically in the range of 1-50 Hz for cantilevers having a resonant frequency of $\omega_0 \sim$ 100kHz. These frequency shifts can be detected in three ways: amplitude detection, frequency modulation and phase detection. For our purposes we used frequency modulation, which gives good signal-to-noise ratios and reduced artifact content. In this method, the cantilever's modulated frequency is measured relative to that of the resonant frequency and is related to the force gradient. As the force gradient changes, the spring constant k_0 causes a shift in the resonant frequency. The resonant frequency $\omega_0' = \omega_0 \pm \delta\omega$ in the presence of F' is given by

$$\omega_0' = \sqrt{\frac{k_{eff}}{m}} = \sqrt{\frac{k_0 - F'}{m}} , \tag{2.5.4}$$

where k_0 is the natural cantilever spring constant and m is the effective mass. F' is much smaller than k_0, thus ω_0' can be expressed as

$$\omega_0' = \omega_0\left(1 - \frac{F'}{2k_0}\right) \tag{2.5.5}$$

and

$$\delta\omega = -\frac{\omega F'}{2k_0} \tag{2.5.6}$$

is the measured shift.

The force gradient and its sign can be detected directly by measuring the frequency shift from the resonant frequency. This shift is then converted to a color variation (chosen to be a red to yellow variation in this example) that depicts the magnitude of the local magnetization and its sign. Generally, the red (yellow) contrast is chosen for attractive (repulsive) interactions between the magnetic tip and the local magnetization. From the resulting image it is possible to obtain the distribution of stray fields above the sample surface (Figure 2.5.1). Notice that the stray field profile is quite different for the in-plane film compared to a perpendicular film, where in the former case the contrast is only evident in the vicinity of the domain wall but for the latter more sharp transitions between domains is observed. For a more in-depth look at MFM please refer to the following references. [2.10-2.12].

2.6 X-ray Magnetic Circular Dichroism (XMCD) and XMCD-Photoemission Electron Microscopy (PEEM)

XMCD exploits the dichroic nature of magnetic materials, where originally the term ‘dichroism’ was used to describe materials that preferentially absorbed one color of light, leading to two different colors for two light directions. The term has come to be more general and describes the dependence of photon absorption based on the polarization state. In the case of XMCD, where dichroism occurs due to anisotropies in the spin in the material, the dependence of X-ray absorption on the helicity of the X-ray beam by a magnetic material is measured. With X-ray absorption spectroscopy (XAS) there is element specificity in this approach and the XMCD gives magnetic sensitivity. XMCD-PEEM allows us to have both the element specificity and the magnetic sensitivity with spatial resolution.

2.6a X-ray Absorption Spectroscopy (XAS)

The use of X-rays, and principles of X-ray Absorption Spectroscopy (XAS), allow us to pick apart a sample element by element due to the energy dependent nature of the absorption of photons. Third generation synchrotron radiation sources supply large intensities of energy dependent photons in the soft to hard X-ray regime allowing for a simple method to determine the elemental composition of a sample. Spectra can be obtained in two modes, total electron yield (TEY) or total fluorescence yield (TFY). For surface-sensitive and element-specific information on thick samples, TEY mode is the method of choice, where TEY is the electrical current necessary to keep the sample at a fixed potential during the ejection of photoelectrons. TFY mode has bulk sensitivity and looks at the fluorescence photons using a fluorescence detector. Since XAS is governed by dipole selection rules, the d-shell properties (important for magnetism, as discussed below) are best probed by L-edge absorption studies (2p to 3d transitions) for the 3d transition metals (Ni, Fe, Co). The L-edge X-ray absorption spectra of the transition metals and oxides are dominated by two main peaks (L_3 and L_2, arising from the transition from $2p_{3/2}$ and $2p_{1/2}$, respectively, to 3d valence holes) separated by about 15 eV as shown in Fig. 2.6a.1. The two main peaks in the spectra arise from the spin orbit interaction of the 2p core shell and the total intensity of the peaks is proportional to the number of empty 3d valence states. The metal spectra mainly show two broad peaks, reflecting the width of the empty d-bands. The oxide spectra exhibit considerable fine structure, called multiplet structure (See Figure 2.6a.1).

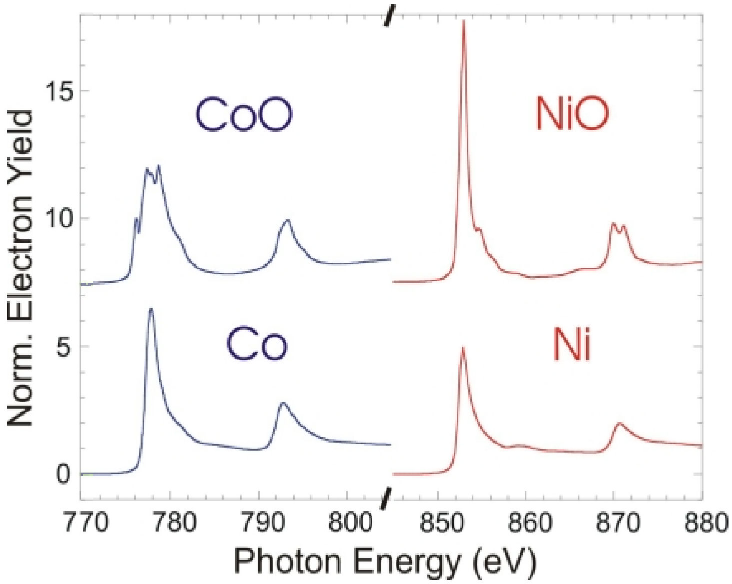

Figure 2.6a.1: X-ray Absorption Spectroscopy

X-ray Absorption Spectra for Co and Ni about the L_3 and L_2 peaks. The metallic Co and Ni have two broad peaks, while the oxides CoO and NiO show multiplet structure in both the L_3 and L_2 peaks [Figure taken from J. Stöhr, reference 2.13].

2.6b XMCD

For magnetic studies, measuring the XMCD signal is done by taking XAS spectra for both right handed (RCP) and left handed (LCP) circularly polarized X-rays. The XMCD signal is then given by

$$I_{XMCD} = \frac{I_{RCP} - I_{LCP}}{I_{RCP} + I_{LCP}}, \qquad (2.6b.1)$$

where *I* is the TEY or TFY intensity for a given polarization. This XMCD signal is due to a two-step process proposed by Stöhr and Wu [2.14]. First, right or left circularly polarized photons transfer their angular momentum to the excited photoelectron. If this photoelectron originated from either the $2p_{3/2}$ or $2p_{1/2}$, the angular momentum of the incoming photon can be transferred in part to the spin through the spin-orbit coupling, where RCP and LCP transfer opposite momentum and thus photoelectrons with opposite spins are created. Thus, the core shell can be viewed as an atom specific source of spin-polarized electrons. Since the $2p_{3/2}$ and $2p_{1/2}$ levels have opposite spin-orbit coupling (l+s and l-s, respectively), the spin polarization will be opposite at the two edges (L_2 and L_3). Now that photoelectrons have been produced, where their spin is controlled by the helicity of the incoming light and the edge they emanated from, the next step (the magnetic step) is when the spin-polarized electrons are analyzed by the spin-resolving 'detector' of the exchange split final d state. A spin-flip is forbidden in electric dipole transitions, thus spin-up (spin-down) photoelectrons from the p core shell can only be excited into spin-up (spin-down) d hole states [2.15]. Thus, the photoelectrons become a probe of the magnetism with element specificity.

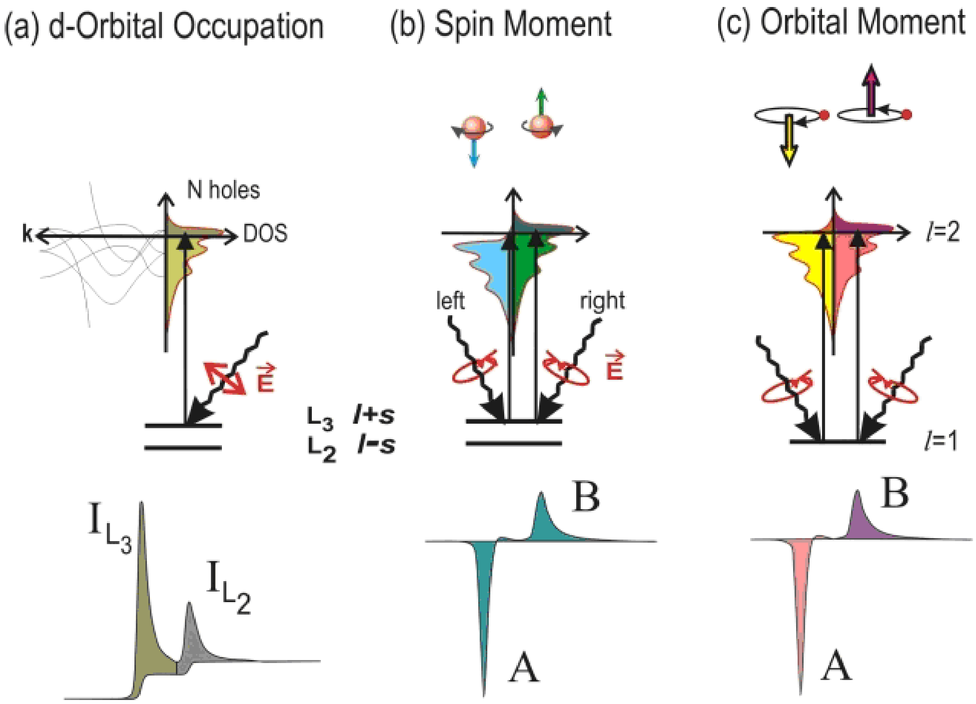

Figure 2.6b.1: X-ray magnetic circular dichroism

(a) Electronic transitions in conventional L-edge X-ray absorption, (b) and (c) X-ray magnetic circular dichroism, illustrated in a one-electron model. The transitions occur from the spin orbit split 2p core shell to empty conduction band states above the Fermi level. In conventional X-ray absorption the transition intensity measured as the white line intensity L_3+L_2 is proportional to the number of d holes, N. By use of circularly polarized X-rays the spin moment (b), and orbital moment (c), can be determined from the dichroic difference intensities A and B, as explained in the text [Figure taken from reference 2.15].

The XMCD data is described through a series of sum rules (shown in Fig. 2.6b.1), which link the experimental integrated intensities of XAS and XMCD spectra to the ground-state expectation values of the orbital and spin magnetic moments of the absorbing atom. The first X-ray absorption sum rule links the total intensity of the L_3 and L_2 resonances with the number N of empty d states (holes). The d valence shell can hold up to 10 electrons which are filled into band states up to the Fermi level and the number of filled states is therefore 10-N (Fig. 2.6b.1a). The second and third sum rules, developed by Thole *et al.* [2.16,2.17], relate the XMCD intensity at A (L_3 edge) and B (L_2 edge) to the spin and orbital moments in the material. The spin moment is related to the XMCD intensity by *A-2B* (Fig. 2.6b.1b) and the orbital moment is related to the XMCD intensity by *A+B* (Fig. 2.6b.1c). These powerful sum rules make it possible to get quantitative information on magnetic materials; however, in practice there are some simplified approaches that can be taken. In general, the XMCD signal can be treated similarly to an optical spectroscopy approach, like MOKE, where absolute values are unnecessary and only changes in magnetization are of interest. In this sense, the intensity of A can be measured versus field, temperature, etc.

2.6c XMCD-PEEM

XMCD-PEEM [2.18-2.20] is the incorporation of electron microscopy with the local electron yield from a sample region allowing us to study element specific magnetization with spatial resolution. The PEEM technique uses the secondary electrons emitted from a sample surface upon the absorption of photons (See Figure 2.6c.1). Synchrotron X-rays provide a direct chemical contrast using the element-specificity of the X-ray absorption edges allowing the probing of a single element within a more complex heterostructure, i.e. multilayered systems and magneto-electronic devices.

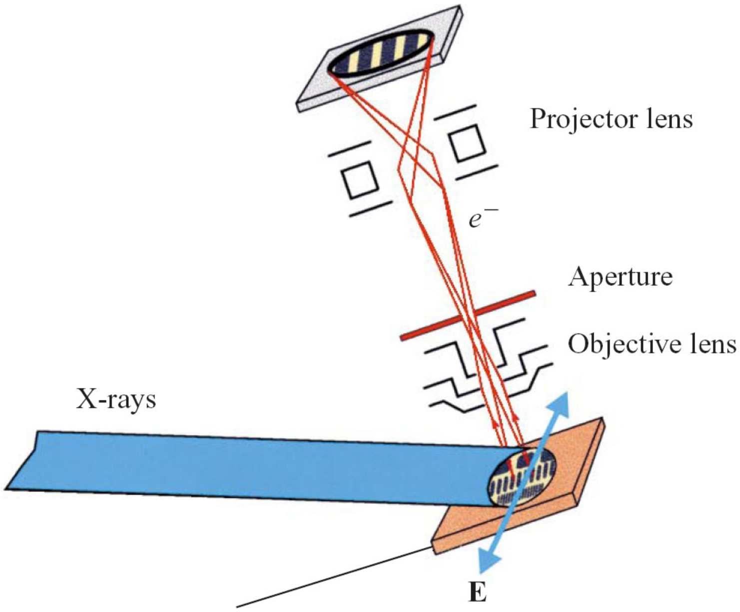

Figure 2.6c.1: Photoemission electron microscopy

Magnetic imaging by means of PEEM. A layer in the sample is selected by tuning the X-ray energy to the desired element. X-ray polarization contrast at an absorption peak is used for imaging contrast. The local electron yield from a sample region, imaged by PEEM, depends on the relative orientation of the magnetic direction or axis and the polarization [Figure taken from J. Stöhr, reference 2.13].

Using the XMCD tools previously discussed along with circularly polarized X-rays, this technique becomes even more powerful in that one can image domain patterns in samples with multiple ferromagnetic, ferrimagnetic, antiferromagnetic, nonmagnetic, etc… layers, each layer can be observed separately. Correlations and interactions can be observed between layers [2.21]. Calculations show that the spatial resolution for PEEM is predicted to be less than 10 nm [2.20,2.22], and a resolution of 8 nm has been demonstrated [2.23]. Further techniques intend to drop this resolution even further [2.24-2.25]. Since a total electron yield technique is used, along with XMCD, this too is also a very surface sensitive measurement, where the 1/*e* sampling depth is about 1.7 nm for Fe and 2.5 nm for Co and Ni, where depths about 3 times these values can still be imaged [2.26]. This tool has quickly become an important 'detective' in correlating spin structures in very complex systems, particularly exchange coupled and exchange biased media. In addition, the time resolution of the third generation synchrotrons allows PEEM imaging to be done at ultrafast timescales (~100 ps).

Similar measurements to XMCD can be achieved for antiferromagnetic materials using linearly polarized light through a process called X-ray Magnetic Linear Dichroism (XMLD). This technique was not used for the purposes of this dissertation (although some attempts were made). This technique can be coupled to PEEM to image antiferromagnetic domains. This is particularly useful for exchange biased systems where a direct observation of domains in the antiferromagnet are coupled to the adjacent ferromagnetic layer [2.21].

2.7 Alternating Gradient Force Magnetometry (AGFM)

The Alternating Gradient Force Magnetometer (AGFM) is a relatively easy method to get magnetic data for the full thickness of a magnetic sample (not surface sensitive). In the AGFM, a sample (needs to be roughly 3mm x 3mm or smaller) is mounted to a piezoelectric transducer which oscillates when the sample is subjected to an alternating magnetic field gradient superimposed on the DC field of an electromagnet, Figure 2.7.1. This technique is considered a force technique, which measures the force on a magnetized sample in the presence of a magnetic field gradient. The piezoelectric reed sample holder of the AGFM operates at its resonance frequency, which depends on the mass of the sample/substrate combination. For this reason, each new sample requires re-tuning to its resonance frequency. To ensure good quantitative determination of the magnetic moment in the sample it is important to calibrate the sample holder often and ensure that the calibration sample and the measured sample are in the same location within the AGFM set-up, as there is a strong variation in the measured moment with even slight misalignment of the sample. In addition, for samples with small coercivity (<100Oe) it is important to reduce the gradient field by an order of magnitude or more. This modification in gradient field will lead to a similar reduction in the signal-to-noise ratio.

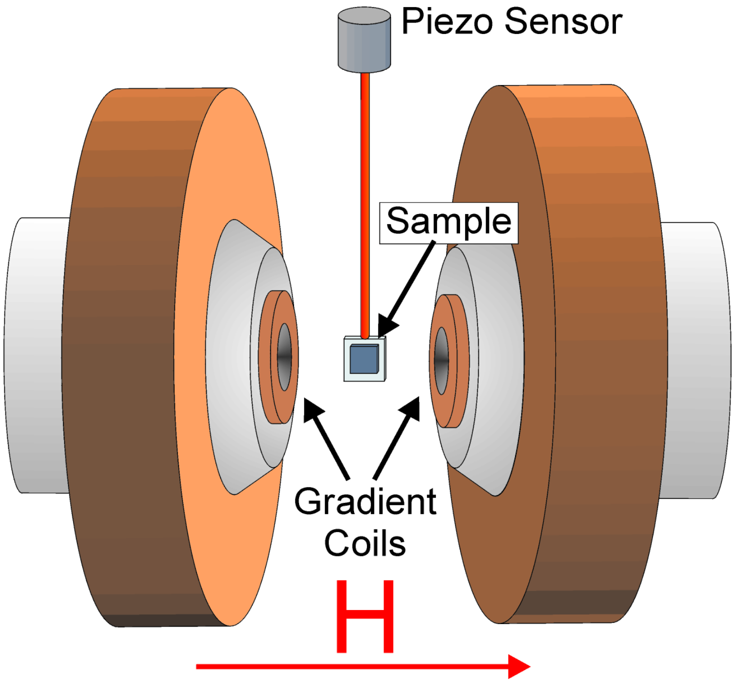

Figure 2.7.1: Alternating Gradient Force Magnetomter

Schematic of the Alternating Gradient Force Magnetometer.

2.8 Neutron Diffraction

Very similar to X-ray spectroscopy techniques (see Chapter 2.3), Neutron diffraction is a crystallographic method for the determination of the atomic and/or magnetic structure of a material. It is well known that neutrons reside in atomic nuclei; to make these neutrons useful for spectroscopy requires a neutron source. There are two predominant types of neutron sources: 1) a nuclear reactor - a device in which nuclear chain reactions are initiated, controlled, and sustained at a steady rate and 2) a spallation source - a process in which a heavy nucleus emits a large number of neutrons as a result of being hit by a high-energy particle. Work for this thesis was done at the High Flux Isotope Reactor (HFIR) at Oak Ridge National Laboratory (ORNL) on beamline HB-1A in collaboration with Dr. Lee Robertson. The 85-megawatt HFIR provides the highest steady-state neutron flux in the USA. The flux at the sample on HB-1A is roughly 2×10^7 n/cm^2/s and for elastic studies on crystallographic and magnetic structures the beamline has a wavevector transfer **Q** range of 0.2 to 4.9 Å^{-1}.

Similar to X-rays, the atomic structure of crystallographic structures can be studied with neutrons. However, because the neutron has a magnetic moment, it also interacts with the magnetization throughout the sample giving magnetic details. For an un-polarized neutron source (which is the case for HFIR), this fact can allow the probing of antiferromagnetic ordering in films. For example, in a (111) textured NiO thin film (See Chapter 1.3), the periodicity of the magnetic structure (the distance between two similarly aligned ferromagnetic planes) is twice that of the atomic periodicity. Thus, in neutron diffraction studies a peak at the (111) position (atomic) will be seen as well as a (½ ½ ½) peak (magnetic), where the (½ ½ ½) peak corresponds to a Bragg spacing that is twice that of (111). Other than this important addition of a magnetic moment, the equations and results seen in Chapter 2.3 for X-rays hold for neutrons, assuming a modified wavelength. Also, the scattering cross section for neutrons is much smaller than that for X-rays, so larger (or thicker) samples are required for reasonable signal-to-noise. For a review see Refs 2.27-2.29.

2.9 References

2.1 J.A. Thornton and D.W. Hoffman, Thin Film Solids **171**, 5 (1989).

2.2 J. Vossen and W. Kern, *Thin Film Processes*, Academic Press, New York (1978).

2.3 B.N. Chapman, *Flow Discharge Processes*, John Wiley and Sons, New York (1980).

2.4 http://www.inficonthinfilmdeposition.com/en/xtm2thinfilmmonitor.html

2.5 Leon I. Maissel, Reinhard Glang, *Handbook of Thin Film Technology*, McGraw-Hill (1970).

2.6 B.D. Cullity and S.R. Stock, *Elements of X-Ray Diffraction: Third Edition*, Prentice Hall, America (2001).

2.7 N.W. Ashcroft, N.D. Mermin, *Solid State Physics*, Holt Rinehart & Winston (1976).

2.8 A. Gibaud and S. Hazra, Current Science **78**, 1467 (2000).

2.9 D.S. Kliger and J.W. Lewis (Author), *Polarized Light in Optics and Spectroscopy*, Academic Press (1990).

2.10 S. Porthun, L. Abelmann, and C. Lodder, J. Magn. Magn. Matter. **182**, 238 (1998).

2.11 P. Grutter, H.J. Mamin, and D. Rugar, *Magnetic Force Microscopy in Scanning Tunneling Microscopy II edited by R. Wiesendanger and H.-J. Gunterodt*, Vol. 28, page 151-207, Spring-Verlag, Berlin (1992).

2.12 R.D. Gomez, *"Recent Advances in Magnetic Force Microscopy: Quantification and in-situ Field Measurements" in Experimental Methods in the Physical Sciences, Vol 36, edited by M. de Graef and Y. Zhu*, Academic Press (2001).

2.13 Retrieved from the world wide web at http://ssrl.slac.stanford.edu/stohr/xmcd.htm

2.14 J. Stöhr, Y. Wu, *New Directions in Research with Third-Generation Soft X-Ray Synchrotron Radiation Sources edited by A.S. Schlachter, F.J. Wuilleumier,* p. 221, Kluwer Academic Publishers, Netherlands (1994).

2.15 J. Stöhr, J. Magn. Magn. Mater. **200**, 470 (1999).

2.16 Paolo Carra, B. T. Thole, Massimo Altarelli, and Xindong Wang, Phys. Rev. Lett. **70**, 694 (1993).

2.17 B. T. Thole, P. Carra, F. Sette, and G. van der Laan, Phys. Rev. Lett. **68**, 1943 (1992).

2.18 B. P. Tonner, G. R. Harp, S. F. Koranda, and J. Zhang, Rev. Sci. Instrum. **63**, 564 (1992).

2.19 J. Stohr, H. A. Padmore, S. Anders, T. Stammler, and M. R. Scheinfein, Surf. Rev. Lett. **5**, 1297 (1998).

2.20 S. Anders, H. A. Padmore, R. M. Duarte, T. Renner, T. Stammler, A. Scholl, M. R. Scheinfein, J. Stöhr, L. Séve, and B. Sinkovic, Rev. Sci. Instrum. **70**, 3973 (1999).

2.21 F. Nolting, A. Scholl, J. Stöhr, J.W. Seo, J. Fompeyrine, H. Siegwart, J.P. Locquet, S. Anders, J. Lüning, E.E. Fullerton, M.F. Toney, M.R. Scheinfein, H.A. Padmore, Nature **405**, 767 (2000).

2.22 R.N. Watts, S. Liang. Z.H. Levine, T.B. Lucatorto, F. Polack, and M.R. Scheinfein, Rev. Sci. Instrum. **68**, 3464 (1997).

2.23 G.F. Rempfer and O. H. Griffith, Ultramicrosc. **27**, 273 (1989).

2.24 G.F. Rempfer, D.M. Desloge, W.P. Skoczylas, and O.H. Griffith, Microsc. Microanal. **3**, 14 (1997).

2.25 R. Fink, M.R. Weiss, E. Umbach, D. Preikszas, H. Rose, R. Spehr, P. Hartel, W. Engel, R. Degenhardt, R. Wichtendahl, H. Kuhlenbeck, W. Erlebach, K. Ihmann, R. Schlogl, H.J. Freund, A.M. Bradshaw, G. Lilienkamp, Th. Schmidt, E. Bauer, and G. Brenner, J. Electron Spectrosc. Relat. Phenom. **84**, 231 (1997).

2.26 R. Nakajima, J. Stöhr, and Y. U. Idzerda, Phys. Rev. B **59**, 6421 (1999).

2.27 George D. Wignall, *Applications of neutron scattering to soft condensed matter*, Gordon and Breach Science Publishers, New York (2000).

2.28 S. W. Lovesey, *Theory of Neutron Scattering from Condensed Matter; Volume 1: Neutron Scattering*, Clarendon Press, Oxford (1984); *S. W. Lovesey, Theory of Neutron Scattering from Condensed Matter; Volume 2: Condensed Matter,* Clarendon Press, Oxford (1984).

2.29 G.L. Squires, *Introduction to the Theory of Thermal Neutron Scattering (2nd ed.),* Dover Publications Inc., Mineola, New York (1996).

Chapter 3

Origin of Interlayer Exchange Coupling in [Co/Pt]/NiO/[Co/Pt] multilayers studied with XAS, XMCD, and micromagnetic modeling

3.1 Introduction

The investigation of the coupling of ferromagnetic films across non-ferromagnetic spacers has resulted in a spectrum of scientific discoveries as well as technologically useful devices [3.1]. Early investigations into the coupling across metallic spacer layers revealed oscillatory coupling [3.2] as a function of spacer thickness and the associated phenomenon of the giant magnetoresistive effect [3.3]. The period of the oscillatory coupling is associated with the spanning vectors of the Fermi surface of the spacer material. For insulating spacers, both theoretical and experimental studies indicate a non-oscillatory monotonic decay of the coupling with increasing spacer thickness [3.4, 3.5].

Our research group had previously observed a non-monotonic oscillatory coupling between two [Co/Pt] multilayers on either side of a NiO spacer layer [3.6, 3.7]. In this novel system, the [Co/Pt] multilayers have a perpendicular easy magnetization axis, while the Ni spins lie in-plane. The period of oscillation corresponds to the antiferromagnetic (AFM) ordering period of the NiO, suggesting a correlation of the coupling with the AFM order. The coupling of ferromagnetic (FM) layers across an AFM spacer has been studied by various groups, often in conjunction with the exchange biasing effect. The well-known oscillatory coupling with a 2 monolayer (ML) period seen for Cr (100) spacer layers [3.8] has been ascribed to a nested feature in the Fermi surface, which also happens to be responsible for the AFM spin density wave. The 2 ML oscillation is not directly attributable to the AFM ordering; in fact, below the Néel temperature of the thin Cr film, the coupling can disappear [3.9, 3.10]. A model of interlayer exchange coupling (IEC) through metallic antiferromagnets (the proximity magnetism model [3.11]) indicates that both the exchange coupling at the interface as well as the propagating spin structure of the AFM spacer has to be taken into account. The spin structure in either the FM and/or the AFM may rotate away from its easy axis at the interface and the anisotropy constants dictate the degree of twisting. In experiments on FM sandwiches coupled across both insulating [3.12, 3.13] and metallic antiferromagnets, [3.14] non collinear coupling has been observed over a substantial range of spacer layer thickness. The presence of atomic layer roughness in the AFM layer leads to a competition between FM coupling between the magnetic layers (favored by an *odd* number of AFM spacer layers) and antiferromagnetic coupling (favored by an *even* number of AFM layers), leading to a compromise that results in a net non-collinear coupling in order to minimize the energy. In these cases, oscillatory coupling as a function of thickness (as would be expected for atomically flat interfaces) is not observed. A recent paper [3.15] using x-ray magnetic circular dichroism photoelectron microscopy (XMCD-PEEM) shows that in a trilayer with a wedge shaped FeMn as the antiferromagnetic spacer layer, the top FM layer shows an oscillatory domain pattern with increasing FeMn thickness. These FeMn layers were carefully prepared to be epitaxial, and showed layer-by-layer growth. The lack of oscillatory coupling in previous experiments may stem from the atomic scale roughness of the surfaces. We do not expect that the sputtered NiO layers in our films are atomically flat; yet the oscillatory coupling is clear and unambiguous and has been reproduced for other samples grown in different sputtering chambers with some variation in the exact parameters [3.6, 3.7]. The perpendicular easy axis of the [Co/Pt] ferromagnetic layer may play a vital role, since the energy cost associated with non-collinear coupling in this configuration is high.

Theoretical calculations [3.16] show that the oscillatory coupling can be explained within a model that assumes the exchange interaction at the NiO/Co interfaces and the antiferromagnetic super-exchange interaction between Ni moments within the NiO film. The canting of the NiO spins that must occur in order for IEC to take place propagates across the thickness of the NiO, leading to either AFM or FM coupling. The following is a study of the canting of NiO spins, the temperature dependence of the coupling and the behavior of magnetic domains in these oscillatory coupled [Co/Pt]/NiO/[Co/Pt] samples. There is clear evidence for canting of the Ni spins. Detailed examinations of the domain structures in virgin samples confirm that the oscillatory coupling occurs domain by domain. Moreover, the Co spins and the Ni spins cant in coincidence, both macroscopically and microscopically. The temperature dependence of the coupling shows both irreversible changes caused by low temperature oxidation/reduction reactions at the interface, as well as reversible changes due to the complex interplay of the temperature dependences of the variety of parameters on which the coupling depends.

The chapter is organized as follows: Sample preparation and experimental measurements are described in section 3.2. Experimental results and discussions involving element specific magnetization of Co and Ni as functions of field as well as x-ray magnetic circular dichroism (XMCD) scans at the Ni photon resonant energy are presented in section 3.3. Section 3.4 presents our results on the domain structure of these multilayers using XMCD-PEEM imaging and MFM. Section 3.5 contains the temperature dependence and a summary and conclusions are presented in section 3.6.

3.2 Sample Preparation and Experimental Techniques

Two series of samples were prepared as outlined below. The series 1 samples were used only for the total fluorescence yield (TFY) measurements. All samples were prepared by dc and rf magnetron sputtering from separate Pt, Co, and NiO targets.

Series 1: Samples on glass substrates with varying NiO thickness and Pt capping layers. Deposition rates were 0.96 Å/s, 0.2 Å/s, and 0.19 Å/s, for Pt, Co, and NiO respectively, in 3 mTorr Ar pressure, with base pressure of 4×10^{-7} Torr.

Glass/Pt(100Å)/$[\mathrm{Pt}(5\text{Å})/\mathrm{Co}(4\text{Å})]_3$/NiO($t_{NiO}$Å)/$[\mathrm{Co}(4\text{Å})/\mathrm{Pt}(5\text{Å})]_3$/Pt(50Å).

t_{NiO} had values 11Å and 12Å

Series 2: Samples on Si substrates with Cu capping layers.

Deposition rates of 0.56 Å/s, 0.26 Å/s, and 0.07 Å/s for Pt, Co, and NiO, respectively, in 2 mTorr Ar pressure with a base pressure of 3.8×10^{-8} Torr.

A. Samples with varying NiO thickness

Si<111>/Pt(100Å)/[Pt(6Å)/Co(4Å)]$_3$/NiO(t_{NiO}Å)/[Co(4Å)/Pt(6Å)]$_3$/Cu(20Å).

t_{NiO} ranged from 7.5Å to 12Å.

B. Samples with varying Pt thickness

Si<111>/Pt(100Å)/[Pt(t_{Pt}Å)/Co(4Å)]$_3$/NiO(8Å)/[Co(4Å)/Pt(t_{Pt}Å)]$_3$/Cu(20Å).

t_{Pt} ranged from 5.1Å – 11.8Å.

The thickness calibration for series 1 was checked by grazing angle X-ray reflectivity after sample preparation, displaying an accuracy of ~10%. Series 2 was checked using an *in situ* quartz thickness monitor. The sample structure was checked for both series by X-ray diffraction. The Pt layers are polycrystalline, but are highly fcc (111) textured; the Co layers are highly hcp (100) textured, and the NiO layer is highly fcc (111) textured.

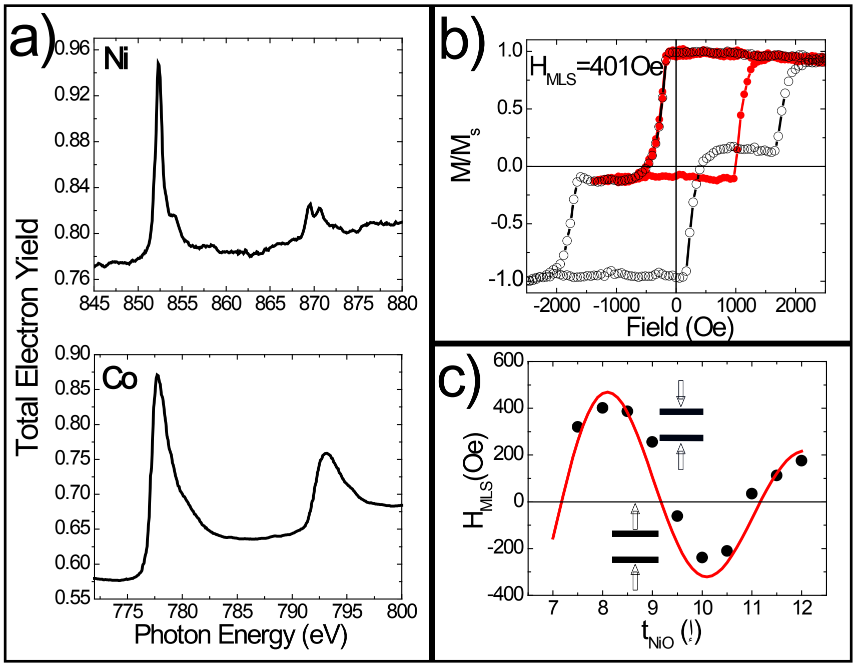

Figure 3.1:

a) Room temperature XAS spectra at the Ni and Co $L_{3,2}$ resonances indicate no evidence of multiplet splitting at the Co $L_{3,2}$ peaks, as would be expected if CoO were present, and the Ni L_2 peak reveals a doublet splitting, as expected for Ni^{2+} in NiO. b) The major and minor hysteresis loops at room temperature for a sample with a NiO thickness of 8Å, which was measured using polar MOKE. For measurement of the minor loop a large field was applied to saturate the sample; the field was then decreased until the top [Co/Pt] multilayer reversed. Then the field was again increased to complete the loop, during this entire loop the bottom [Co/Pt] multilayer does not switch. c) The room temperature minor loop shift is a measure of the interlayer exchange coupling, thus the variation in coupling with NiO thickness is given. The coupling oscillates with NiO thickness from antiferromagnetic to ferromagnetic coupling.

Initial magnetic characterization of samples was done in ambient conditions using a tabletop magneto-optical kerr effect (MOKE) set-up. A typical room temperature MOKE loop is shown in Figure 3.1(b). The upper and lower [Co/Pt] layers have distinct coercive fields, which we attribute to the differences in the microstructure between the two layers [3.17-3.19]. Moreover, the magnetizations of the two layers are unequal; the top multilayer has 1.43 times the out-of-plane magnetization compared to the bottom layer. This ratio of the magnetization has been confirmed by both alternating gradient field magnetometer (AGFM) and superconducting quantum interference device (SQUID) measurements. Careful studies of the absolute magnetization of [Co/Pt] multilayers indicate that increasing Pt strain leads to lower than expected values for the saturation magnetization [3.20]. The intervening NiO spacer layer may change the microstructure of the upper multilayer leading to changes in saturation magnetization, anisotropy and other magnetic properties.

Evidence of oscillatory IEC at RT for a series of NiO thicknesses was obtained by measurement of the minor loop shift similar to that in references 3.6 and 3.7, shown in Figure 3.1(c). The samples in this study represent various regions of antiferromagnetic and ferromagnetic coupling based on these MOKE measurements. Temperature dependent magnetization measurements were made with MOKE using a Janis cryostat with polarization preserving optical windows over a temperature range of 180– 470K.

Element specific characterization was performed using X-ray absorption spectroscopy (XAS) and XMCD at beamline 4-ID-C of the Advanced Photon Source at the Argonne National Laboratory. Due to the large separation of the Ni and Co L_3 resonances (778.1 and 852.7 eV, respectively), XAS provides valuable information on the chemical states of the Ni and Co layers separately (Figure 3.1(a)), while XMCD yields the corresponding magnetization information. The samples were mounted on a liquid He cryostat in a split-coil superconducting magnet with both the field and sample normal parallel to the incident X-ray beam, thus the XMCD data are sensitive only to the normal component of the magnetization. Data was collected in total electron yield (TEY) by monitoring the sample current and in TFY using a Ge detector. One key difference between the two measurements (TEY vs. TFY) is the attenuation lengths of the secondary electrons emitted for the TEY measurements vs. the fluorescence photons (~1-2 nm vs. ~100 nm, respectively). TEY measurements are therefore more heavily weighted by the upper layers and accounting for this attenuation plays an important role in the interpretation of the TEY data obtained.

Element-specific magnetic domain images were obtained using XMCD-PEEM at the same beamline. The XMCD-PEEM provides a map of the absorption contrast with spatial resolution of ~100 nm, thus high-resolution images of surfaces and interfaces with elemental and magnetic contrast can be obtained by tuning to the appropriate incident energy. In this part of the experiment, as-grown (virgin) samples with varying NiO and Pt thicknesses were mounted in the XMCD-PEEM with an incidence angle of 25 degrees above the surface of the sample. In this orientation, the resulting domain images are sensitive to both in-plane and out-of-plane magnetization components. However, both previous [3.7] and current magnetic force microscopy (MFM) domain images shown in section 3.5 clearly indicate that the magnetic domains are oriented perpendicular to the sample plane.

The MFM images were measured in tapping/lift mode at a lift height of 5 nm under ambient conditions. The MFM tip consists of a 30 nm thick CoPt film with a coercivity of ~ 15kOe [3.21] coated onto a soft cantilever. The MFM tip is magnetized along a direction perpendicular to the sample surface, pointing downwards.

3.3 XAS and XMCD Measurements at Co and Ni Resonant Energies

3.3a XAS

In Figure 3.1(a), we show room temperature XAS energy scans with a resolution of 0.25 eV through the Ni and Co $L_{3,2}$ resonances. These scans indicate no evidence of multiplet splitting at the Co $L_{3,2}$ peaks, as would be expected if CoO were present. The Ni L_2 peak reveals a doublet splitting, as expected for Ni^{2+} in NiO. This stands in sharp contrast to previous spectroscopic studies of the Co/NiO interface which indicate a region of CoO and Ni formation in molecular beam epitaxy (MBE) grown interfaces [3.22, 3.23]. We do not see, at similar energy resolution, any formation of a mixed Co-Ni-O compound at the interface region, as evidenced by the lack of multiplet splitting in the Co XAS scan about the L_2 or L_3 edges. Previous measurements of metal-oxide interfaces consisted of MgO/NiO(10Å)/Co(10Å)/Ru, whereas our samples contain considerably more material above the Co/NiO interface, an effect that could lead to considerable attenuation of the secondary electrons. In reference 3.23, the oxidation of Co was limited to about 2Å at the Co/NiO interface. In order to calculate the fraction of the Co signal that arises from this thin layer at the interface we follow the procedure outlined by O'Brien and Tonner [3.24], where the contribution from a single Co layer of thickness dz is

$$dN_{Co} = I_o m_{Co} \mu_{Co} G_{Co} e^{\left(-z\left(\mu_{Co}+\frac{1}{\lambda_{Co}}\right)\right)} dz\,. \tag{3.1}$$

I_o is the incident photon intensity, m_{Co} is the magnetization contribution from the Co layer, μ_{Co} is the photon attenuation through the Co, G_{Co} is the number of created electrons due to the incident photon, and λ_{Co} is the electron attenuation through the Co layer. Integration of dN_{Co} over the thickness of a single Co monolayer gives the TEY contribution from that layer

$$N_{Co} = I_o \frac{m_{Co} G_{Co}}{1+\frac{1}{\mu_{Co}\lambda_{Co}}}\left(1-e^{-t_{Co}\left(\mu_{Co}+\frac{1}{\lambda_{Co}}\right)}\right). \tag{3.2}$$

Due to photon and electron attenuation from the Pt, Cu and NiO layers there will be a different TEY contribution from each of the six Co layers based on the layers that cover it. There are four possible attenuation contributions from the Co, Pt, Cu and NiO layers:

$$\begin{aligned} A &= t_{Co}\left(\mu_{Co}+\frac{1}{\lambda_{Co}}\right) \\ B &= t_{Pt}\left(\mu_{Pt}+\frac{1}{\lambda_{Pt}}\right) \\ C &= t_{Cu}\left(\mu_{Cu}+\frac{1}{\lambda_{Cu}}\right) \\ D &= t_{NiO}\left(\mu_{NiO}+\frac{1}{\lambda_{NiO}}\right) \end{aligned}\,. \tag{3.3}$$

Using these definitions, the Co layers which lie in intimate contact with the NiO will have contributions

$$l_{top} = I_o \frac{m_{Co(top)} G_{Co}}{1+\frac{1}{\mu_{Co}\lambda_{Co}}}\left(1-e^{-A}\right)\left(e^{-4A}\right)\left(e^{-3B}\right)\left(e^{-C}\right) \tag{3.4}$$

and

$$l_{bottom} = I_o \frac{m_{Co(bottom)} G_{Co}}{1 + \frac{1}{\mu_{Co} \lambda_{Co}}} \left(1 - e^{-A}\right)\left(e^{-6A}\right)\left(e^{-3B}\right)\left(e^{-C}\right)\left(e^{-D}\right). \tag{3.5}$$

Doing a similar treatment for the remaining layers of Co allows a ratio of these two sandwiched layers to the rest of the Co to be calculated. For this calculation, we choose λ_{Co} = 25Å [3.25], t_{Co} = 2Å and μ_{Co} = 1/180Å [3.26]. The photon attenuation through Pt and NiO is nearly negligible where μ_{Pt} is 1/620Å and μ_{NiO} is 1/4846Å [3.26]. The electron attenuation through Pt has not been studied, but using the universal energy curve [3.26, 3.27], we assume an attenuation length of 60Å. A secondary electron mean free path of around 4Å is used for the NiO; this will be shown to be experimentally accurate later in this text. With these values, the 2Å layers of Co that are in intimate contact with the NiO make up 13.6% of the total Co contribution in the 8Å sample, where this percentage is highly sensitive to the electron attenuation through the NiO and Pt. Even though the multiplet splitting would occur in only 13.6% of the contributing Co, the expected multiplet features are sufficiently far from the main absorption peak and they would be easily visible. In particular, the absence of pre-edge intensity strongly argues against a significant amount of non-metallic Co. Hence at room temperature and below we assume that there are negligible amounts of CoO at the Co/NiO interface.

3.3b XMCD Hysteresis Loops and Electron Attenuation Length in NiO

In Figure 3.2(a) and (c) we show the element-specific magnetization loops for Co and Ni obtained by tuning to the appropriate L_3 resonance and measuring the field-dependent XMCD in both TEY and TFY modes. In the TEY data, the lower field data is not shown due to artifacts that result from the varying field and photoelectron trajectories. The hysteresis loops were measured for strongly and weakly AFM and FM coupled samples, above and below the blocking temperature; shown are a FM (Figure 3.2(a)) and an AFM (Figure 3.2(c)) coupled sample, taken at 175K and 154K, respectively. The x-ray beam is incident normal to the sample plane; in this geometry, we are sensitive only to the out-of-plane component of the magnetization. The square shapes of all three loops are suggestive of the expected out-of-plane easy axis of the [Co/Pt] (of which we observe the Co). The exchange bias effect is clearly visible as a net shift of the lower temperature loops (shown in Figure 3.2(a) and (c)), an effect which disappears above the blocking temperature of 250K for these samples. Similar effects have been seen with MOKE and SQUID for the $[Pt/Co]_n/NiO/[Co/Pt]_n$ system [3.6, 3.7, 3.28] and show the coexistence of exchange coupling and exchange bias at temperatures below the blocking temperature. A very large difference in the signal from the top and bottom [Co/Pt] multilayers was observed for the TEY data (much larger than that seen in TFY or MOKE data), clearly due to the attenuation of the secondary electrons from the bottom [Co/Pt] layer through the very thin NiO layer and the top [Co/Pt] layer (See study below). MOKE, SQUID and AGFM measurements on a variety of samples give a ratio of 1.43 for the magnetization of the top and bottom [Co/Pt] multilayers. This ratio was observed to be the similar for all samples studied (8, 9.5, 11 and 12Å) over a wide range of temperatures (180K-300K).

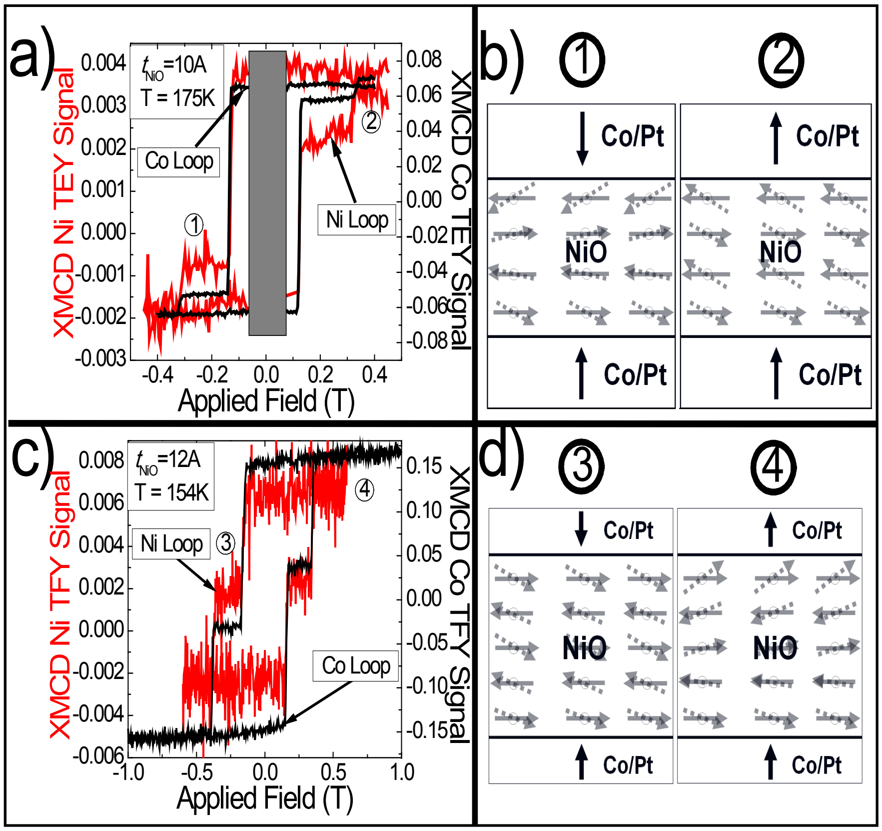

Figure 3.2:

a) Element-specific magnetization loops for Co and Ni taken with X-ray magnetic circular dichroism in total electron yield mode at 175K on a ferromagnetically coupled, series 2 sample with a 10Å thickness of NiO. b) Possible NiO spin configuration for a ferromagnetically coupled sample in the *antiferromagnetic* state (①) and *ferromagnetic* state (②), leading to the net Ni out-of-plane magnetization presented in a) – See section 3.3C in the text for details on exchange coupling at the Co/NiO interface. c) Element-specific magnetization loops for Co and Ni taken with X-ray magnetic circular dichroism in total fluorescence yield mode at 154K on an antiferromagnetically coupled, series 1 sample with a 12Å thickness of NiO. d) Possible NiO spin configuration for an antiferromagnetically coupled sample in the *antiferromagnetic* state (③) and *ferromagnetic* state (④), leading to the net Ni out-of-plane magnetization presented in c).

Both TEY and TFY data indicate that the Ni magnetization, although much smaller than the Co magnetization, as evidenced by the poorer signal-to-noise ratio, follows in lock step with the Co magnetization. We also note (Figure 3.1(a)) that the Ni XMCD line shape in all these samples exhibits a multiplet splitting indicative of a Ni^{2+} state, which shows that this XMCD signal originates in the NiO layer, and not a minority metallic phase. This implies that the Ni spins in the intervening insulating AFM NiO layer cant up and down out of plane in concert with the neighboring Co layers (Figure 3.2(b) and 3.2(d)). In the AFM coupled state (the plateau region at low field, indicated by ① and ③ in Figure 3.2(a) and (c), respectively) the magnitude of the net Ni magnetization is minimized. The resultant magnetization is not zero due to a range of canting angles from the top to bottom of the NiO layer in addition to attenuation effects through the NiO; this canting phenomenon is fully discussed in the next section. In order to study this canting which is predicted [3.16] to play a key role in the coupling, we pose two questions; do both interfacial layers of Ni spins (i.e. the upper and lower) cant an equal amount and how is this canting propagated through the bulk? In order to answer these questions, it is necessary to address the attenuation of the TEY signal through the NiO layer.

For the Co loops, the TEY signal arising from the lower multilayer is considerably smaller than that from the upper one. This is also seen in the Ni loops, where the signal arising from the lower NiO layer is smaller than from the upper layer (each switch at differing coercivities). The dramatic attenuation of the electron signal arising from only ~1 nm of NiO is somewhat surprising. Previous estimates of the attenuation length of NiO range from 2-3 nm [3.23]. However, this attenuation length implies an almost negligible attenuation for our very thin NiO spacer layers, certainly much smaller than the almost 10-fold reduction we see. No published measurements of the electron attenuation length in NiO exist. Therefore, in order to obtain a direct measurement for comparison with our XMCD data, a calibrated wedge-shaped NiO sample with a [Co/Pt] underlayer and a Cu cap was made. Low angle X-ray reflectivity measurements were used to obtain a functional model for the thickness of a NiO wedge grown under identical conditions for a longer time. Figure 3.3 inset shows the position dependent thickness of the thinner NiO wedge used, obtained by scaling down thicknesses with time. The two edges of the wedge were sharply masked to allow for cross calibration of the position. This calibrated sample was loaded into the 4-ID-C beamline at the Advanced Photon Source. The room temperature TEY signal at the Co resonance arising from the lower Co layer was recorded as a function of sample position and correlated with NiO thickness. The integrated Co XAS signal is shown as a function of NiO thickness in Figure 3.3. The resulting exponential fit indicates an attenuation length of 4Å in NiO, much smaller than previous estimates of about 30Å [3.23]. We have made the following assumptions: (i) that the photon absorption in the wedge shaped NiO is negligible, a reasonable assumption since the measurements are made at the Co L_3 resonance, well below the Ni resonance and (ii) that there is a negligible incident photon energy dependence on this attenuation length between the Co and Ni resonances. Although the attenuation length of secondary electrons is energy specific, the TEY consists primarily of secondaries, with a range of energies below ~ 10 eV. The difference in the secondary electron energy distribution and hence the attenuation lengths at the Co and Ni resonance edges (778.1 eV and 852.7 eV respectively) is therefore very small. Thus we use this value of 4Å in the discussion of what follows. A similarly short attenuation length of 4-5Å was measured [3.29] for polarized low energy secondary electrons in NiO, excited by an 800eV electron beam. Assuming that the attenuation is independent of the spin polarization, the result in reference 3.29 provides strong support for our result.

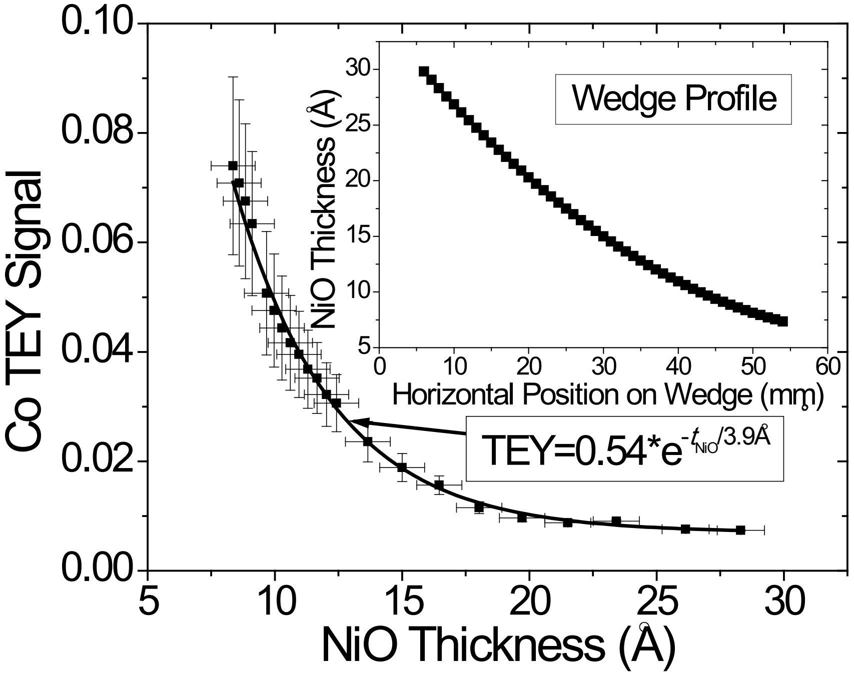

Figure 3.3:

Measurement of the secondary electron attenuation length in NiO. The total electron yield signal arising from the Co L_3 resonance on a $[Co/Pt]_3/NiO/Cu$ sample is measured at room temperature, where the NiO thickness varies with position. The exponential fit indicates an attenuation length for secondary electrons in NiO of 3.9Å. The inset shows the profile of the NiO wedge, characterized with low-angle x-ray reflectivity.

Predictions of the ratio between the top and bottom Co/Pt multilayer TEY signal can be made based on the secondary electron attenuation measurements in NiO. Following from our previous results for the XAS signal from the sandwiching Co layers, we can also use this approach to determine the expected magnetization ratios from the top to bottom [Co/Pt] multilayers. Using previous definitions in Eq. 3.3, the contribution from the top three Co layers is

$$l_{n=1,2,3} = I_o \frac{m_{Co(top)} G_{Co}}{1+\frac{1}{\mu_{Co}\lambda_{Co}}} \left(1-e^{-nA}\right)\left(e^{-(n-1)A}\right)\left(e^{-nB}\right)\left(e^{-nC}\right) \tag{3.6}$$

and the bottom layers is

$$l_{n=4,5,6} = I_o \frac{m_{Co(bottom)} G_{Co}}{1+\frac{1}{\mu_{Co}\lambda_{Co}}} \left(1-e^{-nA}\right)\left(e^{-(n-1)A}\right)\left(e^{-(n-1)B}\right)\left(e^{-nC}\right)\left(e^{-D}\right). \tag{3.7}$$

Thus, the TEY ratio of top to bottom is then

$$Ratio = \frac{m_{Co(top)}\left(l_1+l_2+l_3\right)}{m_{Co(bottom)}\left(l_4+l_5+l_6\right)} = \frac{m_{Co(top)}}{m_{Co(bottom)}} e^{3A} e^{2B} e^{C}. \tag{3.8}$$

As discussed, MOKE measurements on these samples give a ratio of the Co magnetization from top to bottom to be roughly 1.43 for all thickness of NiO over this temperature range. Thus, the TEY ratio is given by

$$Ratio = 1.43 e^{3A} e^{2B} e^{C}, \tag{3.9}$$

With the same values we used previously we obtain the calculated TEY ratios. Comparison of these values to the experimental ratios is given in Table 3.1.

Thickness of NiO (Å)	Calculated TEY Ratio	Experimental TEY Ratio
8	22.7	9.5
10	37.6	14.6
11	48.2	15.3
12	61.9	17.0

Table 3.1:

Comparison of expected and experimental TEY ratios from the upper and lower [Co/Pt] multilayers. For details see text.

A large discrepancy between the calculated and observed TEY ratios is seen. Alternatively, if we assume the experimental TEY ratio is correct, we obtain a λ_{NiO} of nearly 7Å, larger than the 4Å we have measured. This value is still much smaller than previous estimates, but it is significantly different than our anticipated 4Å value. As a similar wedge sample was carefully calibrated using low angle X-ray reflectivity, we expected an error of less than 10%. There are several possible explanations for this discrepancy between the experimental and calculated values. i) Inaccurate absolute thickness calibrations in our Series 2 samples. The sample thicknesses were characterized by *in situ* deposition monitoring, which is less accurate than the X-ray reflectivity and not necessarily consistent over long periods of time following a calibration. ii) Non uniform deposition rates, causing an error in the NiO thickness for the thin wedge-shaped NiO sample on which the experiment was performed. iii) The uncertainties in the other constants, such as the attenuation of the secondary electrons through Co and Pt; varying these parameters will close the gap between the experimental and calculated values. Regardless of these variations, a very short attenuation length is observed for NiO and must be taken into account in this study.

3.3c Ni Canting

We probed the relationship between the canting angles of the Ni moments and the strength of the IEC by measuring the XMCD signal of the Ni layer at normal incidence for a range of samples with varying coupling strengths. The normal incidence XMCD scans were performed about the L_3 edge of Ni, at 852.7 eV (Figure 3.4). All measurements were made at high enough fields such that the Co magnetization was saturated i.e. the [Co/Pt] layers were in a *ferromagnetic* state (Figure 3.2, points ② and ④) and were taken at 175K. Based on the model proposed by Zhuravlev *et al.* [3.16] we expect the Ni moments within the NiO structure to cant out of the (111) plane with the resultant canting angle arising from the competition between the coupling across the two Co/NiO interfaces, the AFM exchange in NiO and the out-of-plane K_1 anisotropy constant of the NiO. The antiferromagnetic order in NiO (111) consists of spins oriented along the three $<11\bar{2}>$ directions, which lie in the (111) plane [3.30]. The ferromagnetic (111) sheets stack antiferromagnetically in the <111> direction. Due to the lack of in-plane anisotropy, all possible spin orientations exist within the plane. The exchange interaction with the adjacent Co causes a canting of the spins, forming a cone of constant half-angle θ and the NiO XMCD signal is proportional to $\cos(\theta)$. The integrated XMCD (IXMCD) signal shown in the Figure 3.4 inset is a measure of the net out-of-plane signal from these Ni spins and is found by integration over the dichroism signal normalized to the total XAS signal.

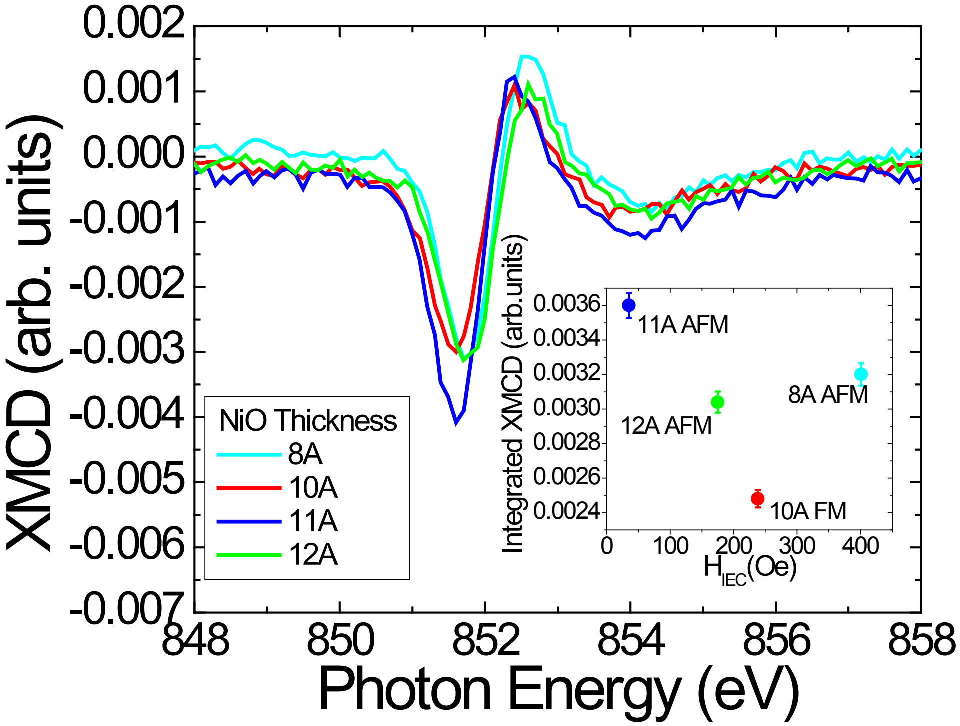

Figure 3.4:

XMCD signal at the Ni L_3 resonance for the 8, 10, 11 and 12Å samples, taken at 175K. The integral over this signal gives a measure of the net out-of-plane magnetization in the antiferromagnetic NiO. Inset: The magnitude of the integral over the dichroism signal versus the magnitude of the coupling strength for the given sample. A larger out-of-plane signal arises for the AFM coupled samples when compared to the FM coupled sample.

One complication arising from the short attenuation length of secondary electrons in NiO is that the signal in Figure 3.4 is heavily weighted in favor of the upper NiO layers. Even for the thinnest NiO sample (8Å) the lower NiO interface contributes only about 10% to the total signal. This IXMCD signal is then weighted by the attenuation effects from the NiO layer. For example, the bottom layer for the 12Å sample will contribute less to the total Ni magnetization than it will for the 8Å sample. It should be noted that these XMCD measurements alone do not reveal the actual layer-by-layer configuration of the spins, but are able to measure the overall canting contribution to the out-of-plane magnetization. Figure 3.4 shows the measure of this out-of-plane contribution as a function of the magnitude of the coupling strength. The data show that the AFM coupled samples have a larger out-of-plane net Ni signal than that of the FM coupled samples.

In order to explain the experimental data, we use a model proposed by Zhuravlev *et al*. [3.16] who attributed the IEC to the exchange interaction at both Co/NiO interfaces and the antiferromagnetic super-exchange interaction within the NiO film. In that work, the coupling at both the top and the bottom Co/NiO interfaces was assumed to be FM and of the same magnitude. It was found that AFM (FM) IEC occurred for an even (odd) number of NiO MLs, hence leading to the experimentally observed oscillatory coupling. In the saturated state where both [Co/Pt] layers are aligned parallel (Figure 3.2, points ② and ④), such a consideration leads to a large out-of-plane signal for FM coupled samples, with one uncompensated layer, and a much smaller signal for AFM coupled samples. If, however, the interfacial exchange coupling has opposite signs at the top and bottom interfaces the model predicts the opposite case, namely, that an odd (even) number of

NiO MLs leads to AFM (FM) IEC. Based on the conclusions of Figure 3.4, namely that the AFM coupled samples have a larger out-of-plane signal than the FM coupled samples, we believe this is the case for our work.

If the couplings at the top and bottom interfaces have differing magnitudes (as well as signs) the Ni spins near the stronger coupled interface will have a larger canting angle leading to an asymmetric spin configuration across the NiO. This asymmetry in the NiO canting is figuratively shown in Figure 3.2(b) and 3.2(d), where the net Ni magnetization found in the hysteresis loops in Figure 3.2(a) and 3.2(c) is due to this asymmetry. From hysteresis loops taken below the blocking temperature we find that the exchange bias field acting on the top [Co/Pt] multilayer is approximately twice that for the bottom film, so a similar consideration was taken for the interfacial exchange coupling. Also, since the net Ni magnetization is aligned parallel to the [Co/Pt] magnetization (since the XMCD hysteresis loops for Co and Ni match in Figure 3.2(a) and 3.2(c)) we deduce that the stronger interface coupling at the top is FM in nature, as we are most sensitive to the topmost layer due to attenuation. These considerations explain the data found in Figure 3.4.

A possible mechanism for the different exchange coupling at the two interfaces could be that the termination of NiO at the two interfaces is different; for example, Nickel terminated interface at the top and Oxygen terminated at the bottom. The direct Ni-Co exchange interaction at the top would most likely lead to FM coupling. At the bottom interface, however, coupling between Ni and Co spins would be mediated by the super-exchange interaction through the O terminated interface and would lead to an AFM coupling, as it does in NiO itself. Since the two couplings have different physical origins it is reasonable to assume that the two will have different magnitudes, as is reflected in the different exchange bias for the top and bottom [Co/Pt] multilayers. The results of Figure 3.4 should be regarded as indirect evidence for this mechanism, and further experimental investigations are needed to confirm our assumptions.

3.4. Domain Structures using XMCD-PEEM and MFM

All domain imaging was performed on virgin samples, in zero applied field and at room temperature. Both XMCD-PEEM and MFM were used, providing complimentary data.

3.4a Coincidence of domains in NiO and Co: XMCD-PEEM measurements

Magnetic domain images were taken using XMCD-PEEM on a virgin, as-grown sample, with t_{NiO}= 8Å, corresponding to the strongest AFM coupling in the series 2 sample set. In Figure 3.5 we show images of the difference obtained for right and left circularly polarized X-rays taken at the (a) Co and (b) Ni L_3 edges. In these perpendicularly oriented films, the contrast in the XMCD-PEEM images corresponds to up (light) and down (dark) domains. Due to the strong attenuation of secondary electrons originating from the bottom [Co/Pt] layer, we primarily see the contribution from the top [Co/Pt] multilayer. The image taken at the Ni resonance, shown in Figure 3.5(b) shows an identical domain configuration, with a very weak contrast. We emphasize that these images are XMCD images hence the domains seen in NiO correspond to a net magnetization of the NiO perpendicular to the film plane (as discussed earlier, all possible spin orientations exist within the plane), and not antiferromagnetic domains as would be seen by magnetic linear dichroism. The domain images are exactly coincident: arrows indicate the location of strikingly similar features. The domain-by-domain correspondence implies that the Ni spins cant in coincidence with the Co magnetization at a microscopic level, and rules out a minority ferromagnetic Ni phase as the explanation for the Ni moment seen by XMCD. Hence the Ni and Co spins follow in lock step throughout the sample on both a macroscopic (as seen with element specific magnetization curves) and a microscopic level.

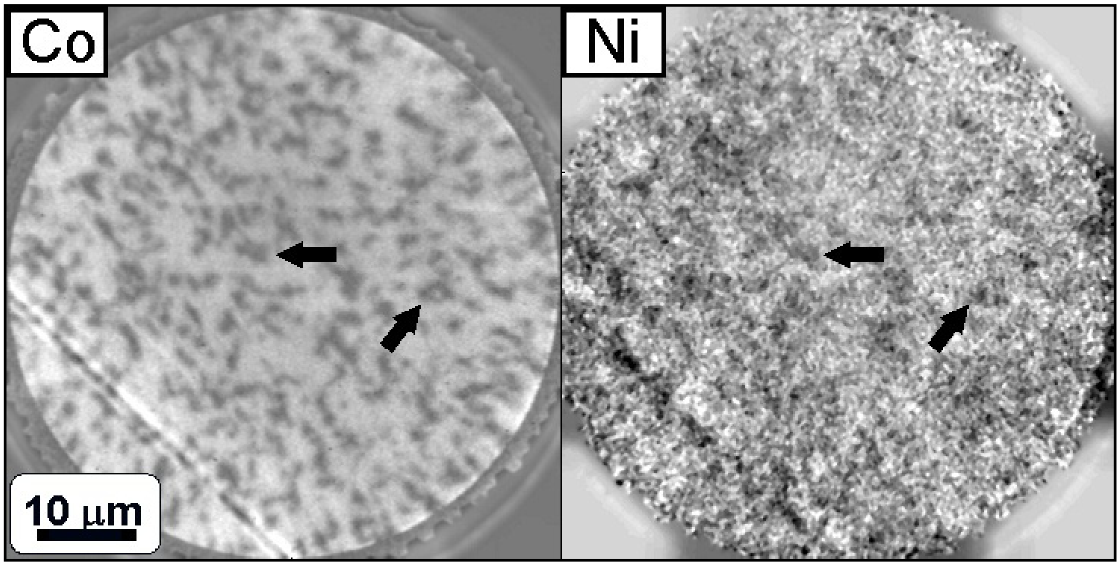

Figure 3.5:

X-ray magnetic circular dichroism – photoemission electron microscopy images taken at room temperature at the Co and Ni L_3 resonances on a virgin, antiferromagnetically coupled, 8Å sample from series 2. This technique images ferromagnetic domains in both the top Co and buried NiO layers. There is exact coincidence in the domain structure of the Co and NiO. Arrows indicate the position of coincident domains.

3.4b Variation in domain size with coupling strength: XMCD PEEM images at Co L_3 edge

XMCD-PEEM images were taken at the Co L_3 resonance for a variety of series 2 samples with varying coupling strength, and are shown in Figure 3.6. Previous measurements [3.7] indicate a variation in coupling strength as the Pt thickness was varied. To generalize our result we account for changes in IEC due to both Pt and NiO thickness variations and investigate the domain size as a function of coupling strength. Once again, only the contribution from the top [Co/Pt] multilayer is visible due to attenuation. The domain images indicate that the weaker coupled samples form very small domains that surround the larger domains that form for all samples. These smaller domains developed as 'wispy' domains in the 11Å and small 'speckle' domains in the 9.5Å, which represent the weakest coupling. Using ImageJ, a public domain Java image processing program inspired by NIH Image for the Macintosh [3.31], the average domain size was determined for each sample. ImageJ was designed with an open architecture that provides extensibility via Java plug-ins. Using one such Java plug-in, we were able to determine the average size of each domain. This particular plug-in allows the user to define a boundary (domain edge) and then mask all possible domains. The areas of these masks are separated into 256 bins and are then plotted as a histogram. From this histogram an average size can be determined. A direct correlation between the magnitude of the coupling strength and domain size was established, where the error bars give a measure of the spread in domain size (Figure 3.6). Note that this effect is independent of both the sign of the coupling (whether FM or AFM) and the method used to vary the coupling strength (i.e. changing either the NiO or Pt thickness). The non-monotonic dependence on the thickness of the intervening NiO layer provides a strong argument against purely magnetostatic effects. Clearly, the strength of the interlayer coupling plays a major role in determining the domain size in these coupled samples.

Qualitatively, we may consider the IEC as playing the role of an effective anisotropy. Then, a decrease in the coupling lowers the energy cost for domain formation leading to the formation of smaller domains for the weakly coupled samples to minimize the magnetostatic self-energy.

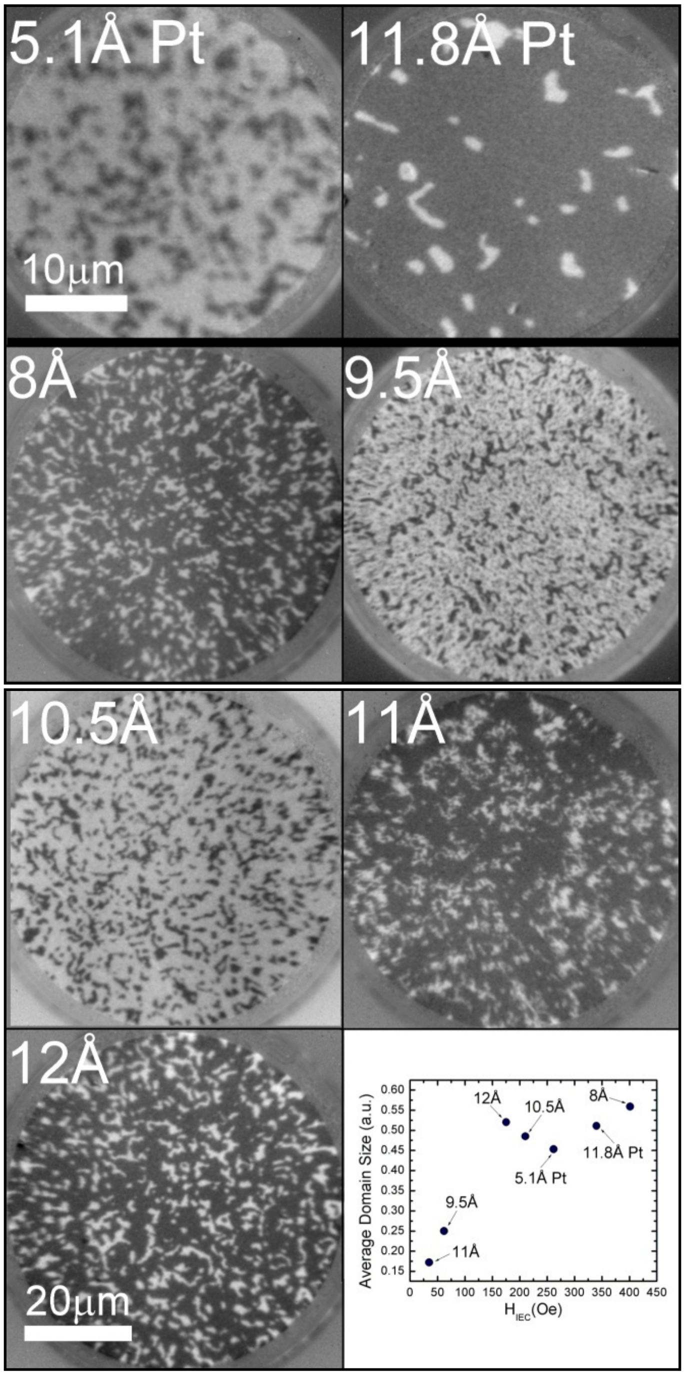

Figure 3.6:

XMCD-PEEM images taken at room temperature at the Co L_3 resonance on virgin samples representing various NiO and Pt thicknesses. Due to attenuation, this measurement is only sensitive to the top Co layers. The top two images represent two Pt thicknesses (5.1 and 11.8Å), where the NiO thickness was set to 8Å. The lower 5 images represent varying NiO thicknesses (8, 9.5, 10.5, 11 and 12Å). The plot shows the average domain size of these samples as a function of their coupling strength. The average domain size tends to increase with increasing coupling strength, no matter how this variation in coupling is attained (varying NiO or Pt thickness).

3.4c MFM images of varying NiO thickness

MFM images, in contrast to the XMCD-PEEM images above, see both the upper and lower [Co/Pt] multilayers. In Figure 3.7 the light-colored areas correspond to a magnetization pointing up. For AFM coupled samples, the only contrast appears in the domain wall regions, as can be seen in Figure 3.7(a) and (d), since the [Co/Pt] layers order antiferromagnetically domain-by domain [3.7]. For FM coupled samples (Figure 3.7(b)), clear up and down domains are visible. An intriguing feature appears within the domain wall of AFM coupled samples: small FM domains are formed within the domain wall by a slight relative shift of the domains in the upper and lower multilayer. This is most clearly visible in the 12Å NiO sample. Similar effects have been seen in an AFM coupled sample of [Co/Pt] separated by Ru [3.32]. The weaker AFM coupling in the 12Å sample (as compared to the 8Å sample) makes domain overlap energetically favorable in order to reduce the magnetostatic energy at the expense of the IEC. Also clearly visible in Figure 3.7(d) are "stripes" in the FM domain overlap region corresponding to opposite net magnetizations in the domain wall. The dipolar energy within the domain wall region is reduced by having the orientation of the FM region reverse periodically along this overlap of the upper and lower domains. This process leads to the formation of both up and down FM domains that form periodically throughout this overlap. The region of overlap of the upper and lower domain structure increases dramatically for the weakest AFM coupled sample (11Å), due to a significant decrease in AFM exchange energy. In this sample, with very weak interlayer exchange energy, magnetostatic effects play a large role, leading to domain overlaps that are a significant fraction of the domain size.

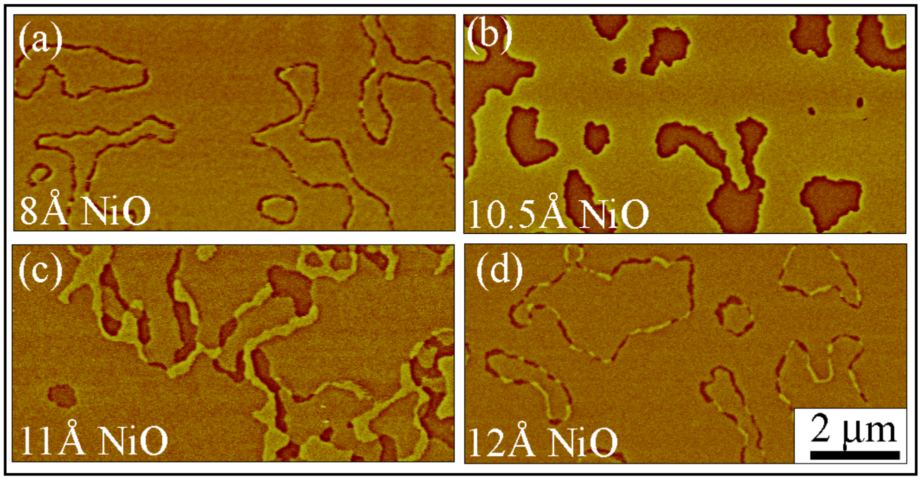

Figure 3.7:

Room temperature MFM images of samples with 8, 10.5, 11 and 12Å NiO thicknesses. The 8 and 12Å samples are antiferromagnetically coupled, up and down domains disappear and only a domain overlap region is observed. The 10.5Å sample is ferromagnetically coupled and only up and down domains are observed. The 11Å is very weakly coupled (slightly antiferromagnetic). The domain overlap that occurs in the antiferromagnetically coupled samples grows with decreasing coupling strength, where the 8Å is the strongest and 12Å is the most weakly coupled sample. The orientation flips from up to down along the overlap to minimize magnetostatic energy.

To model this behavior, we developed a simple model of two identical magnetic layers of thickness *t* separated by distance *d*, as shown in Figure 3.8. The magnetization in each layer is a periodic system of stripe domains with magnetization directed perpendicularly to the plane. There are two domains of equal size within one period *L*. The magnetization changes abruptly by 180° from one stripe domain to the next, i.e. the variation of the magnetization within the domain wall is neglected. We assume that the domain patterns in the two layers are displaced with respect to each other by *δ*. The magnetostatic energy is calculated using the method described in references 3.33 and 3.34.

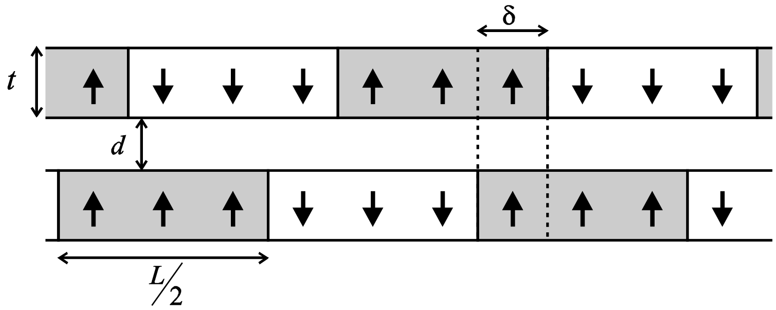

Figure 3.8:

The model domain structure for the two [Co/Pt] multilayers. The view is in the plane of the film along the stripe domains. The dimensions are defined in the text.

Here we consider only the AFM IEC, since in FM coupled samples the FM configuration corresponds to a minimization of both the exchange coupling and the dipolar energy (since the magnetization of the two films is constrained to remain perpendicular to the film plane). In the calculations we assume a $[\mathrm{Co/Pt}]_3$ thickness of $t = 3$nm, the thickness of NiO $d = 1$ nm and the stripe width $L = 3.22$ μm corresponding to the equilibrium domain size according to XMCD-PEEM measurements. The energy of the IEC through the spacer is given by $E_{IEC} = 4J_{IEC}\delta/Lt$, where J_{IEC} is the coupling constant.

The total energy as a function of δ for an AFM exchange coupling $J_{\mathrm{IEC}} = 0.1$, 0.033 and 0.015 erg/cm^2 is displayed in the Figure 3.9 inset, where the latter two values correspond to the 8 and 12Å samples, respectively. There is a small but nonzero value of δ for which the energy is minimal, so the magnetizations of the two layers are mostly antiparallel except for a small overlapping region as observed in Figure 3.7. This overlap arises due to the competition between the magnetostatic interaction and the IEC: the magnetostatic interaction favors parallel alignment whereas the exchange interaction prefers antiparallel alignment of the domains. On average, the IEC dominates the magnetostatic interaction and if the two were homogeneous over the surface the domains would align perfectly antiparallel with no overlap. However, the magnetostatic coupling is strongly inhomogeneous over the surface due to the stray fields localized in the vicinity of the domain walls. That makes it energetically favorable to produce a small shift δ between the antiparallel aligned domains to reduce the magnetostatic energy [3.32]. With increasing the IEC constant the value of δ decreases with J_{IEC}, as is seen from the results of calculation shown in Figure 3.9 by solid circles.

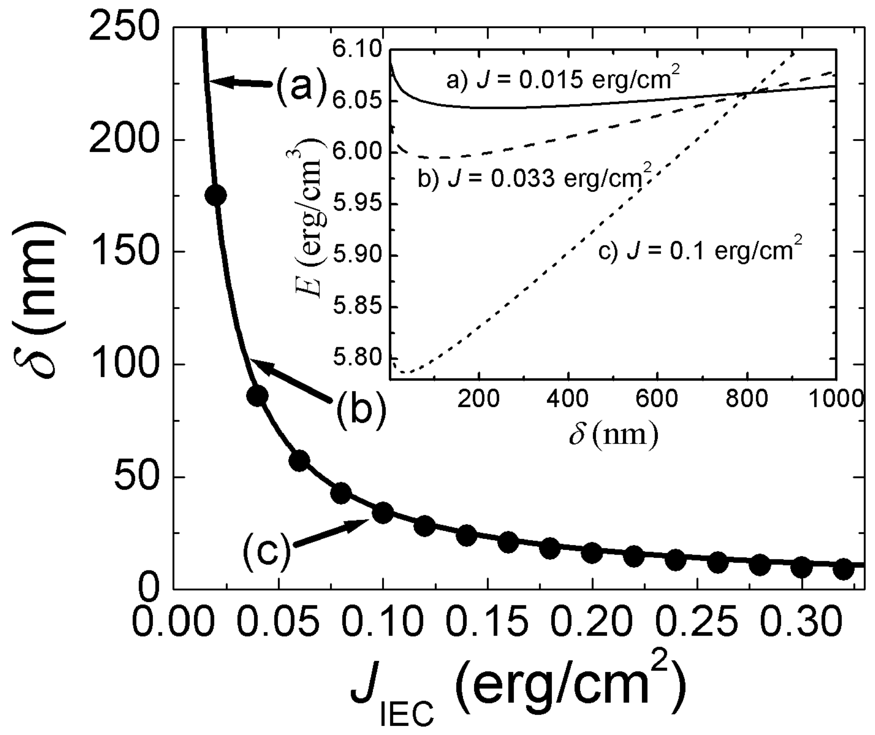

Figure 3.9:

The dependence of the equilibrium domain overlap δ on the interlayer exchange coupling J_{IEC}. The open circles are results of the numerical calculation for periodic stripe domains, and the curve calculated directly from Eq. 3.11. Arrows indicate specific values for J_{IEC} as defined in the inset. The closed circles show the measured δ values for the 12 and 8Å samples, as defined in the text. Inset: The variation in the total energy versus the overlap δ for 3 J_{IEC} values (a) 0.015, (b) 0.033 and (c) 0.1 erg/cm^2, where (a) and (b) correspond to the coupling for the 12 and 8Å samples, respectively.

It can be shown from a simple analytic calculation that the variation of δ is inversely proportional to J_{IEC}. In the limit of large L the perpendicular component of the field produced by the lower Co/Pt multilayer with a domain wall at $x = 0$ can be written as

$$H_z\left(x,z\right)=4M\left[\arctan\left(\frac{z+t}{x}\right)-\arctan\left(\frac{z}{x}\right)\right], \tag{3.10}$$

where z is the distance above the film. This field acts on the upper Co/Pt multilayer with a domain wall at $x = \delta$. For $\delta << d$, as appears to be the case in Figure 3.7, the magnetostatic energy of the interaction of these two domain walls is proportional to $\ln(1/\delta)$ and the competition with the interlayer exchange interaction leads to a finite overlap given by

$$\delta=\frac{8M^2t^2}{J_{\text{IEC}}}. \tag{3.11}$$

The variation of δ calculated using Eq. 3.11 is plotted in Figure 3.9 by the solid line showing an excellent agreement with the results of the numerical calculations for the periodic system of stripe domains.

Now we compare the results of the domain width calculations to the experimental results. For the weakly coupled sample (with 12Å of NiO) the strength of the IEC is 0.015 erg/cm^2 (Eq. 3.11) yields a domain wall width of 235nm. For the stronger coupled 8Å sample, corresponding to an interlayer coupling strength of 0.033 erg/cm^2, (Eq. 3.11) calculations give a domain wall overlap of 107nm. From line scans on the MFM data the width of the overlap, for the 8Å and 12Å samples, are 130nm and 240nm, respectively. The excellent quantitative agreement between the calculated and observed domain wall overlap is strong evidence for the model of competing interactions.

3.5 Temperature Dependence and Oxidation/Reduction Reactions at the Interface

The temperature dependence of the IEC consists of an irreversible component arising from chemical changes at the Co/NiO interface and reversible changes arising from a combination of temperature dependences of the magnetic ordering and the anisotropy.

3.5a Temperature induced irreversibility

Heating these samples above room temperature produces a small, permanent decrease in the room temperature minor loop shift (MLS). Figure 3.10(a) indicates the size of this effect. The data in Figure 3.10(a) was taken by increasing the sample temperature (inside an evacuated cryostat) to the value specified on the x-axis. The sample was then allowed to cool in the absence of an external field to room temperature and the MLS was measured. For the strongest AFM coupled sample, with a NiO thickness of 8Å, the change amounted to 120 Oe after heating the sample to a maximum value of 450K (Figure 3.10(a)).

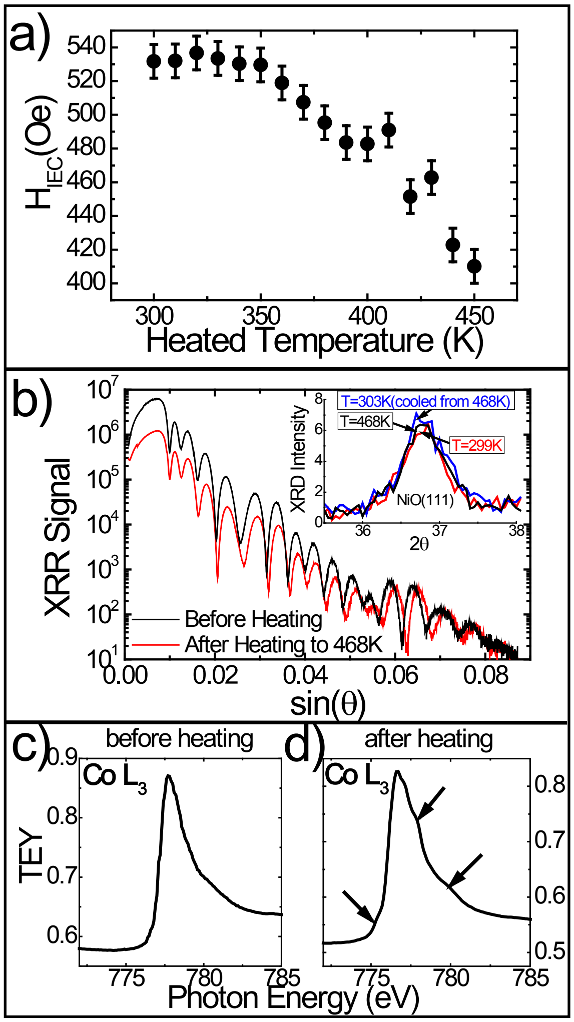

Figure 3.10:

a) A plot of the room temperature minor loop shift after heating to a specified temperature, indicated on the horizontal axis. This indicates permanent, irreversible changes in the exchange coupling due to heating, where these changes increase with increased heating. b) Low-angle x-ray reflectivity taken on an 8Å sample from series 2 before and after a 468K heating showing minimal change in the multilayer structure due to diffusion and no evidence of increased roughness. The inset of b) shows no change in the intensity of the x-ray diffraction at the NiO fcc(111) peak before, at and after a 468K heating. c) XAS data taken at the Co L_3 resonance before (c) and after (d) heating to 468K. The presence of CoO after heating is evident in (d).

In order to check for structural changes in the sample with this low temperature anneal, x-ray reflectivity (XRR), diffraction (XRD) and absorption (XAS) were performed. XRD measurements were performed at the NiO(111) diffraction peak and show that the decrease in the MLS is not due to a structural change in the NiO as there is very little change in either the intensity or the shape of the (111) peak as a function of temperature (Figure 3.10(b) inset). XRR was carried out before and after a 468K anneal and shows little evidence of a change in the multilayer structure by way of diffusion as there is no decrease in the intensity of the multilayer Bragg peaks and no increase in roughness (Figure 3.10(b)). There is a small change in the Bragg peak position of .12° in 2θ, indicating a slight change (0.45Å) in the thickness of the [Co/Pt] multilayers. Previous measurements indicate that annealing even at low temperatures dramatically increases the degree of oxidation/reduction at the interface [3.23]. Figure 3.10(c) shows room temperature XAS measurements at the Co L_3 resonance performed before and after (Figure 3.10(d)) heating the sample to 450 K. A comparison shows clear evidence of the formation of small amounts of CoO after annealing. This oxidation/reduction reaction occurs at the Co/NiO interface and is responsible for the reduction in the IEC. This result has implications for spin valve structures based on transition metal oxides-even a very small temperature increase from 300K to 400K results in an irreversible 40 Oe decrease in the coupling strength. Our data indicate that in addition to roughness and structural inhomogeneities [3.35], the details of chemical processes at the interface can be quantitatively correlated with the strength of the magnetic coupling [3.22].

3.5b Temperature dependence of the minor loop shift

The temperature dependence of the IEC across a spacer layers provides insight into the combination of parameters that govern the coupling. Temperature dependences arise from a combination of spacer layer effects, magnetic layer effects and the temperature dependence of the reflection coefficients at the interface. Theoretical treatments of the temperature dependence taking into account some combination of these effects predict different dependences for metallic and insulating spacer materials [3.36-3.39]. For metallic spacer layers, the smearing of the Fermi surface leads to a reduction in the IEC coupling strength with increasing temperature [3.40, 3.41], whereas in an insulating spacer [3.39] the greater availability of carriers with increasing temperature leads to an increase in the strength of the coupling, an effect seen in SiO_2 spacer layers [3.42] and recently in NiO below 350K [3.6, 3.28]. The magnetic layer effects are due to magnetic excitations, altering the properties of the magnetic layers. Thermal magnetic disorder may drastically reduce the energy difference between parallel and antiparallel alignment of the magnetic layers and therewith the interlayer coupling [3.43].

The effects of temperature on the [Co/Pt]/NiO/[Co/Pt] system are complex and include the temperature dependences of magnetic ordering in both the ferromagnetic [Co/Pt] and the antiferromagnetic NiO, the anisotropy constants and the availability of carriers in the insulating NiO. The data on the temperature dependence of the coupling are shown in Figure 3.11. Minor loops were taken *in situ* on samples with a variety of

NiO thicknesses in a temperature range of 180 to 470K using MOKE. We confine our discussion to temperatures above the blocking temperature of 250K and to AFM coupled samples, since minor loops for the FM coupled samples are harder to ascertain at high temperatures, leading to larger errors in the strength of the IEC. For the strongest AFM coupled samples (t_{NiO}=8 and 12Å), the minor loop shift (and thus the coupling) increases slightly and then decreases with temperature. The decrease for the 8Å sample corresponds to a change of 250 Oe in going from 300K to 470K and is significantly larger than the irreversible changes previously discussed (Note that all measurements reported here are made on previously unheated samples). Even at the highest temperature of 470K, the minor loop shift (and hence the IEC) is still present and fairly large. This is consistent with Reference 3.28, which indicates that the coupling disappears above 500K for 11Å of NiO.

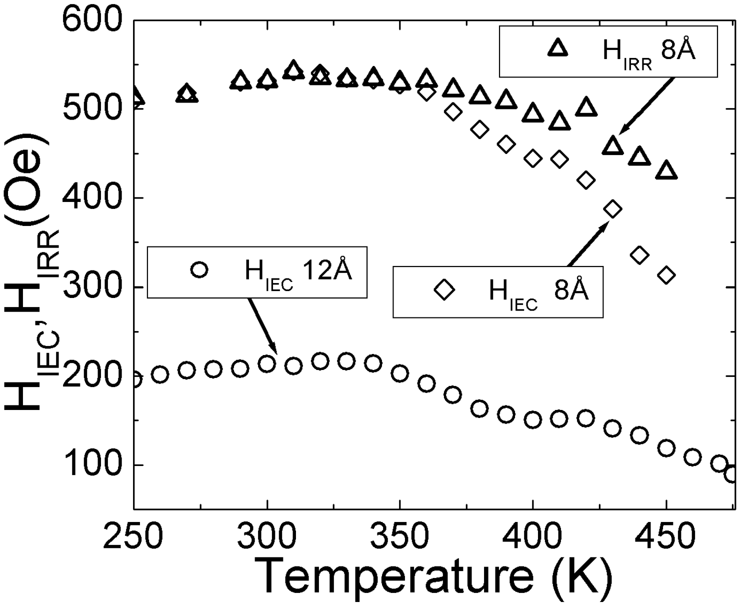

Figure 3.11:

Interlayer exchange coupling as a function of temperature for the 8 and 12Å samples, which couple antiferromagnetically. Two plots are given for the 8Å sample. The H_{REV} data are the reversible component of the temperature dependence, obtained as explain in the text. The 8 and 12Å samples exhibit a decrease in interlayer exchange coupling with increasing temperature.

In an attempt to separate the changes in coupling caused by irreversible chemical reactions at the interface from the purely reversible temperature dependence, we have plotted in Figure 3.11 the temperature dependence of the IEC coupling for the 8Å NiO sample (with the strongest AFM coupling) after accounting for the irreversible changes. Below 300K, ΔH_{IRR}, the irreversible change in exchange coupling caused by heating the sample, is 0. Above 300K, we set

$$\Delta H_{REV}(T) = \Delta H_{IEC}(T) - \Delta H_{IRR}(T) \tag{12}$$

where $\Delta H_{REV}(T)$ is the change in coupling due to reversible temperature dependent changes (shown in Figure 3.11) and $\Delta H_{IEC}(T)$ is the total change measured. There is a slow increase in this purely reversible component of the interlayer coupling from 250K-300K followed by a plateau and then a decrease. However, even at the highest temperature of 450K, the interlayer coupling is large.

Since the AFM ordering of the NiO plays a crucial role in the coupling, we expect the coupling to vanish above the Néel temperature of the NiO. The Néel temperature of a very thin antiferromagnetic film in a FM/AFM/FM trilayer is hard to ascertain experimentally and hence we point to previous experiments. Previous measurements on epitaxial thin films of NiO indicate Néel temperatures of ~300K for a 5 ML sample [3.44], a dramatic reduction from the bulk. The presence of a large IEC at temperatures well above this may be explained by the presence of the ferromagnetic [Co/Pt], which could stabilize the AFM ordering. Such effects have been seen before. Neutron scattering studies on both Fe_3O_4/NiO [3.45] and Fe_3O_4/CoO superlattices [3.46] show that the ferrimagnetic ordering of the Fe_3O_4 stabilizes the AFM ordering of the antiferromagnet, leading to Néel temperatures well over the bulk Néel temperature. Hence, it is entirely feasible that the Néel temperature of the NiO in our multilayer sample is enhanced, certainly above the thin film value of 300K and perhaps even above the bulk value of 525K. In fact, in many magnetic superlattices, only a single transition temperature (the Curie and/or the Néel temperature) exists for the entire structure [3.46, 3.47].

The Curie temperature of the [Co/Pt] multilayers varies with both Co and Pt thickness, increasing with Co thickness [3.48] and decreasing with Pt thickness [3.49]. In samples with thicknesses comparable to ours, the Curie temperature is above 700K [3.47]. Recent measurements on similar multilayers indicate that the IEC goes to zero at 526K [3.28], a temperature which is a reasonable candidate for the single transition temperature of the stack. One concern is the effect of the oxidation/reduction reaction at these higher temperatures, an issue that has not been addressed in Reference 3.28 and which could conceivably lead to an artificially lowered temperature value for the disappearance of the IEC.

The slight increase in the strength of the IEC over the temperature range 250K - 350K may be attributed to a steep decrease in the out-of-plane K_1 anisotropy constant with increasing temperature, assuming that the temperature dependence of K_1 is similar to that measured for K_2 [3.50]. The IEC, which is driven by the Co/NiO interface coupling and mediated through the NiO, depends on both the AFM exchange of the NiO (which tends to align successive spin layers antiparallel) and the anisotropy constant of the NiO (which tends to align the spins in the in-plane (111) direction, minimizing the canting). In this temperature regime, the anisotropy constant decays rapidly, much faster than the AFM order parameter, leading to a situation whereby the spins order almost strictly anti-parallel to each other, with no frustration at either interface, hence maximizing the coupling. At higher temperatures, the decrease in the antiferromagnetic order parameter reduces the ability of the antiferromagnetic spacer to mediate the coupling, leading to the decrease that is seen.

Our data provide strong evidence for a Néel temperature that is significantly enhanced above the thin film value. In addition, the complex interplay between the various parameters is evidenced in the non-monotonic temperature dependence.

3.6 Conclusions

The element specific magnetic behavior measured by XMCD reveals that the in-plane Ni spins in the antiferromagnetic NiO cant out-of-plane and track the out-of-plane [Co/Pt] magnetization in these oscillatory coupled [Co/Pt]/NiO/[Co/Pt] magnetic heterostructures. XMCD hysteresis loops indicate that the Ni magnetization follows the [Co/Pt] magnetization as a function of field. On a microscopic level using XMCD-PEEM imaging, we have shown that the domains in Co and NiO are exactly coincident, indicating that the tracking of spins occurs domain-by-domain and is not the result of averaging effects. This tracking of spins provides strong support for the model of Zhuravlev *et al*. [3.16] in which the oscillatory coupling across the NiO spacer layer is simply a result of exchange coupling at the Co/NiO interface and the antiferromagnetic coupling in the NiO layer. In order for this exchange coupling to occur, it is necessary for the Ni spins to cant out-of-plane.

However, a simple relationship between the degree of canting and the strength of the IEC has not been seen. Experimentally, the net Ni out-of-plane magnetization is larger for AFM coupled samples and there is a non-monotonic dependence of this magnetization on the strength of the coupling. There is strong experimental evidence that the coupling at the upper and lower interface differ both in magnitude and sign. We infer that, in common with nearly all magnetic exchange coupling, the microscopic details of the interface structure drive the macroscopic behavior. In this case, we have indirect evidence for differing signs of the coupling at the two interfaces, which may imply different termination layers. Clearly careful structural work is needed in order to see if this is indeed the case.

An unexpected result arising from our work is the extremely short attenuation length for secondary electrons in NiO, ~4-7 Å. This has implications for the interpretation of earlier XMCD work [3.23], since previous fitting of spectroscopic data assumed a much longer attenuation length based on the universal energy curve. It is possible that other transition metals oxides have similarly short attenuation lengths, quite far removed from the universal energy curve.

Domain imaging using XMCD-PEEM at the Co resonance (which sees only the upper [Co/Pt] layer due to strong attenuation effects) indicates an increase in the average domain size with increased coupling strength. This is independent of whether the coupling is changed by varying the NiO or Pt thickness and of the sign of the coupling. The IEC acts as an effective anisotropy field, increasing the average size of the domains by making it energetically harder to form domains.

MFM domain images measure both top and bottom [Co/Pt] layers. Here we once again see clear evidence for domain-by-domain coupling [3.7]. In addition, in AFM coupled samples, the competition between magnetostatic and IEC leads to a region of domain overlap [3.32]. This region increases in thickness as the IEC decreases. A simple model giving numerical values for the size of this domain overlap region as a function of coupling strength is found to closely agree with the experimental width obtained from the MFM data.

The temperature dependence of the strength of the IEC shows both irreversible changes (caused by oxidation/reduction reactions at the Co/NiO interface) and reversible changes (which we attribute to the temperature dependences of the myriad factors on which the coupling depends). The most striking feature in the temperature dependence is the fact that the coupling persists at temperatures well above the expected Néel temperature of this thin film of NiO, providing strong evidence for a stabilization of the ordering temperature in the presence of the ferromagnetic [Co/Pt].

3.7 Acknowledgements

The work at the University of Nebraska - Lincoln was supported by NSF (grants Nos. MRSEC DMR-0213808 and DMR-0203359) and the Nebraska Research Initiative. Use of the Advanced Photon Source was supported by the U.S. Department of Energy, Office of Science, Office of Basic Energy Sciences, under Contract No. W-31-109-ENG-38.

3.8 References

3.1. B. Dieny, V. S. Speriosu, S. S. P. Parkin, B. A. Gurney, D. R. Wilhoit, and D. Mauri, Phys. Rev. B **43** , 1297 (1991).

3.2. P. Grünberg, R. Schreiber, Y. Pang, M. B. Brodsky and H. Sowers, Phys. Rev. Lett. **57**, 2442 (1996).

3.3. M. N. Baibich, J. M. Broto, A. Fert, F. Nguyen Van Dau, F. Petroff, P. Etienne, G. Creuzet, A. Friederich, and J. Chazelas, Phys. Rev. Lett. **61**, 2472 (1988).

3.4. E. Popova, J. Faure-Vincent, C. Tiusan, C. Bellouard, H. Fischer, E. Snoeck, M. Hehn, F. Montaigne, V. da Costa, M. Alnot, S.Andrieu, and A. Schuhl, Appl. Phys. Lett. **81**, 509 (2002).

3.5. J. Faure-Vincent, C. Tiusan, C. Bellouard, E. Popova, M. Hehn, F. Montaigne, and A. Schuhl, Phys. Rev. Lett. **89**, 107206 (2002).

3.6. Z.Y. Liu and S. Adenwalla, Phys. Rev. Lett. **91**, 037207 (2003).

3.7. Z. Y. Liu, L. P. Yue, D. J. Keavney and S. Adenwalla, Phys. Rev. B **70**, 224423 (2004).

3.8. J. Unguris, R.J. Celotta, and D.T. Pierce, Phys. Rev. Lett. **67**, 140 (1991).

3.9. Eric E. Fullerton, K.T. Riggs, C.H. Sowers, S.D. Bader and A. Berger, Phys. Rev. Lett. **75**, 330 (1995).

3.10. S. Adenwalla, G.P. Felcher, Eric E. Fullerton and S.D. Bader, Phys. Rev. B **53,** 2474 (1996).

3.11. J.C. Slonczewski, J. Magn. Magn. Mater. **150,** 13 (1995).

3.12. J. Camarero, Y. Pennec, J. Vogel, M. Bonfim, S. Pizzini, F. Ernult, F. Fettar, F. Garcia, F. Lancon, L. Billard, B. Diney, A. Tagliaferri, and N. B. Brookes, Phys. Rev. Lett. **91**, 027201 (2003).

3.13. P.A.A. van der Heijden, C.H.W. Swuste, W.J.M. de Jonge, J.M. Gaines, J.T.W.M van Eemeren and K.M. Schep, Phys. Rev. Lett. **82**, 1020 (1999).

3.14. M. E. Filipkowski, J. J. Krebs, G. A. Prinz and C. J. Gutierrez, Phys. Rev. Lett. **75**, 1847 (1995).

3.15. Wofgang Kuch, Liviu I. Chelaru, Francesco Offi, Jing Wang, Masata Kotsugi and Jurgen Kirschner, Phys. Rev. Lett. **92**, 017201 (2004).

3.16. M. Y. Zhuravlev, E. Y. Tsymbal and S. S. Jaswal, Phys. Rev. Lett. **92**, 219703 (2004).

3.17. H.S. Oh and S.K. Joo, IEEE Trans. on Magn. **32**, 5, 4061 (1996).

3.18. Q. Meng, P.de Haan, W.P. van Drent, J.C. Lodder and Th.J. A. Popma, IEEE Trans. on Magn. **32**, 5, 4064 (1996).

3.19. T.K. Hatwar and C.F. Brucker, IEEE Trans. on Magn. **31**, 3256 (1995).

3.20. J. C. A. Huang, C. H. Lee and K. L. Yu, J. Appl. Phys. **89**, 7059 (2001).

3.21. S. H. Liou and Y. D. Yao, J. Magn. Magn. Mater. **190,** 130 (1998).

3.22. H. Ohldag, T. J. Regan, J. Stöhr, A. Scholl, F. Nolting, J. Lüning, C. Stamm, S. Anders and R. L. White, Phys. Rev. Lett. **87**, 247201 (2001).

3.23. T. J. Regan, H. Oldhag, C. Stamm, F. Nolting, J. Lüning, J. Stöhr and R. L. White, Phys. Rev. B **64**, 214422 (2001).

3.24. W.L. O'Brien and B.P. Tonner, Phys. Rev. B **50**, 12672 (1994).

3.25. Reiko Nakajima, J. Stöhr and Y.U. Idzerda, Phys. Rev. B **59**, 6421 (1999).

3.26. X-ray attenuation data can be found at http://www-cxro.lbl.gov/optical_constants/atten2.html.

3.27. M.P. Seah and W.A. Dench, Surface and Interface Analysis **1**, No. 1, 2 (1979)

3.28. Z.Y. Liu, G.H. Yu and Z.C. Wang, Phys. Rev. B **72**, 064451 (2005).

3.29. D.L. Abraham and H. Hopster, Phys. Rev. Lett. **58**, 1352 (1987).

3.30. M. T. Hutchings and E. J. Samuelsen, Phys. Rev. B **6**, 3447 (1972).

3.31. http://rsb.info.nih.gov/ij/

3.32. Olav Hellwig, Andreas Berger and Eric E. Fullerton, Phys. Rev. Lett. **91**, 197203 (2003).

3.33. E. Y. Tsymbal, Appl. Phys. Lett. **77**, 2740 (2000).

3.34. E.Y. Tsymbal, J. Magn. Magn. Mater. **130**, L6-L12 (1994).

3.35. J. Nogués, D. Lederman, T.J. Moran, Ivan K. Shuller and K.V. Rao, Appl. Phys. Lett. **68,** 3186 (1996).

3.36. S. Schwieger and W. Nolting Phys. Rev. B **69**, 224413 (2004).

3.37. P. Bruno and C. Chappert, Phys. Rev. Lett. **67**, 1602 (1991).

3.38. D. M. Edwards, J. Mathon, R. B. Muniz and M. S. Phan, Phys. Rev. Lett. **67**, 493 (1991).

3.39. P. Bruno, Phys. Rev. B **52**, 411 (1994).

3.40. Z. Zhang, L. Zhou, P.E. Wigen and K. Ounadjela, Phys. Rev. Lett. **73**, 336 (1994).

3.41. N. Persat and A. Dinia, Phys. Rev. B **56**, 2676 (1997).

3.42. B. Briner and M. Landolt, Europhys. Lett. **28**, 65 (1994).

3.43. S. Schwieger, J. Kienert and W. Nolting, Phys. Rev. B **71**, 174441 (2005).

3.44. D. Alders, L.H. Tjeng, F.C. Voogt, T. Hibma, G.A. Sawatzky, C.T. Chen, J. Vogel, M. Sacchi and S. Iacobucci, Phys. Rev. B **57**, 11623 (1998).

3.45. J. A. Borchers, R. W. Erwin, S. D. Berry, D. M. Lind, J. F. Ankner, E. Lochner, K. A. Shaw and D. Hilton, Phys. Rev. B **51**, 8276 (1995).

3.46. P. J. van der Zaag, Y. Ijiri, J. A. Borchers, L. F. Feiner, R. M. Wolf, J. M. Gaines, R. W. Erwin and M. A. Verheijen, Phys. Rev. Lett. **84**, 6102 (2000).

3.47. Ken Takano, Ph.D. Thesis, University of California-San Diego (1998).

3.48. Junsaku Nakajima, Akira Takahashi, Kenji Ohta and Toshio Ishikawa, J. Appl. Phys. **73,** 7612 (1993).

3.49. S. Hashimoto, J. Appl. Phys. **75** , 438 (1994).

3.50. K Kurosawa, M Miurat and S Saito, J. Phys. C: Solid St. Phys. **13**, 1521 (1980).

This chapter is based on the published paper: *Origin of Interlayer Exchange Coupling in [Co/Pt]/NiO/[Co/Pt] multilayers studied with XAS, XMCD, and micromagnetic modeling*, A. Baruth, D. J. Keavney, J. D. Burton, K. Janicka, E. Y. Tsymbal, L. Yuan, S. H. Liou, and S. Adenwalla, Phys. Rev. B **74**, 054419 (2006).

Chapter 4

Domain overlap in exchange-coupled [Co/Pt]/NiO/[Co/Pt] multilayers

4.1 Introduction

Magnetic thin films separated by a non-magnetic spacer layer exhibit interlayer exchange coupling (IEC). This coupling is either oscillatory (for metallic spacers [4.1, 4.2]) or monotonically decaying (for insulating spacers [4.3]) with spacer layer thickness. In [Co/Pt] multilayers with perpendicular anisotropy separated by an antiferromagnetic (AFM), insulating NiO spacer layer the IEC is facilitated by the canting of Ni spins in the NiO [4.4], resulting in a non-monotonic, oscillatory behavior [4.5, 4.6], where the coupling oscillates from ferromagnetic (FM) to AFM with NiO thickness. The period of oscillation corresponds to the AFM period in the NiO [4.5,4.6] and the coupling occurs domain-by-domain [4.7].

Previous data on the domain structures of films exhibiting IEC is somewhat limited. The domain structure of coupled multilayers has been investigated for Co/Cu/Ni [4.8], [Co/Pt]/Ru/[Co/Pt] [4.9] and recently for [Co/Pt]/NiO/[Co/Pt] [4.4]. For samples with perpendicular anisotropy that exhibit strong AFM coupling, ([Co/Pt]/Ru/[Co/Pt] and [Co/Pt]/NiO/[Co/Pt]), a relative shift between the domains of the top and bottom magnetic layers has been observed. This overlapping region has been attributed to a competition between the magnetostatic interaction and the AFM IEC, where the magnetostatic interaction tends to align the domains parallel whereas the AFM coupling favors antiparallel alignment [4.9]. In typical coupled systems, the AFM IEC is much larger than the magnetostatic interaction and the overlap region is small compared to the typical domain size.

In this chapter, using high resolution magnetic force microscopy (MFM) we perform a detailed study of the domain overlap in [Co/Pt]/NiO/[Co/Pt] multilayers with various strengths of the IEC. We develop a simple model that explains the formation of these regions and predicts the relationship between the overlap width and the magnitude of the IEC. The chapter is organized as follows: Sample preparation and experimental measurements are described in section 4.2. Experimental results and discussions involving magnetic force microscopy are found in 4.3. Section 4.4 presents the theoretical approach to analyzing the MFM data and a summary and conclusions are presented in section 4.5.

4.2 Sample Preparation and Experimental Techniques

Samples were sputtered on Si substrates from separate Pt, Co, and NiO targets with deposition rates of 0.56 Å/s, 0.26 Å/s, and 0.07 Å/s for Pt, Co, and NiO, respectively, in 2 mTorr Ar pressure with a base pressure of 3.8 x 10-8 Torr. The sample structure was

Si<111>/Pt(100Å)/[Pt(6Å)/Co(4Å)]$_3$/NiO(t_{NiO}Å)/[Co(4Å)/Pt(6Å)]$_3$/Cu(20Å)

t_{NiO} ranged from 7.5Å to 12Å.

The thickness calibration for series 1 was checked using an in situ quartz thickness monitor. The sample structure was checked for both series by X-ray diffraction. The Pt layers are polycrystalline, but are highly fcc (111) textured; the Co layers are highly hcp (100) textured, and the NiO layer is highly fcc (111) textured, similar to previously grown structures [4.4, 4.5, 4.7]. These samples have shown the oscillatory IEC previously described.

The MFM images (Figure 4.1) were made on virgin samples with different NiO thicknesses, corresponding to varying coupling strengths, in tapping/lift mode at a lift height of 5 nm under ambient conditions. The NiO thickness and the corresponding IEC strength, J_{IEC}, are both indicated on the individual figure panels. Note that positive (negative) J_{IEC} correspond to AFM (FM) coupling. The MFM tip, made by coating a 30 nm thick CoPt film on a cantilever, consists of a small magnetic CoPt particle (~ 30 nm) with a coercivity of about 15 kOe [4.10]. The MFM tips were magnetized so that the magnetization of the tip is perpendicular to the sample surface, pointing downward.

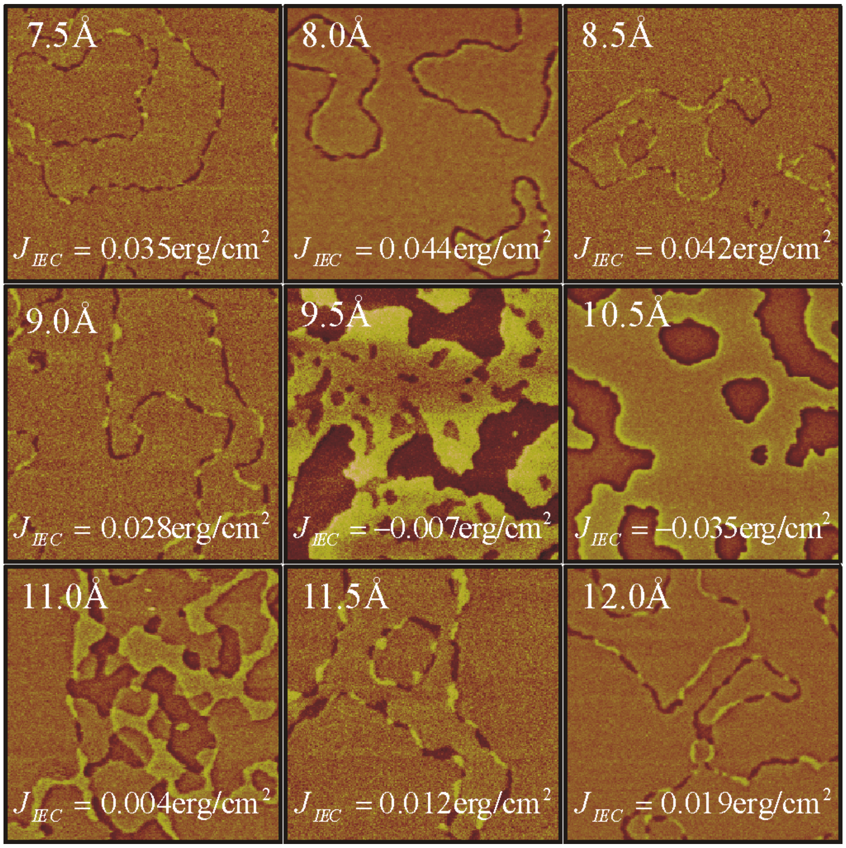

Figure 4.1:

MFM images of coupled Co/Pt multilayers, with different thicknesses of the NiO interlayer corresponding to the IEC values listed. In the images, light colored areas indicate a magnetization out of the page. Each image is 5µm x 5µm in size.

MFM measures the net magnetization through the depth of the sample, including both the top and bottom [Co/Pt] multilayers. There is a striking contrast between the FM and the AFM coupled samples. In FM coupled samples, the domain-by-domain coupling implies that an *up* (*down*) domain in the upper [Co/Pt] layer is in perfect alignment with an *up* (*down*) domain in the lower [Co/Pt] layer, leading to a net upward (downward) magnetization. In AFM coupled samples, an *up* (*down*) domain in the upper [Co/Pt] layer is in alignment with a *down* (*up*) domain in the lower [Co/Pt] layer, leading to a zero net magnetization. Hence in AFM coupled samples, the only contrast is seen in the regions of the domain walls where the magnetization changes from up to down, whereas in FM coupled samples, up and down domains are clearly visible. The rest of this chapter is devoted to the investigation of the domain wall regions in the AFM coupled samples.

4.3 Experimental Results and Discussion

Careful inspection of the images of AFM coupled samples reveals that rather than perfect alignment of domains, there is a slight shift between the domains in the upper and lower [Co/Pt] layers. The domain wall region possesses a net magnetic moment and is wider (>130nm) than the expected domain wall width in these films (14-22nm). This domain overlap region varies in width with J_{IEC}. Along the length of this overlap region, the magnetization switches from up to down. This is most clearly seen in the weaker coupled samples.

In order to investigate the width of the domain overlap region, regions that were fairly straight over a length scale of hundreds of nanometers were chosen. A representative set is shown in Figure 4.2. Line scans were taken perpendicular to the length of these regions and averaged along the length to improve statistics. The final data were obtained from three different overlap regions for each thickness of NiO. The black boxes in Figure 4.2 indicate one of the regions over which the width was averaged and the red lines indicate the average domain overlap width, obtained from the full width at half maximum (FWHM) of the line scans. Note that only regions where the magnetization was pointing downward (dark contrast) were analyzed to ensure uniformity in data across all domains of various samples of varying NiO thickness.

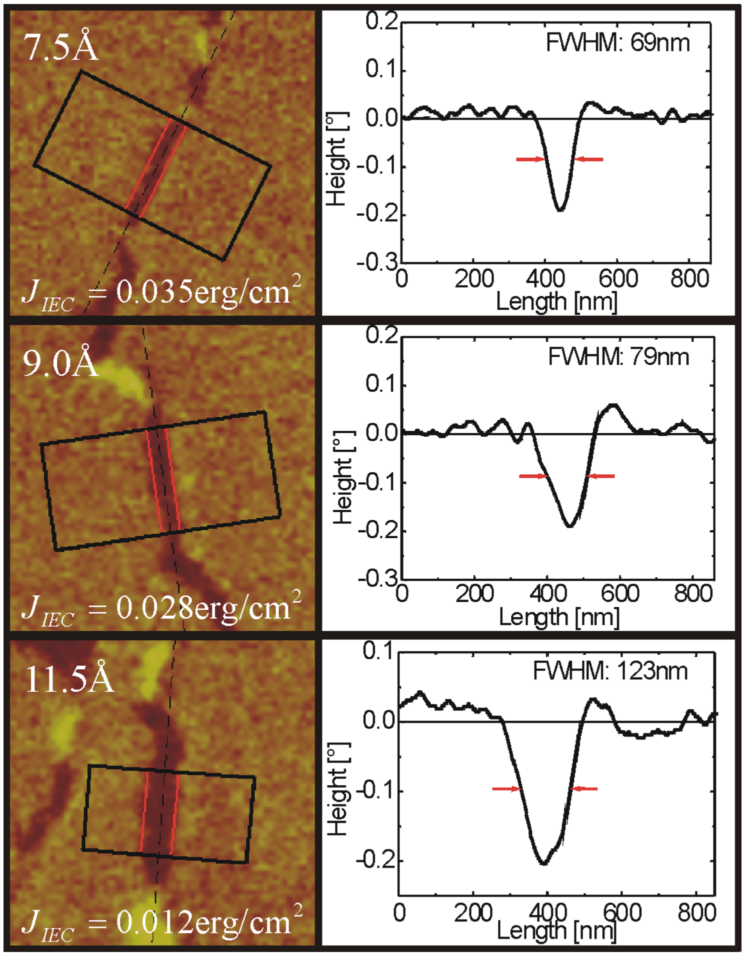

Figure 4.2:

Representative line scans for the 7.5, 9 and 11.5Å samples. The left panels show the region where the lines scans were performed, the black box indicates the region used for averaging and the red lines indicate the average domain overlap width. Each image is 1.25µm x 1.25µm in size. The right panel shows the corresponding lines scans, averaged over the region enclosed in the black box. The red arrows indicate the location of the red lines in the left panel and represent the FWHM of the features.

The origin of the overlap between antiparallel-aligned magnetic domains is the magnetostatic interaction. Magnetic stray fields which are produced by domains favor parallel alignment of the magnetic moments, competing with AFM IEC which aligns the magnetic moments antiparallel. For most samples, the IEC dominates the magnetostatic interaction and, if the magnetostatic coupling were homogeneous, the domains would align perfectly antiparallel with no overlap. The magnetostatic coupling, however, is strongly *inhomogeneous* over the surface due to the stray fields localized in the vicinity of the domain walls. This makes it energetically favorable to produce a shift δ between the antiparallel aligned domains to reduce the magnetostatic energy which has the highest density in the vicinity of the domain walls.

4.4 Theoretical Analysis of Domain Overlap

The energetics of the domain overlap can be described as follows. Assuming an abrupt domain wall at $x = 0$ separating two seminfinite domains lying in the x-y plane, as shown in Fig. 3, we find that the x- and z-components of the field produced by the bottom [Co/Pt] film are

$$H_x(x,z) = 2M_{bot} \ln\left(\frac{x^2 + (z-t)^2}{x^2 + z^2}\right), \tag{4.1}$$

$$H_z(x,z) = -4M_{bot}\left(\arctan\left(\frac{z-t}{x}\right) - \arctan\left(\frac{z}{x}\right)\right), \tag{4.2}$$

where z is the distance above the film, t is the film thickness, and M_{bot} is the saturation magnetization of the bottom film. A similar field is produced by the upper [Co/Pt] film (separated by a spacer of thickness d from the bottom film) with a domain wall at $x = \delta$ and magnetization M_{top}. For perfectly antiparallel-aligned domains with no overlap ($\delta =$ 0) the magnetostatic energy density, $U = H^2/8\pi$, is very large near the domain walls, as is evident from Figure 4.3(a). The separation of the domain wall of the top and bottom films leads to a significant reduction in the magnetostatic energy, as seen from the energy density plot shown in Figure 4.3(b), even for a very small δ = 4 nm.

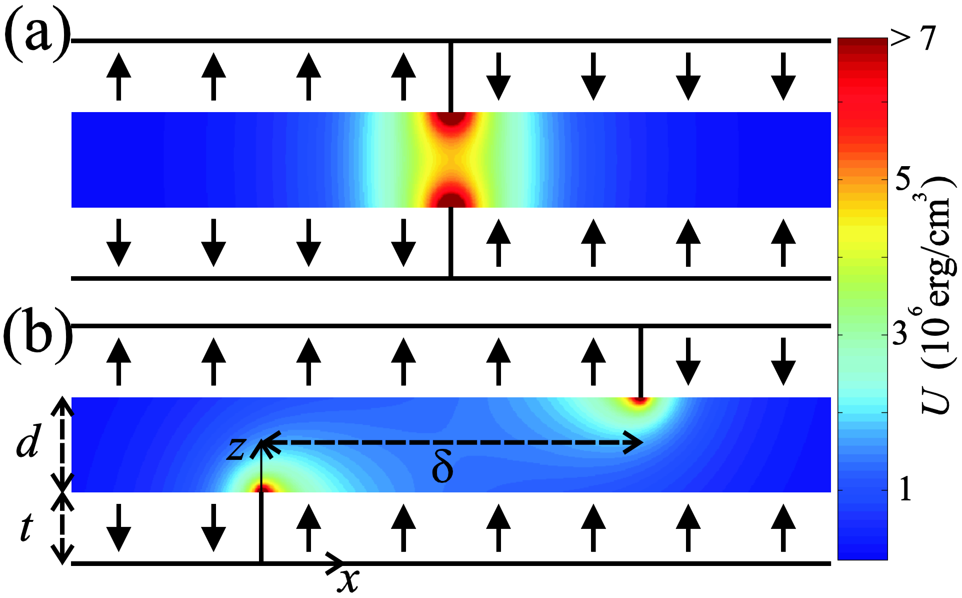

Figure 4.3:

Magnetostatic energy density for antiparallel-aligned domains with no overlap (a) and with overlap δ (b) for t = 3nm, d = 1nm, and δ = 4nm.

The reduction in the magnetostatic energy with increasing δ competes with the increase in the interlayer exchange energy per unit length, $J_{IEC}\delta$. The total energy per unit length $E(\delta)$ relative to $\delta = 0$ is

$$E(\delta) - E(0) = -2M_{top}\int_{t+d}^{2t+d}\int_{0}^{\delta} H_z(x,z)\,dxdz + J_{IEC}\delta\ . \qquad (4.3)$$

To find the equilibrium overlap we minimize this energy with respect to δ which leads to

$$\frac{\partial E}{\partial \delta} = -2M_{top}\int_{t+d}^{2t+d} H_z(\delta,z)\,dz + J_{IEC} = 0\ . \qquad (4.4)$$

For $\delta << d$, as appears to be the case in Figure 4.2, the magnetostatic field (Eq. 4.2) is reduced to $H_z(\delta,z) \approx 4M_{bot}t/\delta$, so that Eq. 4.4 results in a finite overlap given by

$$\delta = \frac{8M_{top}M_{bot}t^2}{J_{\mathrm{IEC}}}\ . \qquad (4.5)$$

Thus, the domain overlap width is inversely proportional to the magnitude of AFM coupling.

This result is consistent with our experimental data. Figure 4.4 shows the average domain overlap width, δ, obtained from the MFM lines scans in three different regions as a function of J_{IEC}. Previous experiments using a similar tip and experimental conditions as these scans show a resolution of 15nm [4.11]; hence we include error bars of ±15nm. A best fit to the data gives

$$\delta = \frac{a}{J_{\mathrm{IEC}}} + b\ , \qquad (4.6)$$

where a = (1.0 ± 0.1)$\times10^{-7}$erg/cm and b = (43.5 ± 3.7)$\times10^{-7}$cm. From Eq. 4.5, a is a measure of the magnetization of the [Co/Pt] multilayer. Assuming a Co thickness t of 1.2 nm for each layer and assuming an M_{top}=1.43M_{bot} ratio (from MOKE, SQUID and AGFM measurements [4.4]), we obtain M_{top} = 1109.7 emu/cm^3 and M_{bot} = 776.0 emu/cm^3, in excellent agreement with previous SQUID measurements that give values of M_{top} = 1087.7 and M_{bot}= 760.6 emu/cm^3. This is well within the range of previous measurements on [Co/Pt] multilayers, which have shown M_s values ranging from 600 to 2300 emu/cm^3 [4.12]. The offset of 43 nm is explained from a combination of the finite thickness of domain walls (an effect that is ignored in the model which assumes abrupt transitions between domains) and the resolution of the MFM tip. A convolution of a Gaussian stray field with a FWHM of 15 nm (from the MFM tip) with a domain wall of 20 nm, increases the width for each of the overlap features by 25-30 nm, nearly accounting for our offset within error bars.

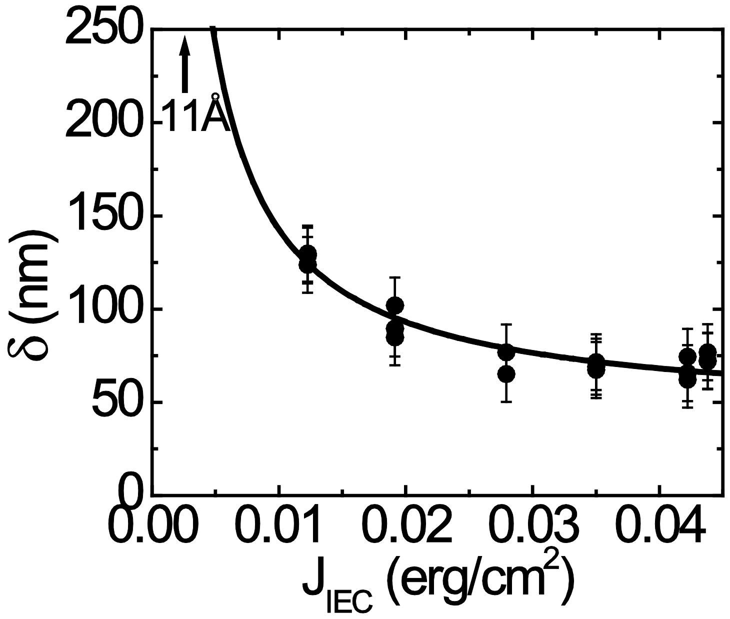

Figure 4.4:

Domain overlap width as a function of the coupling strength. Closed circles give the compiled line scan data for all samples. 15nm error bars account for MFM resolution. The solid line indicates the best fit to Eq. 4.2. The fit parameters are discussed in the text. The arrow corresponds to the coupling strength for the 11Å sample.

For the weakest coupled sample (t_{NiO}= 11Å), there is a wide variation in the width of the overlap region. In this sample, the IEC is very weak so that magnetostatic interactions determine the domain alignment. From the fit, we obtain an overlap width of 300 nm (as indicated in Figure 4.4 by the arrow), which agrees reasonably well with that in Figure 4.1.

For a full quantitative analysis of the overlap versus coupling strength, starting from a full magnetostatic calculation see Ref. 4.13.

4.5 Conclusions

In conclusion, we have shown that magnetic thin films with perpendicular anisotropy exhibiting AFM exchange coupling have domain overlap regions which can be quantitatively described by consideration of the stray fields that arise due to the domain walls, leading to a $1/J_{IEC}$ dependence of the domain overlap width. Taking into account the resolution of the MFM data collected, we have shown that this simple model gives an accurate explanation of the relationship between the region's size and strength of the coupling.

4.6 Acknowledgments

This research was supported by NSF (grants Nos. MRSEC DMR-0213808 and DMR-0203359), Nebraska Research Initiative and Seagate Research.

4.7 References

4.1. P. Grünberg, R. Schreiber, Y. Pang, M. B. Brodsky and H. Sowers, Phys. Rev. Lett. **57**, 2442 (1986).

4.2. S. S. P. Parkin, N. More and K. P. Roche, Phys. Rev. Lett. **64**, 2304 (1990).

4.3. J. Faure-Vincent, C. Tiusan, C. Bellouard, E. Popova, M. Hehn, F. Montaigne and A. Schuhl, Phys. Rev. Lett. **89**, 107206 (2002).

4.4. A. Baruth, D. J. Keavney, J. D. Burton, K. Janicka, E. Y. Tsymbal, L. Yuan, S. H. Liou, and S. Adenwalla, Phys. Rev. B **74**, 054419 (2006).

4.5. Z. Y. Liu and S. Adenwalla, Phys. Rev. Lett. **91**, 037207 (2003).

4.6. M. Ye. Zhuravlev, E. Y. Tsymbal and S. S. Jaswal, Phys. Rev. Lett. **92**, 219703 (2004).

4.7. Z. Y. Liu, L. Yue, D. J. Keavney and S. Adenwalla, Phys. Rev. B **70**, 224423 (2004).

4.8. W. Kuch, L. I. Chelaru, K. Fukumoto, F. Porrati, F. Offi, M. Kotsugi and J. Kirschner, Phys. Rev. B **67**, 214403 (2003).

4.9. O. Hellwig, A. Berger and E. E. Fullerton, Phys. Rev. Lett. **91** 197203 (2003).

4.10. S. H. Liou and Y.D. Yao, J. Magn. Magn. Mater. **190,** 130 (1998).

4.11. L. Gao, L. P. Yue, T. Yokota, R. Skomski, S. H. Liou, H. Takahoshi, H. Saito and S. Ishio, IEEE Trans. Magn. **40**, 2194 (2004).

4.12. Y.C. Cho, S.B. Choe, and S.C. Shin, Appl. Phys. Lett. **80**, 452 (2002); K.S. Moon, S.B. Choe and S.C. Shin, IEEE Trans. Magn. **32**, 4058 (1996).

4.13. K. Janicka, J. D. Burton, and E. Y. Tsymbal, J. Appl. Phys. **101**, 113921 (2007).

This chapter is based on the published paper: *Domain Overlap in antiferromagnetically coupled [Co/Pt]/NiO/[Co/Pt] multilayers,* A. Baruth, L. Yuan, S. H. Liou, J. D. Burton, K. Janicka, E. Y. Tsymbal, and S. Adenwalla, Appl. Phys. Lett. **89,** 202505 (2006).

Chapter 5

Domain size and structure in exchange-coupled [Co/Pt]/NiO/[Co/Pt] multilayers

5.1 Introduction

The higher areal densities required for magnetic recording technology require the use of materials with strong perpendicular anisotropy, and investigation of these systems could prove technologically useful [5.1]. They are expected to improve density, stability, and reliability of spin valves and magnetic tunnel junctions [5.2]. [Co/Pt] multilayers with perpendicular magnetic anisotropy (PMA) separated by a thin NiO spacer layer represent the only system being investigated that shows an oscillatory magnetic coupling that alternates between ferromagnetic (FM) and antiferomagnetic (AFM) with increasing spacer layer thickness in the perpendicular geometry [5.3]. The origin of this coupling is quite different from the oscillatory coupling seen between ferromagnetic films separated by metallic spacer layers. The oscillatory coupling for metallic spacers can be well understood as a consequence of the quantum interference model [5.4], in which multiple reflections of electron waves at the FM/spacer interfaces and their interference are considered. Then, the transition region between AFM and FM coupling in these structures follows from the $e^{2i\kappa_F D}$ dependence of the coupling, where D is the thickness of the spacer and κ_F is a parameter based on the Fermi level of the FM layers and the metallic barrier. In contrast, the oscillatory coupling that has been observed in FM/AFM/FM heterostructures with PMA arises from the exchange coupling at the

FM/AFM interface and is propagated across the AFM spacer layer via the AFM exchange [5.3,5.4]. In this case, the coupling oscillates with the period of the AFM ordering, transitioning from FM to AFM with each additional monolayer of the AFM thin film. The question then arises as to the behavior of coupling between each well-defined FM or AFM maxima. As the thickness of the AFM transitions between an odd number of layers (which favors FM ordering) or an even number of layers (which favor AFM ordering), magnetization measurements show that the coupling changes smoothly by decreasing in magnitude, crossing zero and then increasing with an opposite sign (figure 5.1). Wedge-shaped samples provide a method for exploring these regions with magnetic force microscopy (MFM).

5.2 Sample Preparation and Experimental Techniques

MFM provides a unique tool for observing the magnetic coupling via domain size and structure in these heterostructures with spatial resolution. In particular, this chapter investigates the correlation between magnetic domain size and the strength of the interlayer exchange coupling (IEC). This tool is used to look at the domain structure (both size and correlation between each [Co/Pt] layer) in the transition region from AFM to FM coupling.

Two identical samples were sputtered simultaneously on a Si substrate from separate Cu, Pt, Co, and NiO targets. Using an off-axis sputtering technique it was possible to produce a NiO layer wedge which ranged in thickness from ~6Å-20Å across 2” in lateral dimension and still maintain good texturing (higher angle wedges lead to a breakdown of NiO texturing – likely due to strain). The sample schematic is:

$$\text{Si}\langle 111\rangle/\text{Pt}(200\text{Å})/[\text{Pt}(6\text{Å})/\text{Co}(4\text{Å})]_3/\text{NiO}(t_{\text{NiO}}\text{Å})/[\text{Co}(4\text{Å})/\text{Pt}(6\text{Å})]_3/\text{Cu}(50\text{Å}),$$

where t_{NiO} ranged from 6Å to 20Å (figure 5.1). The NiO wedge shape was characterized using X-ray reflectivity (XRR) on a thicker wedge and scaled in time to the present thickness, where absolute thickness for the center of the NiO layer (along with the other layers) was checked with an *in-situ* crystal thickness monitor. X-ray diffraction shows that the Pt layers are polycrystalline but highly fcc (111) textured, this leads to a NiO layer that is also highly fcc (111) textured.

5.3 Bulk Magnetometry and MFM Measurements

Using one sample, bulk magnetization measurements were done at room temperature using a perpendicular magneto-optical kerr effect setup (PMOKE), where a mechanical translation technique was used to scan along the length of the NiO wedge and cross calibrate with the XRR data to correlate the coupling strength, J_{IEC}, with NiO thickness (figure 5.1). The second sample was kept virgin and was used to obtain the MFM images along the length of the wedge, corresponding to varying coupling strengths, in tapping/lift mode at a lift height of 5 nm under ambient conditions. Using a mechanical translation stage, the NiO thickness (from XRR) and the corresponding IEC strength, J_{IEC}, (from PMOKE) were again cross calibrated and are both indicated on the individual figure panels in figure 5.2. Note that positive (negative) J_{IEC} values correspond to AFM (FM) coupling. The MFM tip, made by coating a 30 nm thick CoPt film on a cantilever, consists of a small magnetic CoPt particle (~30 nm) with a coercivity of about 15 kOe

[5.6]. The MFM tips were magnetized so that the magnetization of the tip is perpendicular to the sample surface, pointing downward.

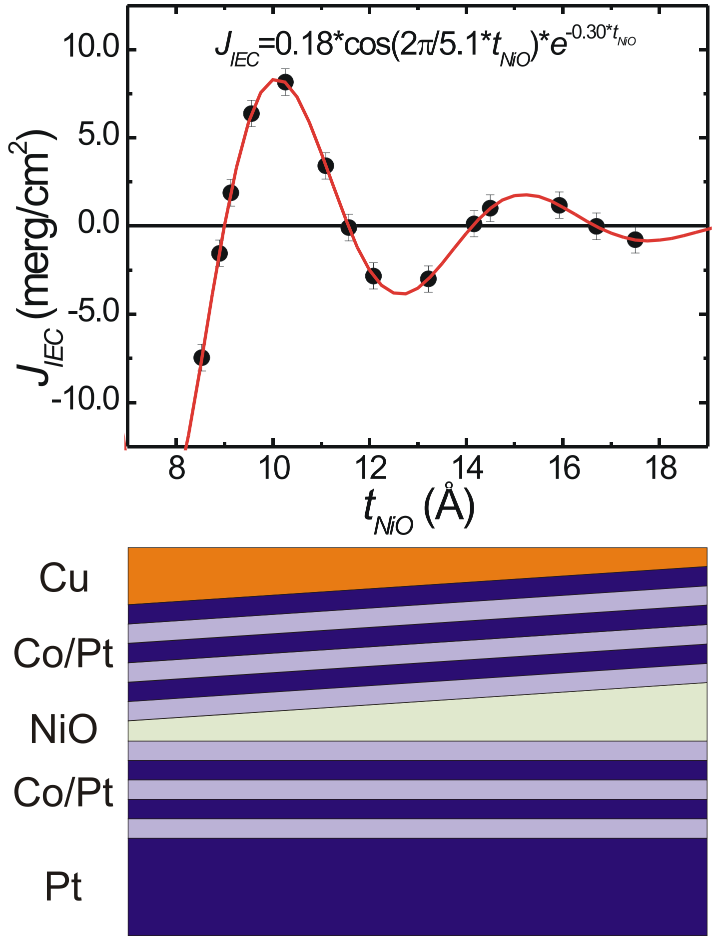

Figure 5.1:

Room temperature J_{IEC} values, based on minor loop shifts, are given for a variety of NiO thicknesses along the sample wedge (as indicated in the illustration). Above 8Å NiO thickness, the coupling smoothly oscillates with NiO thickness from antiferromagnetic to ferromagnetic coupling – the coupling disappears below 8Å due to pin-holes. This oscillation in coupling obeys a simple cosine function with an exponential damping.

MFM measures the net magnetization through the depth of the sample, including the top and bottom [Co/Pt] layers. Thus, for FM coupled samples only up and down domains are observed (the upper and lower layers' domains are in perfect registry). In contrast, the AFM coupled samples have anti-parallel alignment leading to zero net magnetization; however, in the vicinity of the domain walls FM stripes are observed, leading to three separate levels of contrast. These FM stripes have already been well characterized [5.5,5.7-5.9] and are a result of a competition between the AFM coupling and the magnetostatic interlayer interaction between the two [Co/Pt] layers.

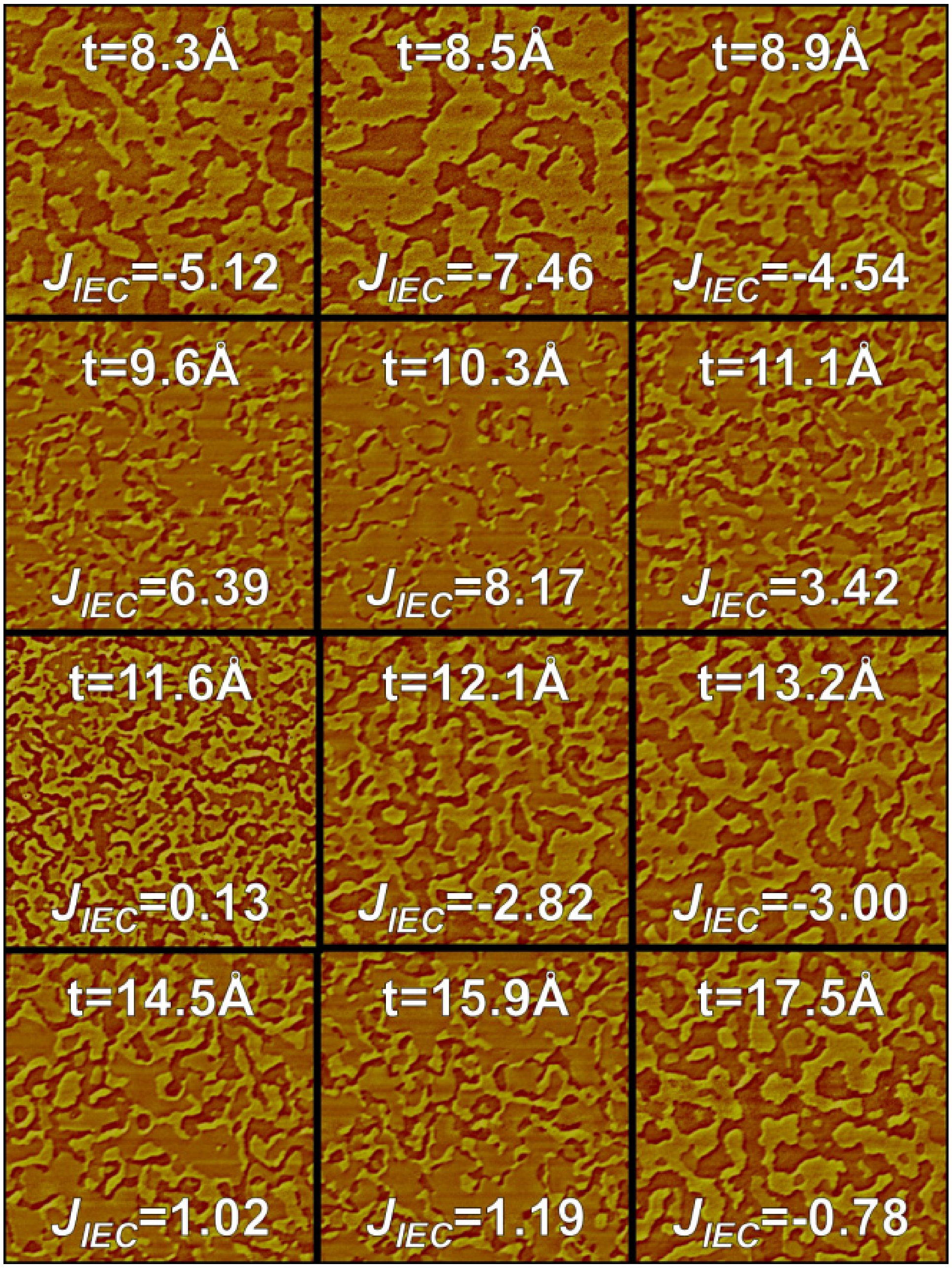

Figure 5.2:

MFM images of coupled [Co/Pt] multilayers, with different thicknesses of the NiO layer corresponding to the position along the wedge. The strength of the interlayer exchange coupling listed (in units of merg/cm^2) is based on PMOKE data taken at each position. In the images, light colored areas indicate a magnetization out of the page. Each image is 5 x 5 μm^2 in size.

Using ImageJ, a public domain Java image processing program inspired by NIH Image for the Macintosh [5.10], the average domain size was determined for each MFM image. ImageJ was designed with an open architecture that provides extensibility via Java plug-ins. Using one such Java plug-in, we were able to determine the average size of each domain. This particular plug-in allows the user to define a boundary (domain edge) and then mask all domains. For the FM coupled regions, this boundary was defined by the sharp contrast across a domain wall (transition from up to down domains), where the boundary was defined as the center of this sharp contrast. Thus, we only measured the size of domains that correspond to both [Co/Pt] magnetizations pointing up. For the AFM coupled regions, the FM region in the vicinity of the domain wall defined the boundary between domains, where the center of this FM stripe defined the exact boundary. For the AFM coupled case, the up/down and down/up domains are indistinguishable, so a determination was made to choose the smaller of the two regions (this is consistent with the FM coupled case). The areas of these masked domains are then separated into 256 bins and plotted as a histogram. From this histogram an average size and spread in size could be determined. A direct, monotonic correlation between the magnitude of the coupling strength and domain size was established, where the error bars give a measure of the spread in domain size (figure 5.3). Note that this effect is independent of the sign of the coupling (whether FM or AFM).

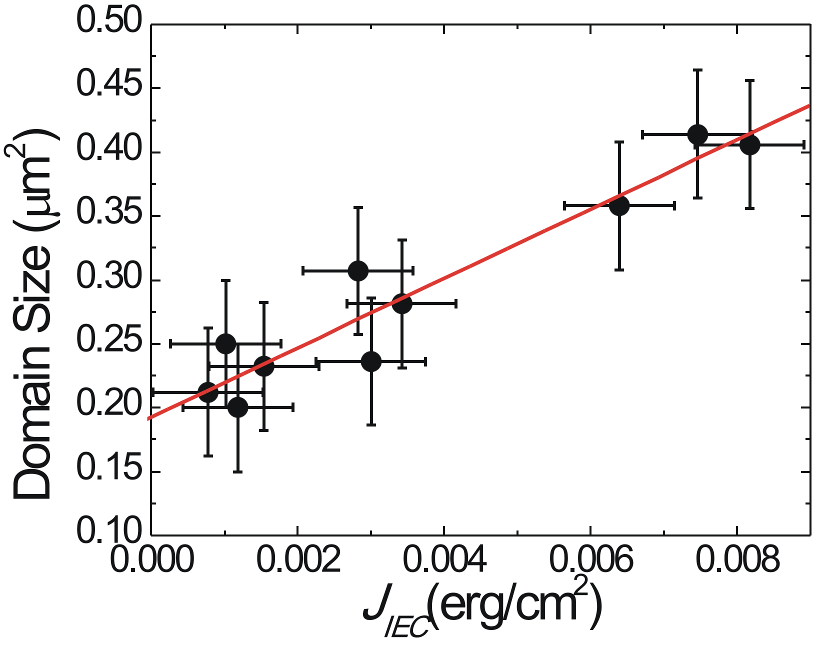

Figure 5.3:

Average up domain size is given as a function of $J_{IEC.}$ The average domain size increases monotonically with increased coupling strength. An assumed linear fit is presented, where the minimum domain size (i.e. zero IEC) is found to be 0.19 μm^2. Domain size error bars give an indication of the spread in sizes amongst the various up domains.

5.4 Discussion of Domain Size versus Coupling

Excluding the IEC between the two [Co/Pt] layers, the natural domain size is governed by the magnetostatic intralayer energy ($E_M^{(0)}$), the magnetostatic interlayer energy ($E_M^{(1)}$) and the domain wall energy (E_{dw}). $E_M^{(0)}$ decreases with decreasing domain size, favoring a smaller domain size. In addition, $E_M^{(1)}$ further decreases the total magnetostatic energy. The total magnetostatic energy is competing with E_{dw}, which increases with decreasing domain size due to the increasing number of domain walls per unit area. In general, this competition leads to relatively small domains that decrease in size as the thickness of the films or their separation gets larger [See Ref. 5.9]. To get an estimate of these energy contributions for our particular system, using a stripe model for domain formation (seen in films with PMA), the magnitudes of the $E_M^{(0)}$ and $E_M^{(1)}$ energy densities are roughly

$$E_M^{(0)} = \frac{16M^2L}{\pi^2 t}\sum_{n=1,3,5\dots}^{\infty}\frac{1}{n^3}\left(1-e^{-\frac{n\pi t}{L}}\right) \approx 3.6\times 10^6\ {}^{\mathrm{erg}}\!/_{\mathrm{cm}^3} \tag{5.1}$$

$$E_M^{(1)} = -\frac{8M^2L}{\pi^2 t}\sum_{n=1,3,5\dots}^{\infty}\frac{1}{n^3}e^{-\frac{n\pi d}{L}}\left(1-e^{-\frac{n\pi t}{L}}\right)^2 \approx -0.017\times 10^6\ {}^{\mathrm{erg}}\!/_{\mathrm{cm}^3}. \tag{5.2}$$

This assumes a Co thickness $t = 1.2\times 10^{-7}\mathrm{cm}$ (from XRR), a separation $d = 1.1\times 10^{-7}\mathrm{cm}$ (from XRR), a saturation magnetization $M = 760\ \mathrm{emu/cm^3}$ (from SQUID mesurements), and an average domain size (actually stripe width in this model) $L = 1.0\times 10^{-4}\mathrm{cm}$ (noting that neither energy value depends heavily on the value of L in the vicinity of a micron domain size). Note that $E_M^{(1)}$ is quite small in comparison to $E_M^{(0)}$. However, for a given heterostructure, $E_M^{(0)}$ should be a constant (*i.e.* the thickness of the film does not change). These two energy contributions would favor small domains, but they are combated by the domain wall energy

$$E_{dw} = \frac{\sigma}{L} = \frac{4\sqrt{AK}}{L} \approx 0.057\times 10^6\ {}^{\mathrm{erg}}\!/_{\mathrm{cm}^3}. \tag{5.3}$$

The exchange stiffness constant $A = 1.0\times 10^6\ {}^{\mathrm{erg}}\!/_{\mathrm{cm}}$ and the uniaxial perpendicular anisotropy constant $K = 2.0\times 10^6\ {}^{\mathrm{erg}}\!/_{\mathrm{cm}^3}$. This energy density favors larger domains.

Now, we compare these energy values with the additional energy contribution from the IEC. As indicated in figure 5.1, from MOKE measurements, the values of surface energy, J_{IEC}, range from $-7.46 \times 10^{-3}\ {}^{\mathrm{erg}}\!/_{\mathrm{cm}^2}$ to $8.17 \times 10^{-3}\ {}^{\mathrm{erg}}\!/_{\mathrm{cm}^2}$. If we scale these surface energies by the Co thickness, t, we get an effective field term,

$$\frac{J_{IEC}}{t} = \frac{M_s H_{IEC}\, t}{t} = M_s H_{IEC}. \tag{5.4}$$

The energy density values for this Zeeman-like term range from $-0.062 \times 10^{6}\ {}^{\mathrm{erg}}\!/_{\mathrm{cm}^3}$ to $0.068 \times 10^{6}\ {}^{\mathrm{erg}}\!/_{\mathrm{cm}^3}$. Thus, at the FM and AFM coupling maxima, the energy values are roughly four times larger than $E_M^{(1)}$, and are comparable with E_{dw} (this is why the FM stripe is observed in the AFM coupled samples [5.11]). Thus, the IEC plays a dominant role over $E_M^{(1)}$ as an effective field. $E_M^{(0)}$ is constant and independent of any change in $E_M^{(1)}$ or J_{IEC}, thus it is not considered when discussing the change in domain size. The sign of this effective field (*i.e.* FM or AFM) is not important; just as the sign of an externally applied field (Zeeman term) would not be important when considering domain size, except for determining which domains grow at the expense of the others. Thus, the domains aligned parallel to this effective field, H_{IEC}, will grow at the expense of the anti-parallel aligned domains, tending towards larger parallel aligned domains when the coupling is stronger. Likewise, a decrease in the coupling lowers the energy cost for domain formation and $E_M^{(1)}$ becomes more important, leading to the formation of smaller domains for the weakly coupled samples to minimize this magnetostatic energy.

5.5 Discussion of Domain Size for weak Interlayer Exchange Coupling

In the limit of very weak IEC (below 25% of maximum), the system is dominated by the relatively weak $E_M^{(1)}$. Thus, the $E_M^{(0)}$ will produce a characteristic domain size for each [Co/Pt] layer, but the domains in each [Co/Pt] layer will be out of registry with the neighboring [Co/Pt] layer due to the weak interlayer interactions. In the MFM images, three levels of contrast are easily seen and the [Co/Pt] layers appear to be completely decoupled (see figure 5.2 for 11.6Å). To further investigate this region, figure 5.4 shows MFM images taken at 100μm steps through the transition region around $t_{NiO} = 11.6$Å.

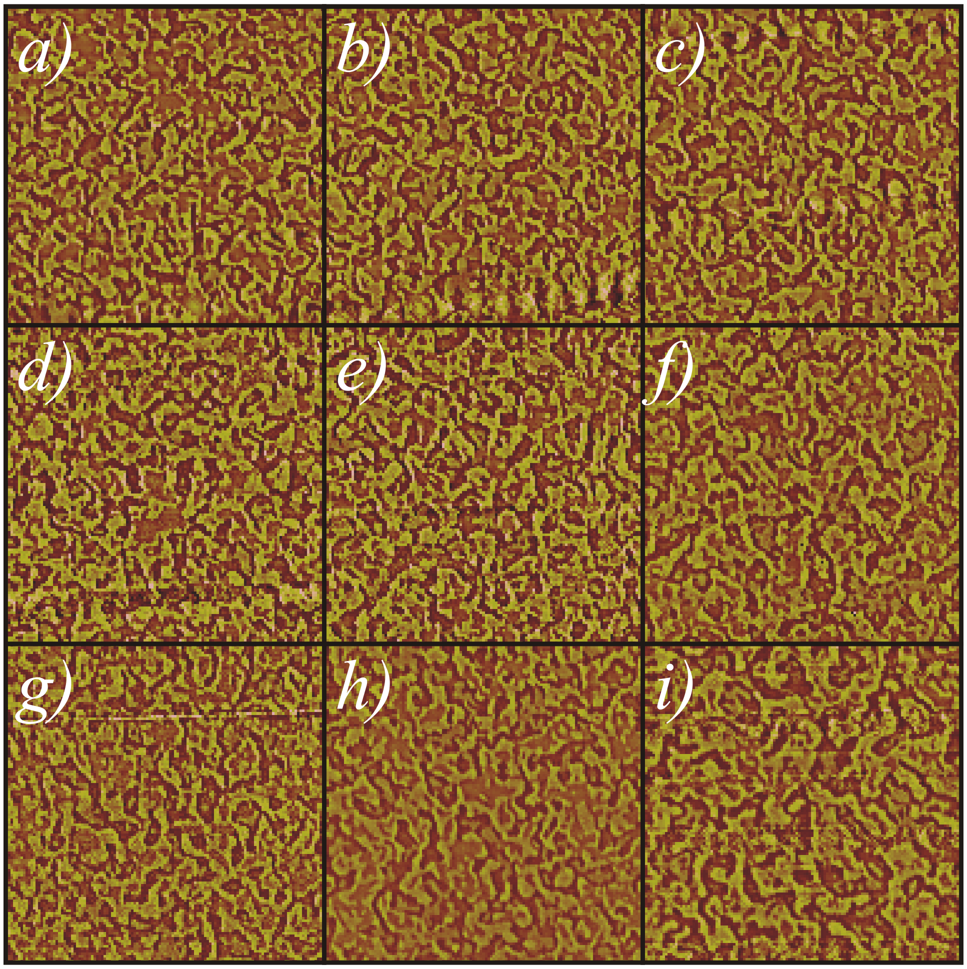

Figure 5.4:

MFM images of weakly coupled [Co/Pt] multilayers, with slightly different thicknesses of the NiO layer corresponding to the position along the wedge. Each image corresponds to a 0.1 mm step along the wedge in the transition region from AFM to FM coupling. The total change in NiO thickness for the entire series is ~0.2Å. In this region, the domain size increases slightly while the structure appears to be consistent. Each image is 5 x 5 μm^2 in size.

Based on the observed domain structure, we expect that the first images correspond quite closely to $J_{IEC} = 0$, and the remaining images correspond to $J_{IEC} < 0$, slightly decreasing (increasing negative) with each image. Throughout this entire region, which corresponds to a total variation in NiO thickness of ~0.2Å, there is essentially no difference in domain structure; however, a slight increase in up/up (yellow) domain size seems apparent from figure 5.4. Similar to figure 5.2, using ImageJ, the up domains were masked off and the sizes of these domains were investigated. This analysis showed that their size did increase along this 1mm length (~0.2Å NiO thickness variation), seen in figure 5.5. In this region, J_{IEC}, becomes nearly negligible compared to $E_M^{(1)}$, and $E_M^{(1)}$ is too weak to correlate the top and bottom domains. So, the observed MFM domain structure is expected, where the slight increase in magnitude of J_{IEC} leads to a slightly larger effective field. The beginning of a slight correlation in the upper and lower [Co/Pt] layers can just barely be seen, leading to the observed increase in up/up domain size.

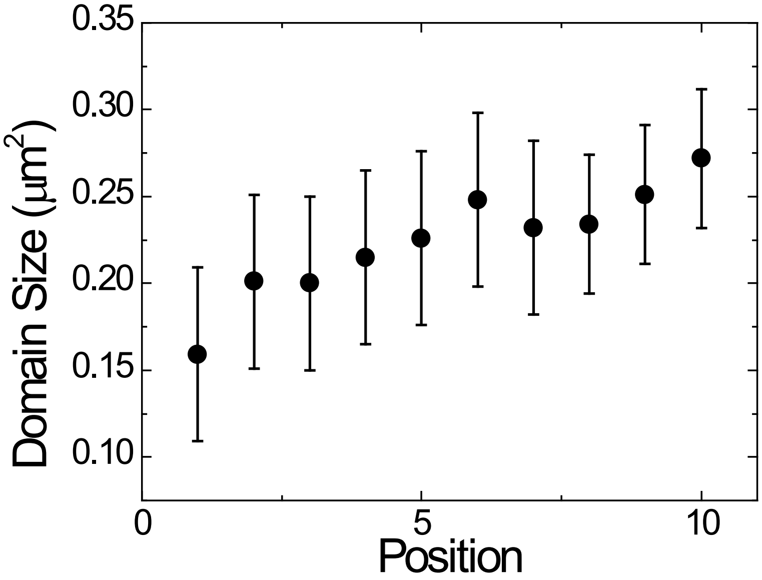

Figure 5.5:

Average up domain size is given as a function of position along the wedge in the vicinity of $t_{NiO} = 11.6\text{Å}$. The average up domain size increases with the slight increase in FM coupling. Domain size error bars give an indication of the spread in sizes amongst the various up domains.

Returning to figure 5.2, it is apparent that the transition from AFM coupling to FM coupling is governed by the relative areas of regions of a particular sign of coupling. As the thickness of the NiO film transitions between odd (n) and even (n+1) numbers of monolayers, when the wedge is traversed in the direction of increasing thickness, the area of regions with (n+1) monolayers increases. These regions must be significantly smaller than a magnetic domain, or a uniform domain-by-domain coupling, as observed, would not be anticipated. In this scenario, the net macroscopic coupling (seen with PMOKE) will then be determined by the region of larger area, where the magnitude is weighted by the presence of both (n) and (n+1) monolayers. Although, these differing regions can not be imaged because they average within a single magnetic domain, a consequence of this effect is apparent in the MFM data. In the domain wall region of the AFM coupled samples a FM stripe is formed. As the IEC decreases, the width of this FM stripe increases as $1/J_{IEC}$ since $E_M^{(1)}$ is relatively constant (favoring FM alignment) and the AFM IEC is decreasing [5.11]. Once the macroscopic IEC goes below the critical magnitude of ~25% of maximum it is weaker than $E_M^{(1)}$ and the FM stripes now form into full FM domains, governed by $E_M^{(0)}$, $E_M^{(1)}$ and E_{dw}. In this region, the number of (n) and (n+1) regions are nearly identical and cause the coupling energy to be very weak (both magnetostatic and IEC). In this case, the domains in each [Co/Pt] layer are no longer in registry with one another, as indicated by the complex domain structures in figure 5.4.

5.6 Conclusion

In conclusion, detailed MFM studies have been performed on oscillatory coupled [Co/Pt] layers with PMA across a NiO wedge spacer. There is a direct, monotonic relationship between domain size and the interlayer exchange coupling strength (independent of sign). The IEC serves as an effective field that leads to larger domain sizes. When the magnitude of the IEC energy drops below the interlayer magnetostatic interaction energy between the two layers, the domain size reaches a fundamentally small size, independent of IEC, and displays a decoupling between the two [Co/Pt] layers. These results are important for application of magnetic layered structures with PMA, as this is the only studied system that displays oscillatory coupling (with changing sign) in a perpendicular geometry.

5.7 Acknowledgements

This work was supported by NSF MRSEC DMR-0213808 and 0820521.

5.8 References

5.1. S. Mangin, D. Ravelosona, J. A. Katine, M. J. Carey, B. D. Terris, and E. E. Fullerton, Nature Mater. **5**, 210 (2006).

5.2. N. Nishimura, T. Hirai, A. Koganei, T. Ikeda, K. Okano, Y. Sekiguchi, and Y. Osada, J. Appl. Phys. **91**, 5246 (2002).

5.3. Z. Y. Liu and S. Adenwalla, Phys. Rev. Lett. **91**, 037207 (2003).

5.4. P. Bruno, J. Magn. Magn. Mater. **121**, 248 (1993); Europhys. Lett. **23**, 248 (1993); Phys. Rev. B **49**, 13231 (1994); Phys. Rev. B **52**, 52 (1995).

5.5. A. Baruth, D.J. Keavney, J. D. Burton, K. Janicka, E.Y. Tsymbal, L. Yuan, S.H. Liou and S. Adenwalla, Phys. Rev. B **74**, 054419 (2006).

5.6. S. H. Liou and Y.D. Yao, J. Magn. Magn. Mater. **190**, 130 (1998).

5.7. O. Hellwig, A. Berger and E. E. Fullerton, Phys. Rev. Lett. **91**, 197203 (2003).

5.8. Olav Hellwig, Andreas Berger, Jeffrey B. Kortright and Eric E. Fullerton, J. Magn. Magn. Mater. **319**, 13 (2007).

5.9. K. Janicka, J. D. Burton, and E. Y. Tsymbal, J. Appl. Phys. **101**, 113921 (2007).

5.10. http://rsb.info.nih.gov/ij/

5.11. A. Baruth, L. Yuan, J. D. Burton, K. Janicka, E.Y. Tsymbal, S.H. Liou and S. Adenwalla, Appl. Phys. Lett. **89**, 202505 (2006).

This chapter is based on the to-be-submitted paper: *Domain size and structure in exchange-coupled [Co/Pt]/NiO/[Co/Pt] multilayers,* A. Baruth, S. H. Liou, and S. Adenwalla, Appl. Phys. Lett. (2009).

Chapter 6

Enhanced blocking temperature and isothermal control of hysteresis loop shifts in Co/NiO/[Co/Pt] heterostructures with orthogonal easy axes

6.1 Introduction

The exchange bias (EB) effect [6.1] is a fundamental aspect of most realized spintronic devices [6.2,6.3]. This effect takes place at the interfaces of magnetic heterostructures and has been shown in ferromagnetic/antiferromagnetic (FM/AFM) and FM/ferrimagnetic bilayers as well as soft/hard FM bilayers. EB is evidenced, among other effects, by a hysteresis loop shift (LS) along the field axis and an enhancement of the coercivity (Hc). The anisotropy constants of the AFM layer play a pivotal role in determining the minimum thickness and maximum temperature range over which EB exists. The magnitude of the LS depends on several intrinsic parameters including the exchange interaction at the FM/AFM interface, interface roughness, micromagnetic structure and thickness. However, it is also possible to tune the EB externally; for example, field cooling in a variety of magnetic states [6.4-6.6] or extremely large field excitations [6.7]. These approaches are often tedious and prove inconvenient in a practical setting and thus are unlikely to be suitable for real world application. Recent isothermal approaches attempting to manipulate the interfacial magnetic spins include a [Pt/Co]/NiFe system, where an in-plane surface magnetization is attributed to Néel-type flux closure caps at the interface between the two FM layers leading to a NiFe loop shift

[6.8] and a Fe/Cr_2O_3/Fe system displaying a tunable exchange bias with moderate set fields (<10 kOe) [6.9].

Engineered spin valve structures in magnetic memory devices require stable operation at temperatures well above room temperature. For AFM materials with low anisotropy constants, this implies a rather large thickness in order to stabilize the LS at higher temperatures, an undesirable constraint given the requirements for high density recording. Heterostructures comprised of Co/NiO(11Å)/$[Co/Pt]_5$ with easy axes perpendicular ([Co/Pt]) and parallel to (Co) the plane of the film are the focus of this study. They display an isothermally tunable in-plane LS at room temperature (RT) and an unusually high blocking temperature (TB). The small thickness and weak in-plane anisotropy of the AFM NiO layer would normally restrict the EB to temperatures below 30K [6.10,6.11]; it will be shown that the presence of the [Co/Pt] layer plays a pivotal role in stabilizing NiO grains and dynamically manipulating them (via in-plane set fields), thereby tuning the observed LS.

6.2 Experimental Techniques

Samples were prepared by dc and rf magnetron sputtering from separate Pt, Co, NiO and Cu targets on similarly sized 4mm x 4mm Si substrates deposited in 2 mTorr Ar pressure with a base pressure of $\sim 3\times10^{-8}$ Torr and consisted of

Sample A: Si/Pt(200Å)/Co(40Å)/NiO(11Å)/$[Pt(6Å)/Co(4Å)]_5$/Cu(100Å).

In order to understand the individual role of each magnetic layer, the constituent parts were also grown:

Sample B: Si/Pt(200Å)/Co(40Å)/NiO(11Å)/Cu(100Å) and

Sample C: Si/Pt(200Å)/NiO(11Å)/[Pt(6Å)/Co(4Å)]$_5$/Cu(100Å).

The thickness calibrations for these structures were checked using an in situ quartz crystal monitor. Crystal structure was measured by X-ray diffraction; the Pt layers are polycrystalline, but are highly fcc (111) textured; the Co layers are highly hcp (100) textured, and the NiO is polycrystalline but is shown to be strongly fcc (111) textured perpendicular to the film plane. Bulk NiO crystallizes in the rock salt (NaCl) structure, undergoing a slight rhombohedral distortion on cooling through the Néel temperature [6.12]. The spins order in antiferromagnetically coupled ferromagnetic (111) sheets within which the spins point in the $(11\overline{2})$ directions. We assume the bulk ordering structure for this thin NiO film, with the antiferromagnetic order parameter perpendicular to the sample surface. Due to the lack of in-plane order, all possible spin orientations exist within the plane.

Extensive experiments on numerous previous samples with similar NiO thicknesses [6.13] grown under identical growth conditions in the same chamber indicate that above a thickness of 7Å the NiO layer is pinhole free as evidenced by antiferromagnetic coupling at thicknesses of 7Å and above. In addition, careful x-ray absorption spectroscopy (XAS) and x-ray reflectivity measurements on samples with similar thicknesses of NiO [6.13] indicate that the Co/NiO interfaces are clean and abrupt.

Room temperature magnetic characterization of samples was done using alternating gradient field magnetometry (AGFM), while temperature dependent characterization was done using the magneto-optic Kerr effect (MOKE) while in vacuum using a Janis cryostat with polarization preserving optical windows.

6.3 Loop Shifts at Room Temperature and Below

The measurements described below consist of both major and minor hysteresis loops. To avoid confusion, the upper (lower) curve of the hysteresis loop is defined as corresponding to the curve starting from positive (negative) field.

The magnetization loops of the constituent samples B and C are described first. The hysteresis loop for sample B is a typical square easy axis hysteresis loop, with an H_c of 46 Oe and a saturation field of ~250 Oe (Figure 6.1). For sample C, all measurements reported were made following perpendicular saturation to ensure that the [Co/Pt] layers were single domain. The major in-plane hysteresis loop of sample C (Figure 6.1) exhibited the expected S-shaped hysteresis loop typical of a hard axis magnetization rotation mechanism, but with a non-zero remanent magnetization (M_R). The in-plane saturation field is ~3.5 kOe; however, the loop displays hysteresis between ±2.75 kOe leading to an M_R value of ~26% of the saturation magnetization. To elucidate the behavior of sample A, minor loops were measured on sample C between ±250 Oe, corresponding to the saturation value of the in-plane Co layer. These minor loops were measured after a variety of in-plane set fields, H_{set}, were applied to the sample. Since the

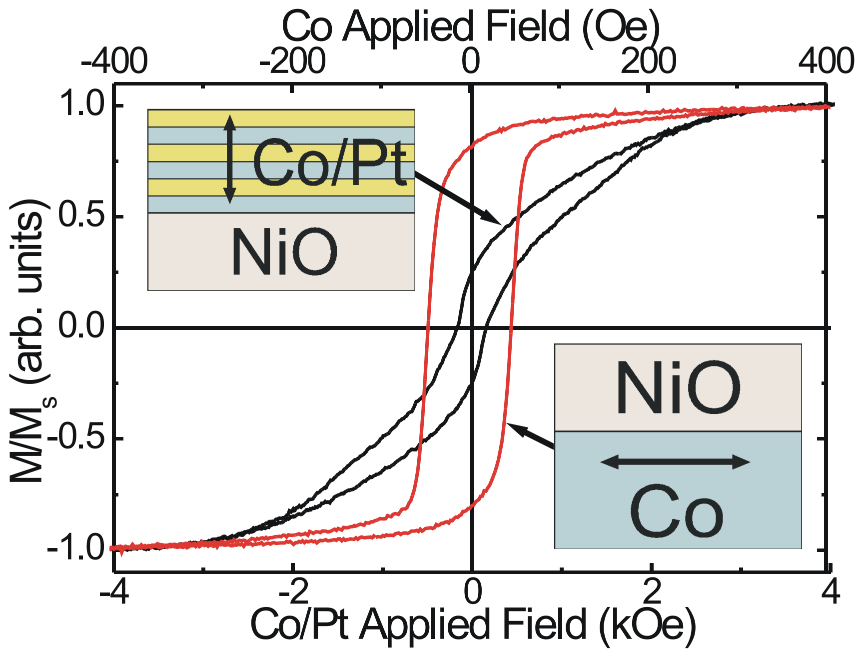

Figure 6.1:

In-plane magnetization curves for samples b and c at room temperature. The thin films structures are also indicated. The Co/Pt layer has the expected hard axis s-shaped curve with a non-zero remanence value that is ~26% of saturation. The Co loop is square and is symmetric about the magnetization axis.

field effectively cycles from the H_{set} value, to -250 Oe, and back to +250 Oe the minor loops show an asymmetry, corresponding to differing values of M_R and H_c for the upper and lower curves of the hysteresis loop. This asymmetry increases with an increase of H_{set} up to a value of ~2.75 kOe, corresponding to the closing of the full in-plane hysteresis loop for the [Co/Pt] multilayer (Figure 6.1). Two representative loops following an applied H_{set} of 2.75 kOe and 0.5 kOe are shown in Figure 6.2 displaying this change in asymmetry. Above H_{set} = 2.75 kOe, further increases in magnetization with increasing field are solely due to reversible, rotational processes and the asymmetry of the minor loop is fixed. Based on this correlation between H_{set} and the [Co/Pt] in-plane magnetization asymmetry, for the remainder of the experiment the field H_{set} serves only as a measure of the asymmetry of the [Co/Pt] minor loop.

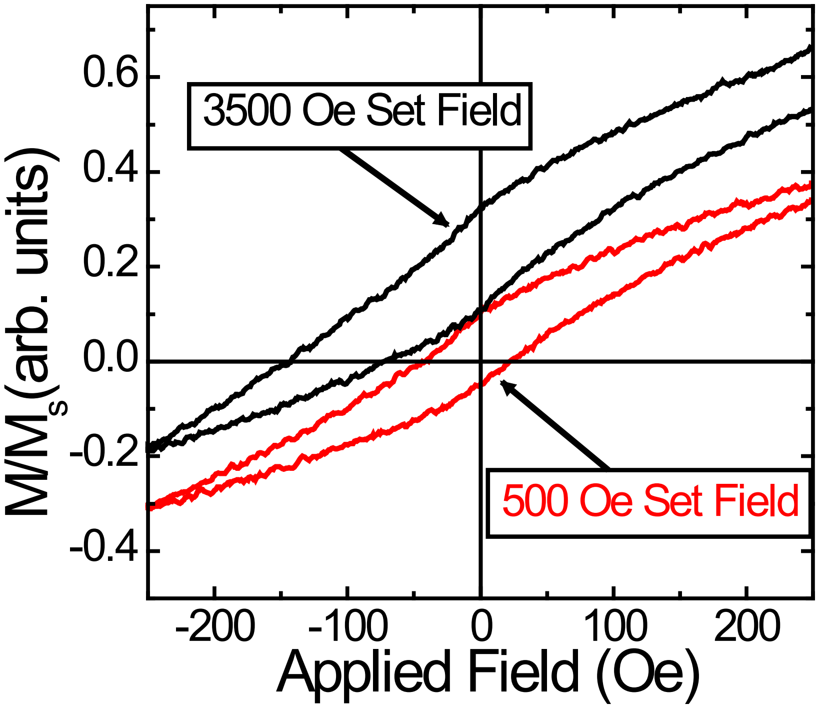

Figure 6.2:

Two minor in-plane, [Co/Pt]/NiO magnetization loops, one from +3.5kOe to -250 Oe and one from +500 Oe to -250 Oe. The asymmetry in the in-plane magnetization increases with increasing set field.

In-plane magnetization measurements of sample A (the entire heterostructure), taken between ±250 Oe at RT, are shown in the inset to Figure 6.3. Similar to measurements on sample C, in order to control the in-plane component of magnetization in the [Co/Pt], the sample is magnetized perpendicular to the plane of the film to produce a single domain state, followed by the application of H_{set}, which induces the in-plane component of magnetization. The magnitude of H_{set} is varied from 250 to 3500 Oe (based on the magnetic properties of the [Co/Pt] multilayer discussed above), which serves to increase the asymmetry of the in-plane component of magnetization in the [Co/Pt] multilayer. For each value of H_{set}, corresponding to a particular in-plane magnetization of the [Co/Pt] layer, in-plane magnetization measurements between ±250Oe (sufficient to switch and saturate the in-plane Co layer) were taken. The result of these measurements is shown in Figure 6.3. At H_{set} values between 250 Oe and 3 kOe, the upper curve shows a steady increase in H_c while the lower curve remains essentially unchanged. This leads to an increasing LS along the field axis for the Co magnetization with increasing H_{set} [6.14]. Increasing H_{set} above 3 kOe results in a symmetric increase in H_c for both the upper and lower curves of the loop such that the LS saturates at a H_{set} of 3 kOe. A similar behavior has been seen for a wide variety of samples with differing NiO thicknesses; in all cases, the loop shifts and the dependence on the set field are qualitatively similar.

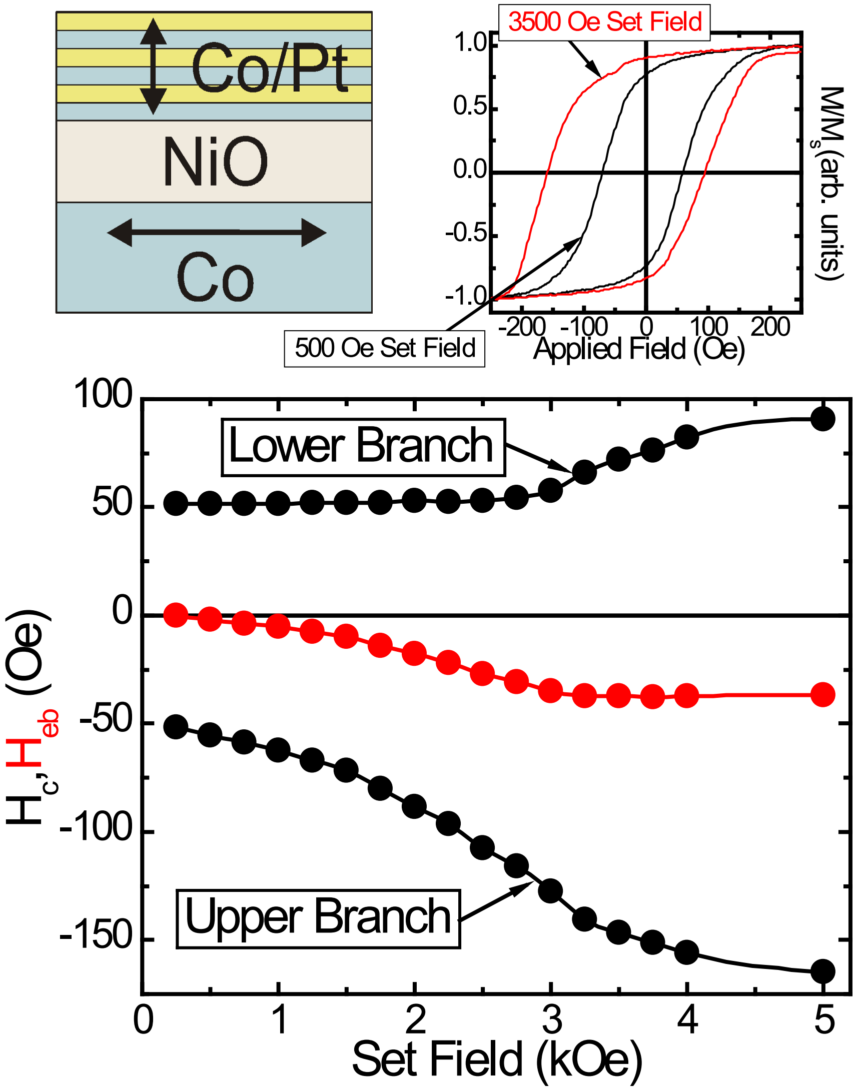

Figure 6.3:

In-plane exchange bias of the Co/NiO/[Co/Pt] heterostructure as a function of H_{set}, where the structure is indicated in the upper left inset. The H_c for the upper and lower branch is also given; notice the lower branch shows no change until 2.75 kOe, above which the upper and lower branches show equal but opposite changes. Two representative loops taken at different H_{set} are shown in the upper right inset.

Temperature dependent measurements were taken on sample A after in-plane ac demagnetization from 3.5 kOe, which minimizes the [Co/Pt] in-plane magnetization. Prior to cooling, a small 250 Oe in-plane field is applied to saturate the in-plane Co layer; the application of this field may result in a very small in-plane remanence of the [Co/Pt] layer (<10% of the saturation magnetization). After cooling in zero-field, the ±250 Oe in-plane magnetization measurements as a function of temperature are shown in Figure 6.4. At each temperature, the sample underwent more than twenty ±250 Oe magnetic field cycles, ensuring that any training effects (resulting in a decrease in LS with repeated magnetic field cycles) for subsequent loops are negligible. Following these initial loops, 10 subsequent loops were taken and averaged together; representative loops for 3 temperatures (150 K, 225 K, 300 K) are displayed in the inset to Figure 6.4. A LS is apparent below a temperature of 225 K and the LS increases linearly with decreasing temperature. The result is consistent with the previously observed linear dependence of EB with temperature below T_B [6.10,6.11,6.15-6.18]. This value of T_B for NiO is vastly greater than other published values of less than 50 K [6.10,6.11] for in plane FM/NiO heterostructures and very closely resembles the linear temperature dependence of LS expected for an AFM with cubic anisotropy and a $(1-T/T_N)^2$ temperature dependence of the anisotropy constant [6.19-6.22]. Note that the strong temperature dependence below T_B rules out magnetostatic coupling effects; due to the high Curie temperatures of the FM layers, the magnetization remains almost constant over the temperature range studied.

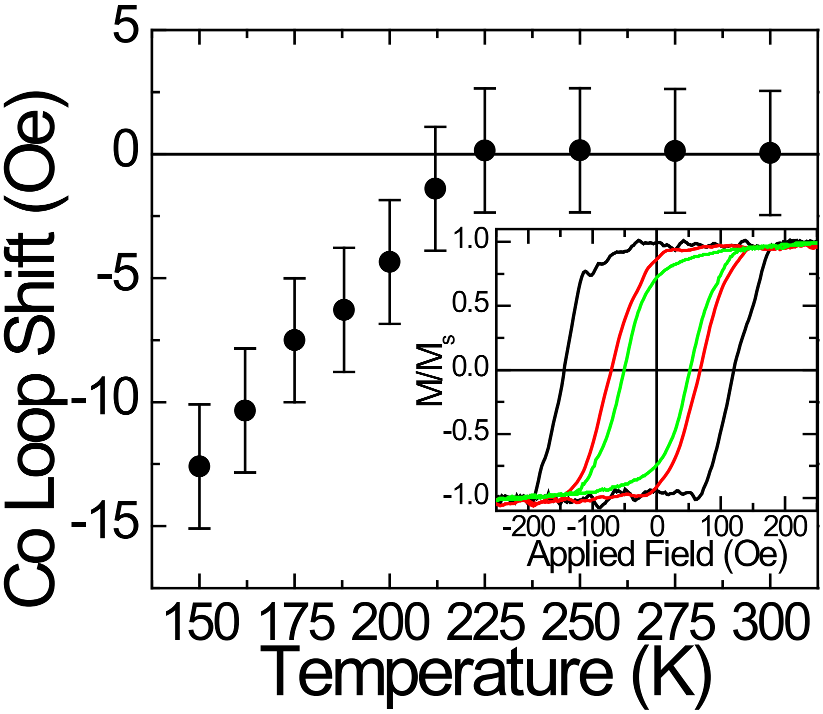

Figure 6.4:

Co loop shift as a function of temperature. The loop shift decreases linearly with temperature, with a T_B of 225 K. The inset shows the hysteresis loop at three representative temperatures (150 - black, 225 - red, 300 K - green)

6.4 Discussion

The in-plane magnetization of the [Co/Pt] layer clearly has a large effect on the in-plane hysteresis loop of the Co layer in these heterostructures. For an 11Å thickness of NiO, the Néel temperature is expected to be below room temperature (RT) [6.23]. However, neutron scattering studies show that the AFM ordering can be stabilized by the presence of an adjacent FM or ferrimagnet [6.18,6.24]. Previous measurements on NiO films of similar thickness sandwiched between [Co/Pt] multilayers [6.13] indicate that the

NiO is AFM ordered well above RT. Following the model of Stiles and McMichael [6.25], we envisage the role of the [Co/Pt] as stabilizing the winding up of domain walls (DW) in the thin AFM NiO during the Co layer's magnetization reversal. In the absence of such stabilization, the partial DW in such a thin film will unwind from the back surface, destroying any possible LS. With only 4 monolayers of NiO, the concept of a DW may seem inadequate; however, the role of the [Co/Pt] magnetization is simply to pin the back surface of the NiO such that the unwinding process does not easily occur. Moreover, since the [Co/Pt] magnetization direction varies with applied fields, the direction of pinning and subsequently the energy stored in the wound up DW can be externally controlled with modest applied fields. The data of Figure 6.3 detailing the dependence of the EB field on the magnetic remanence of the out-of-plane [Co/Pt] layer and the temperature dependence of the EB presented in Figure 6.4 both depend on the presence of the [Co/Pt] layer, albeit in differing ways. The role of NiO in this structure is fundamentally different above and below T_B leading to two distinct mechanisms.

Above T_B, but below T_N, the majority of NiO grains will rotate with the adjacent Co magnetization, contributing to an H_c enhancement. The dragging of AFM grains with the FM magnetization is responsible for the enhanced H_c in EB systems and has been shown to be ubiquitous in bilayer EB systems [6.26, 6.27] and is present well above T_B [6.28]. The differing H_c for the upper and lower curves of the hysteresis loop (i.e. LS) is proposed to occur due to the asymmetry in the [Co/Pt] in-plane magnetization. Soft NiO grains with high coupling strengths will rotate with the respective magnetizations leading to small increases in H_c at low H_{set}. The asymmetry in H_c for the upper and lower curves is due to the NiO layer in contact with the [Co/Pt] layer rotating through a much larger angle on the upper branch than on the lower branch of the hysteresis loop. As the applied field changes from +250 Oe to -250 Oe in the upper curve, the [Co/Pt] layer undergoes a highly asymmetric change in the magnetization angle (see Figure 6.2). As H_{set} increases, this asymmetry increases. Coupling at the [Co/Pt]/NiO interface implies a similarly asymmetric change in the Ni spins at this interface which may be propagated into the rest of the NiO layer. In the lower curve, the very small changes in H_c with increasing H_{set} reflect the small change in angle in both the [Co/Pt] magnetization and hence the corresponding NiO orientation.

For set fields above 3 kOe there is no increase in the asymmetry of the [Co/Pt] loop, as the full [Co/Pt] loop is closed; this is responsible for the saturation of the Co LS seen in Figure 6.3. Above this saturating H_{set} the symmetrical increase in H_c for both the upper and lower curves (Figure 6.3) is attributed to the further rearrangement of the NiO grains. At these larger H_{set} values, the [Co/Pt] magnetization has a larger in-plane component leading to an increase in coupling energy with the NiO layer. This increased coupling at the [Co/Pt]/NiO interface will increase the alignment of NiO grains along the H_{set} direction, increasing the effective coupling at the Co/NiO interface. In this scenario, harder NiO grains will be dragged symmetrically during Co magnetization reversal leading to a symmetric increase in H_c. This symmetric H_c increase will continue until the [Co/Pt] layer saturates in-plane.

Below the observed T_B of 225K, the LS is no longer due to an asymmetry in the [Co/Pt] magnetization, since the applied fields are now symmetric (±250 Oe) in this study. The perpendicular anisotropy of [Co/Pt] has been shown to remain constant with temperature below RT [6.29], so in the ±250 Oe loops at lower temperatures there will be no asymmetry in the [Co/Pt] in-plane magnetization. Instead, the LS occurs due to a balance between the coupling at each interface and the AFM DW energy within a NiO grain. Each NiO grain differs in volume (and hence anisotropy energy), coupling strength (to both the in-plane Co and out of plane [Co/Pt]) and in-plane orientation. The following have been assumed (i) an even number of AFM layers and (ii) AFM coupling at the NiO/[Co/Pt] interface and FM coupling at the Co/NiO interface. Although there is certainly atomic level roughness, the average values of the thickness (as measured by an *in-situ* quartz monitor) is 11Å leading to a preponderance of grains with 4 monolayers of NiO. The assumed sign of coupling at either interface is based on previous XMCD studies, which indicate a Ni terminated Co/NiO interface and an oxygen terminated NiO/[Co/Pt] interface leading to opposite signs of coupling [6.13]. As in the Stiles and McMichael paper, we define $\hat{\mathbf{M}}_{\mathbf{FM}}$, $\hat{\mathbf{u}}$ and $\hat{\mathbf{m}}(\mathbf{0})$ as the directions of the FM magnetization of the in-plane Co layer, the direction of the AFM NiO layer furthest from the FM layer and the direction of the AFM NiO layer closest to the FM Co, respectively [6.25]. For simplicity, both the Co and [Co/Pt] layers are assumed to be in a single domain state and can be described as a macrospin coupled to an ensemble of NiO grains.

The direction of $\hat{\mathbf{u}}$ in this heterostructure is controlled by the magnetization direction of the [Co/Pt], the strength of the coupling at the [Co/Pt]/NiO interface and the anisotropy constants of NiO (including the AFM ordering parameter). For NiO, the anisotropy constant for in-plane rotation (within the (111) plane) is suggested to be ~5% of the out-of plane rotation (perpendicular to the (111) plane), $K_1=3.32\text{x}10^6$ erg/cm^3 [6.10,6.12]. These widely differing values of anisotropy lead to significantly different T_B for in-plane vs. out-of plane EB. Experiments on in-plane Ni/NiO(28Å) [6.11] indicate a

T_B of 34K whereas experiments on [Co/Pt]/NiO(11Å) bilayers and trilayers with perpendicular anisotropy indicate a T_B above 200K [6.19,6.20]. These T_B values correspond to the thermal energies needed to switch a particular AFM grain, corresponding to K_1V (K_2V) in the case of out-of plane (in-plane) rotations, where V is the volume of a grain. Above the cited T_B, all AFM grains are thermally switched in a particular anisotropy direction.

The initial 250 Oe in-plane field at RT to saturate the Co layer will have the effect of inducing a small in-plane remanent magnetization in the [Co/Pt] layer resulting in a magnetization direction that is ~5° from the normal. This direction of magnetization together with the coupling will define the vector $\hat{\mathbf{u}}$, where $\hat{\mathbf{u}}$ may cant out of and rotate within the (111) plane. Rotation within the (111) plane is governed by the magnitude of K_2, whereas canting out of this plane is governed by the magnitude of K_1. Although $K_2 << K_1$, XMCD measurements [6.13] have shown that the NiO spins do cant out-of-plane at [Co/Pt]/NiO interfaces. Thus, $\hat{\mathbf{u}}$ is expected to have an out-of-plane component during the cooling procedure and lie within the plane defined by $\hat{\mathbf{M}}_{\mathbf{FM}}$ and the [Co/Pt] magnetization. At the opposite interface, the direction of $\hat{\mathbf{m}}(\mathbf{0})$ is dictated by the direction of $\hat{\mathbf{M}}_{\mathbf{FM}}$, the interfacial coupling, the anisotropy constants of NiO (particularly K_2) and, most importantly, the strength of the AFM ordering.

Below 225 K the following constraints hold (i) energy minimization requires that all the NiO spins lie in the plane $\vec{\mathbf{A}}$ defined by the magnetization of the in-plane Co layer, $\hat{\mathbf{M}}_{\mathbf{FM}}$, and the pinned NiO layer, $\hat{\mathbf{u}}$ [6.25] (ii) the energy cost associated with overcoming K_1 prevents the NiO spins from further canting out of the (111) plane; however, at these temperatures spin rotation within the plane is energetically allowed and

(iii) the NiO layers adjacent to the Co and [Co/Pt] layers are coupled to their respective FM layers. Based on these three constraints on the NiO spins we envisage $\hat{\mathbf{u}}$ rotating only slightly within the NiO (111) plane during the magnetization reversal of both the Co and [Co/Pt]. It is energetically unfavorable for $\hat{\mathbf{u}}$ to completely track along with the [Co/Pt] magnetization; when the [Co/Pt] reverses, it does so by passing through a vector perpendicular to the NiO (111) plane. For $\hat{\mathbf{u}}$ to track the [Co/Pt] magnetization along this path, it must overcome the K_1 anisotropy. Instead $\hat{\mathbf{u}}$ will attempt to switch via rotation within the NiO (111) plane; however, this mode will only allow for relatively small rotations due to constraints (i) and (ii). Allowing $\hat{\mathbf{u}}$ to rotate in the NiO (111) plane a small amount minimizes the energy cost associated with overcoming the AFM ordering but also satisfies the 3 constraints. In this scenario, $\hat{\mathbf{u}}$ is sufficiently pinned to produce a DW in the NiO layers resulting in slightly differing energies for positive and negative Co saturation, leading to very small LS values. The measured LS are orders of magnitude smaller than those seen for perpendicular [Co/Pt]/NiO EB measurements. As the temperature decreases below 225K, the anisotropy constants increase leading to the observed linear temperature dependence of LS.

There are numerous configurations of NiO spins that may occur within the constraints given to produce the observed LS. To experimentally observe the specific configuration will require depth profiling measurements of the local magnetization in the NiO layer, similar to the recent investigation of a [CoO/NiO] multilayer in contact with a Pt-Co layer [6.30].

6.5 Conclusion

An isothermally tunable LS has been demonstrated for a Co/NiO/[Co/Pt] heterostructure with an 11Å thick NiO interlayer. This heterostructure exhibits a LS along the field axis and H_c enhancement at RT. The addition of the [Co/Pt] multilayer allows dynamic control of the NiO AFM structure by way of stabilization due to the exchange interaction at the NiO/[Co/Pt] interface. Variation of the in-plane component of magnetization in the [Co/Pt] multilayer leads to changes in the NiO, which in turn lead to a change in the H_c of the Co layer. This H_c change is asymmetric for the upper and lower curves of the hysteresis loop due to an asymmetry in the [Co/Pt] magnetization leading to a tunable LS. The addition of the [Co/Pt] layer also greatly enhances T_B of this structure by adding an additional constraint to the NiO layer during Co magnetization reversal. Such isothermal control of the LS at RT and the greatly enhanced T_B is useful in a variety of modern approaches to spintronic applications.

6.6 Acknowledgements

This work was supported by NSF MRSEC DMR-0213808 and 0820521.

6.7 References

6.1. W.H. Meiklejohn and C.P. Bean, Phys. Rev. **105**, 904 (1957).

6.2. Gary A. Prinz, Science **282**, 1660 (1998).

6.3. S. A. Wolf, D. D. Awschalom, R. A. Buhrman, J. M. Daughton, S. von Molnár, M. L. Roukes, A. Y. Chtchelkanova, and D. M. Treger, Science **294**, 1488 (2001).

6.4. J. Nogués, D. Lederman, T. J. Moran, and Ivan K. Schuller, Phys. Rev. Lett. **76**, 4624 (1996).

6.5. P. Miltényi, M. Gierlings, M. Bamming, U. May, G. Güntherodt, J. Nogués, M. Gruyters, C. Leighton, and Ivan K. Schuller, Appl. Phys. Lett. **75**, 2304 (1999).

6.6. N. J. Gökemeijer, J. W. Cai, and C. L. Chien, Phys. Rev. B **60**, 3033 (1999).

6.7. J. Nogués, J. Sort, S. Suriñach, J. S. Muñoz, M. D. Baró, J. F. Bobo, and U. Lüders, Appl. Phys. Lett. **82**, 3044 (2003).

6.8. A. Bollero, L. D. Buda-Prejbeanu, V. Baltz, J. Sort, B. Rodmacq, and B. Dieny, Phys. Rev. B **73**, 144407 (2006).

6.9. S. Sahoo, T. Mukherjee, K. D. Belashchenko, and Ch. Binek, Appl. Phys. Lett. **91**, 172506 (2007).

6.10. K. Takano, Ph.D. thesis, Physics Department, University of California at San Diego, San Diego, CA (1998).

6.11. M Gruyters, J. Magn. Magn. Mater. 248, 248 (2002).

6.12. M. T. Hutchings and E. J. Samuelsen, Phys. Rev. B **6**, 3447 (1972).

6.13. A. Baruth, D. J. Keavney, J. D. Burton, K. Janicka, E. Y. Tsymbal, L. Yuan, S. H. Liou, and S. Adenwalla, Phys. Rev. B **74**, 054419 (2006).

6.14. Note that the observed loop shift cannot be a result of the simple addition of the two hysteresis loops of the constituent layers (Co/Pt and Co) since the Co layer's contribution to the magnetization is nearly 10 times larger in the region of interest. Moreover, if indeed the [Co/Pt] layer were contributing significantly to the in-plane hysteresis loop, we should see a significant shift of the loop along the vertical magnetization axis, whereas the loop is symmetrical in ±M.

6.15. M. J. Carey and A. E. Berkowitz, J. Appl. Phys. **73**, 6892 (1993).

6.16. M. J. Carey and A. E. Berkowitz, Appl. Phys. Lett. **60**, 3060 (1992).

6.17. V. Strom, B.J. Jonsson, K.V. Rao, and D. Dahlberg, J. Appl. Phys. **81**, 5003 (1997).

6.18. P.J. van der Zaag, Y. Ijiri, J.A. Borchers, L.F. Feiner, R.M. Wolf, J.M. Gaines, R.W. Erwin, and M.A. Verheijen, Phys. Rev. Lett. **84**, 6102 (2000).

6.19. Z. Y. Liu and S. Adenwalla, Phys. Rev. Lett. **91**, 037207 (2003).

6.20. Z. Y. Liu and S. Adenwalla, J. Appl. Phys. **94**, 1105 (2003).

6.21. A. P. Malozemoff, J. Appl. Phys. **63**, 3874 (1988).

6.22. A. P. Malozemoff, Phys. Rev. B **35**, 3679 (1987).

6.23. D. Alders, L. H. Tjeng, F. C. Voogt, T. Hibma, G. A. Sawatzky, C. T. Chen, J. Vogel, M. Sacchi, and S. Iacobucci, Phys. Rev. B **57**, 11623 (1998).

6.24. J. A. Borchers, R. W. Erwin, S. D. Berry, D. M. Lind, J. F. Ankner, E. Lochner, K. A. Shaw, and D. Hilton, Phys. Rev. B **51**, 8276 (1995).

6.25. M. D. Stiles and R. D. McMichael, Phys. Rev. B **59**, 3722 (1999).

6.26. M. D. Stiles and R. D. McMichael, Phys. Rev. B **63**, 064405 (2001).

6.27. G. Scholten, K. D. Usadel, and U. Nowak, Phys. Rev. B **71**, 064413 (2005).

6.28. K. Lenz, S. Zander, and W. Kuch, Phys. Rev. Lett. **98**, 237201 (2007).

6.29. H.Y. Zhang, Y.J. Wang, G.G. Zheng, J.X. Shen, Z.S. Shan and D.J. Sellmyer, IEEE Trans. Magn. **29**, 3376 (1993).

6.30. J. M. Tonnerre, M. De Santis, S. Grenier, H. C. N. Tolentino, V. Langlais, E. Bontempi, M. García-Fernández, and U. Staub, Phys. Rev. Lett. **100**, 157202 (2008).

This chapter is based on the published paper: *Enhanced blocking temperature and isothermal control of hysteresis loop shifts in Co/NiO/[Co/Pt] heterostructures with orthogonal easy axes,* A. Baruth and S. Adenwalla, Phys. Rev. B **78**, 174407 (2008).

Chapter 7

Temperature and set field dependence of exchange bias training effects in Co/NiO/[Co/Pt] heterostructures with orthogonal easy axes

7.1 Introduction

Interfacial coupling at the interface between a ferromagnet (FM)/antiferromagnet (AFM) leads to a symmetry breaking and a subsequent shift of the hysteresis loop (the exchange bias), among other phenomena. Although discovered over 50 years ago [7.7.1], exchange bias continues to pose intriguing questions [7.7.2], one of which is the training effect, in which the exchange bias field is progressively reduced on repeated magnetic field cycling [7.2,7.3]. Exchange bias has important technological application in magnetic memory devices [7.4-7.6] and a clear understanding of the training effect could lead to technological advances by increasing the magnitude of the loop shift. Exchange bias has been successfully modeled by allowing for the formation of multiple domains, usually within the AFM. A net interfacial magnetization within the AFM, S_{AFM}, exchange couples to the FM. The training effect is then commonly ascribed to the rearrangement of these domains towards equilibrium on repeated field cycling, thereby altering S_{AFM}. Numerous models based on experimental observations of the training effect have been proposed [7.7-7.13]. Much of the data on the training effect fit a $1/\sqrt{n}$ dependence [7.2,7.14-7.17], although an understanding of this dependence has been lacking. The addition of non-magnetic impurities to the AFM [7.18] leads to an increase in the exchange bias, and has been ascribed to the lower energy cost associated with the formation of a domain wall that passes through a non magnetic impurity. Monte Carlo modeling of the interface magnetization of these diluted AFM films displays hysteretic behavior where the hysteresis loop does not close at positive saturation [7.18], implying a decrease in interfacial magnetization with subsequent loops leading to a decrease in loop shift. This effect has also been studied extensively by C. Binek in the framework of non-equilibrium thermodynamics, where consecutive magnetization cycles rearrange the interface spins of the AFM towards equilibrium [7.11]. This more contemporary approach gives better insight and predictive power into the temperature dependence [7.19] of the training effect as well as a physical basis for the phenomenological $1/\sqrt{n}$ dependence.

In this chapter the training effect in a new class of exchange biased magnetic heterostructures, consisting of two AFM/FM interfaces in a Co/NiO(11Å)/$[\mathrm{Co/Pt}]_3$ stack, is measured and modeled. Previous experiments [7.20] have demonstrated an enhanced blocking temperature as well as the ability to isothermally field tune the magnitude of the in-plane loop shift, at temperatures well below the Néel temperature of the AFM. Both effects are large; the observed blocking temperature of 225K is well above the 40K or less expected for the in-plane loop shift with a similar thickness of NiO [7.21,7.22] and the isothermal field tuning shows room temperature changes of 35 Oe in the loop shift on application of a 3 kOe in-plane set field. Both effects have been attributed to the $[\mathrm{Co/Pt}]_3$ layer with perpendicular anisotropy. The exchange interaction at the NiO/$[\mathrm{Co/Pt}]_3$ interface pins the NiO domains, thereby increasing the energy cost associated with reversal of the AFM domains [7.20]. The effects seen in this trilayer sample are quite distinct from those seen in a Co/FeMn/CuNi stack [7.23], in which the presence of the Co underlayer effectively eliminates exchange bias effects at the CuNi/FeMn interface. However, their approach to probing the AFM layer with a low T_c ferromagnet gives insight into the formation of exchange bias in a variety of systems, including our trilayer structure.

7.2 Experimental Techniques

Two samples were prepared by dc and rf magnetron sputtering from separate Pt, Co, NiO and Cu targets on naturally oxidized Si substrates deposited in 2 mTorr Ar pressure with a base pressure of $\sim 3 \times 10^{-8}$ Torr and consisted of

Sample A: Si<111>/Pt(200Å)/ NiO(10Å)/[Pt(6Å)/Co(4Å)]$_3$/Cu(100Å)

Sample B: Si<111>/Pt(200Å)/Co(40Å)/NiO(10Å)/[Pt(6Å)/Co(4Å)]$_3$/Cu(100Å) [7.24].

The 40Å Co layer and the [Co/Pt]$_3$ multilayer stack display the expected in-plane and out-of-plane magnetic easy axes, respectively. The NiO is polycrystalline but strongly (111) textured. The thickness calibration and structural characterization are discussed elsewhere [7.20]. Room temperature magnetic characterization of samples was done using alternating gradient field magnetometry (AGFM), while temperature dependent measurements were made using the magneto-optic Kerr effect (MOKE) in a Janis cryostat with polarization preserving optical windows.

The isothermally field tunable loop shifts previously measured on sample B [7.20] were confined to the first loop performed after application of an in-plane set field.

Subsequent magnetization loops displayed a progressive reduction in the loop shift, the subject of this chapter. The blocking temperature of 225K was measured at equilibrium after repeated (n>20) field cycling. Above this blocking temperature, in-plane Co layer loop shifts were observed *only* when the [Co/Pt] multilayer acquired a non-zero in-plane magnetization and the magnitude of the Co loop shift was directly proportional to this in-plane remanence. In the previous chapter it was argued that the effect of the [Co/Pt] layer is to alter the configuration of domains in the NiO layer. Hence these heterostructures are ideal for investigations of the training effect, providing a precise method by which to control the configuration of AFM domains with application of fairly modest fields on a single sample. The role of the [Co/Pt] layer is to variably pin AFM domains, similar to previous measurements of the effects of dilution in the AFM layer [7.25], albeit on a single sample, allowing the discounting of variations in interface roughness, crystallinity, coupling constants, all of which have an effect on the magnitude of both the training effect and the exchange bias field. Also in contrast to the dilution experiments, the magnetization direction of the $[Co/Pt]_3$ stack will control only the interfacial NiO layer, rather than altering the volume of the AFM.

In order to understand the *quantitative* effects of the $[Co/Pt]_3$/NiO interface on the entire heterostructure, room temperature, minor in-plane hysteresis loop measurements performed on sample A consisting of NiO(11A)/$[Co/Pt]_3$ are shown in figure 7.1a. Prior to this measurement an in-plane field, the so called H_{set} of +3.5 kOe is applied, and the hysteresis loop is subsequently cycled between ±250 Oe. (A $H_{set} = 3\,kOe$ would be sufficient to close the magnetization loop; however, we routinely applied $H_{set} = 3.5\,kOe$ to ensure full closure.) The asymmetry in the first loop is due to the field asymmetry in the positive and negative directions, since for this initial loop the field cycles between H_{set} (in this case 3.5 kOe) and -250 Oe. Subsequent magnetization loops cycling between ±250 Oe (which corresponds to the field at which the Co layer in sample B is fully saturated) show minute changes, corresponding to a change in the upper (lower) loop remanence of ~0.1% (~0.05%) relative to saturation. Such minute changes correspond to less than a ~0.1% change in the magnetization angle of the [Co/Pt]; hence training effects in the entire heterostructure (sample B) must primarily be due to the interaction between the in-plane Co and the NiO layer. The positive in-plane remanence for both the upper and lower curves of the hysteresis loops (figure 7.1a) implies that the [Co/Pt] layer will retain a net in-plane magnetization along the positive H_{set} direction, even after repeated switching of the in-plane Co. The value of this positive remanence is dependent on the magnitude of H_{set} as shown in figure 7.1b, which shows the average of the remanence values (M_R) on the upper and lower branches of the hysteresis loop as a function of H_{set}. Increasing the in-plane remanence of the [Co/Pt] magnetization results in a proportional increase of in-plane pinning of NiO AFM domains. At fields above 3.5 kOe, the in-plane remanence saturates because the major in-plane hysteresis loop of sample A closes (and saturates at 5 kOe). Subsequent analysis of the training data will demonstrate that the in-plane remanence has a marked effect on both the equilibrium exchange bias field and on the blocking temperature.

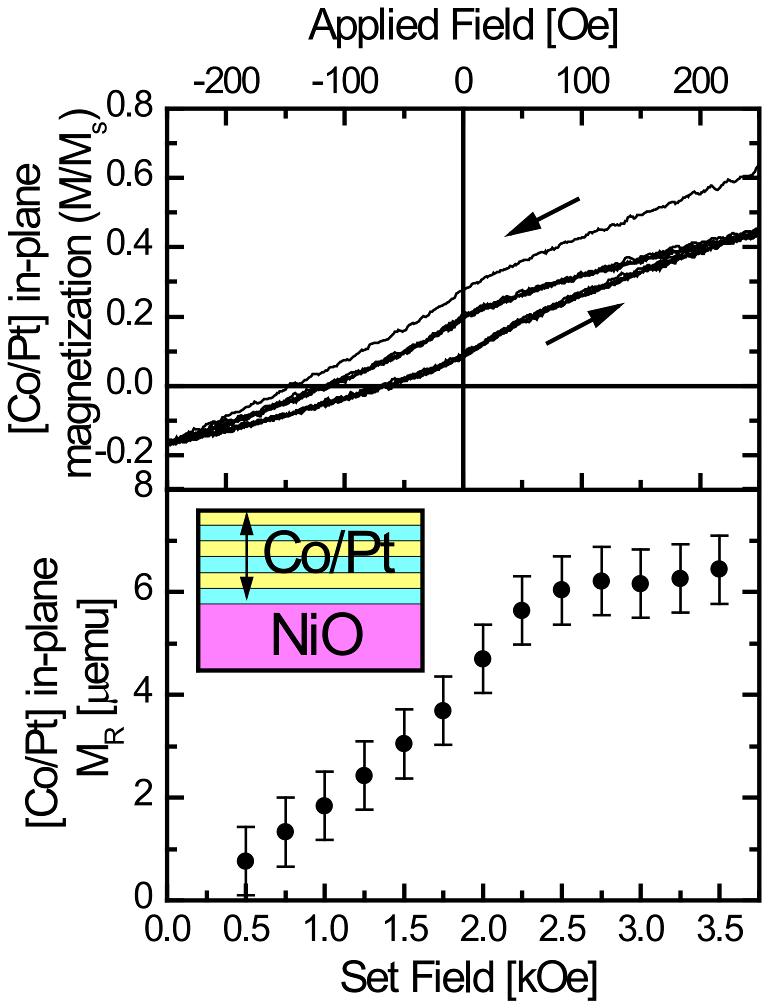

Figure 7.1:

(a) A series of ten 250 Oe in-plane magnetization loops of sample A following the application of a 3.5 kOe in-plane set field. Following the initial loop, the [Co/Pt] magnetization displays negligible training effects. (b) Average [Co/Pt] in-plane remanance, M_R, as a function of the set field, H_{set}. M_R increases with increasing H_{set}, saturating at $H_{set} \cong 2.75\,\mathrm{kOe}$. The sample schematic is given in the inset.

7.3 Measurements of the Training Effect

To test for training effects in sample B, an in-plane set field (H_{set}) is always applied at room temperature. To study the effects of H_{set}, loops are measured at room temperature by varying H_{set} and subsequently cycling between ±250 Oe. Temperature dependence effects are measured after applying H_{set} at room temperature, cooling (or heating) to a given temperature (in zero applied field) and then performing in-plane magnetization measurements between ±250 Oe. Note that these are minor hysteresis loops of the full heterostructure, corresponding only to the magnetization reversal of the in-plane Co layer. The upper (lower) branch of these minor hysteresis loops corresponds to the curves starting from positive (negative) field. The first loop is an anomaly, since this loop is measured in extremely asymmetric fields, cycling from H_{set} to -250 Oe and back again to +250 Oe. Related to this is the anomalously large value of the in-plane remanence of the $[Co/Pt]_3$ layer on the first loop, resulting in an anomalously high value of the exchange bias. This is not due to training effects, rather, to the strong pinning from the $[Co/Pt]_3$. Henceforth, this initial loop is ignored, and the counter is reset to start at $n=1$ *after* this initial loop. The asymmetry (increasing with H_{set}) in the [Co/Pt] magnetization on the upper and lower branches is transferred to the NiO grains at the [Co/Pt]/NiO interface and results, via the AFM coupling within the NiO, in differing coercivity for the upper and lower branches of the Co hysteresis loop, leading to the observed loop shift.

Room temperature, in-plane hysteresis loop shifts for sample B are shown in figure 7.2 for a variety of in-plane set fields from 250 Oe to 3 kOe (no changes in training occur above 3 kOe due to the saturation of the $[Co/Pt]_3$ in-plane remanence) and indicate

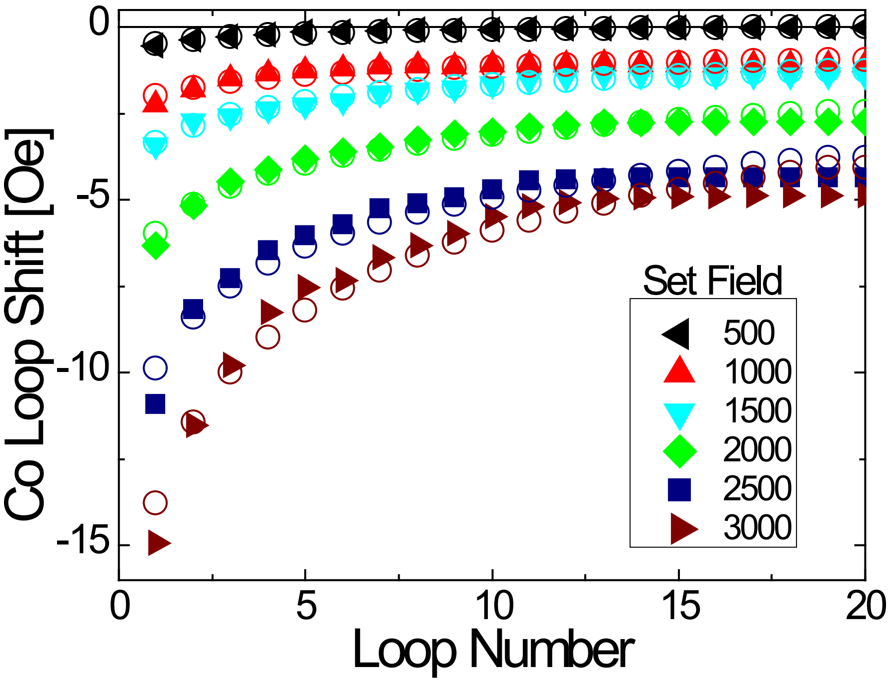

Figure 7.2:

Room temperature training data as a function of set field, H_{set}. The solid symbols represent the Co layer loop shift as a function of loop iteration number. Each colored series represents the corresponding H_{set} before the training data was taken. For $H_{set} \geq 3\,\mathrm{kOe}$, the data are identical for all set fields. The open circles represent the best fit using the L-K theory, described in the text.

the presence of significant training. Beyond n=20, there are no measurable changes in the loops; the system has reached equilibrium. Data for the n=1 and 20 loops are shown as functions of H_{set} in figure 7.3. Above an H_{set} of ~600-700 Oe, a loop shift persists, even after repeated cycling, which must occur due to the presence of irreversible NiO grains aligned along the remanent in-plane magnetization of the [Co/Pt]. The differing coercivity for the upper and lower loops, which leads to the observed loop shift, arise from the in-plane remanent magnetization of the [Co/Pt] layer and its interaction with the

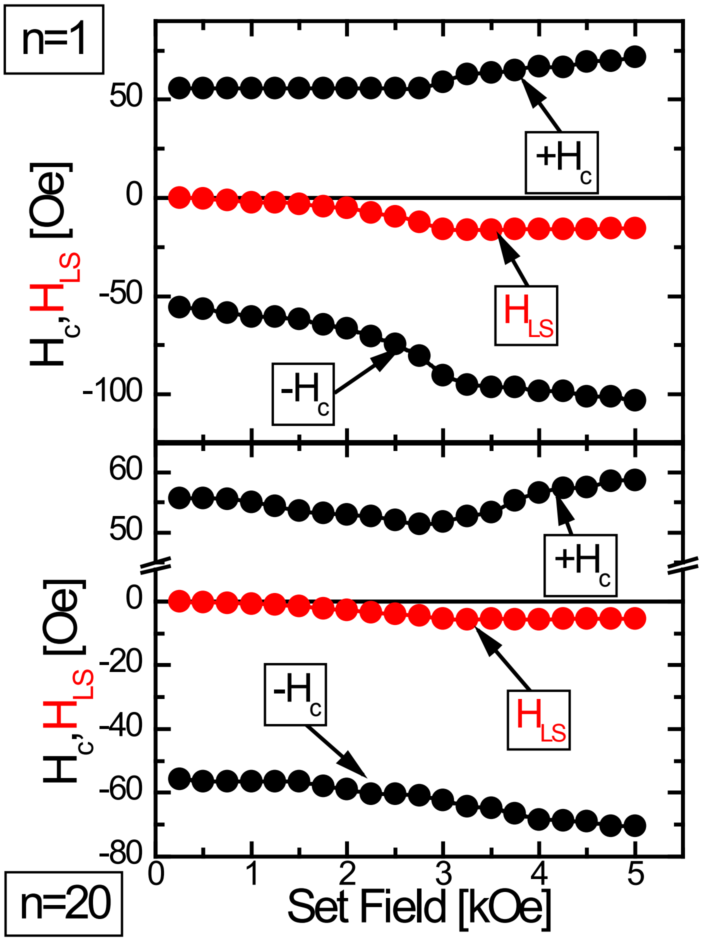

Figure 7.3:

The effect of the set field, H_{set}, on the upper and lower branch coercivities and the loop shift for the initial n=1 (top panel) and the final n=20 (bottom panel) hysteresis loops. For both series, a loop shift is observed that increases with increasing set field until 3 kOe, above which it remains constant. Note that both coercivities continue to increase above $H_{set} = 3\,\mathrm{kOe}$.

NiO, as outlined above and in ref. 7.20. Since this remanence remains unchanged after the initial loop, (see figure 7.1a), the training effects observed between loops 1 and 20 arise solely from the interactions at the Co/NiO interface. The biggest difference between the n=1 and n=20 data, other than the magnitude of the loop shift, is the coercivity of the lower branch as a function of H_{set}. Notice that for n=1, the coercivity remains nearly constant until ~3 kOe, where it rises in conjunction with the upper loop. In contrast, for the n=20 data, the coercivity actually drops with H_{set} until ~3 kOe, where it again rises in conjunction with the upper loop. This is indicative of hard NiO grains that are fixed along the H_{set} direction, that are not affected by the sweeping magnetic field or [Co/Pt] in-plane magnetization loops. The softer grains are completely trained to equilibrium by n=20. Above the saturating H_{set} the symmetrical increase in H_c for both the upper and lower curves (figure 7.3) is attributed to the further rearrangement of the NiO grains. At H_{set} values above this saturating value, the large in-plane component of [Co/Pt] magnetization leads to an increase in coupling energy with the NiO layer. This increased coupling at the [Co/Pt]/NiO interface will increase the alignment of NiO grains along the H_{set} direction, increasing the effective coupling at the Co/NiO interface. In this scenario, harder NiO grains will be dragged symmetrically during Co magnetization reversal leading to a symmetric increase in H_c, which continues until the [Co/Pt] layer saturates in-plane (~5 kOe).

The blocking temperature of 225 K, measured earlier [7.20], corresponds to a minimal $H_{set} = 250\ \mathrm{Oe}$. Larger set fields lead to loop shifts at higher temperatures (*i.e.* higher blocking temperatures), up to a maximum $H_{set} = 3.5\ k\mathrm{Oe}$, thereby expanding the range of temperatures that can be studied. In order to investigate the temperature dependence of training, an in-plane $H_{set} = 3.5\ k\text{Oe}$ is applied at room temperature, after which the sample is heated or cooled to the desired temperature in 25K increments over a range from 175-375K. This value of H_{set} represents the maximum value of in-plane magnetic remanence attainable for the [Co/Pt] stack, and hence sets the scale for the highest achievable loop shift. Ten consecutive in-plane magnetization measurements are taken between ±250 Oe and the resulting loop shifts measured. To improve statistics, this procedure is repeated three times at each temperature and averaged. Representative loop shift data for the entire range of temperatures is shown in figure 7.4. Both the loop shift and the magnitude of the training increase with decreasing temperature. At 375K, the equilibrium values for the loop shift ($n \geq 10$) approach zero.

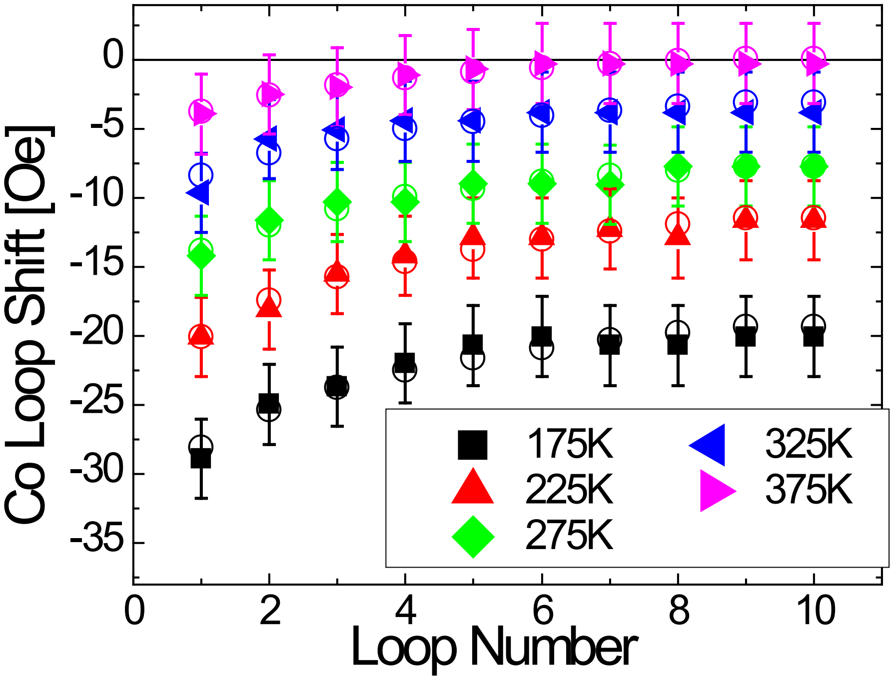

Figure 7.4:

The training effect as a function of temperature. All data were taken after application of an in-plane $H_{set} = 3.5\,\mathrm{kOe}$ at room temperature. The solid symbols correspond to the Co layer loop shift as a function of loop iteration number. Each colored series represents the temperature at which the training data was obtained. The open circles represent the best fit using the L-K theory, described in the text.

The training effect in exchange bias-like systems is dominated by the dynamics of the AFM interfacial layer, in particular by the deviation of the surface magnetization from equilibrium due to thermal activation [7.2,7.6,7.11,7.14,7.15,7.25-7.30]. The non-stationary loop shift indicates a NiO interface magnetization that deviates from its equilibrium configuration, with a slow return to equilibrium with consecutive magnetization cycling. Experimentally, in many systems [7.2,7.14-7.17] the deviation of the loop shift from the equilibrium value (for $n > 1$) can successfully be fit to an empirical $[H_{eb}(n) - H_{eb}^{e}] = \kappa/\sqrt{n}$ dependence, where n is the loop iteration number, $H_{eb}(n)$ is the loop shift at n, H_{eb}^{e} is the equilibrium loop shift (after infinite cycles) and κ is a fitting parameter. Unfortunately, this approach lacks predictive power regarding the temperature and H_{set} dependence of the training, as there is little physical intuition as to why this dependence occurs. A non-equilibrium thermodynamic approach by C. Binek [7.19] serves this purpose better. In this approach, any deviation of the AFM spins from their equilibrium configuration results in an increase in the free energy, and the relaxation of the spins towards equilibrium are described by the Landau Khalatnikov (LK) equation. Discretization of the LK equation and mapping the n dependence of the exchange bias field onto the relaxation of the AFM spins leads to

$$[H_{eb}(n+1) - H_{eb}(n)] = -\gamma[H_{eb}(n) - H_{eb}^{e}]^{3}, \tag{7.1}$$

where γ is a physical parameter describing the relaxation process of the NiO interface spins. Large values of γ correspond to rapid attainment of an equilibrium state and/or small deviations from equilibrium. In general, an increasing value of γ implies that the training effect decreases in importance and that repeated cycling will have little or no effect on the loop shift.

Using this approach to fit the data in figures 7.2 and 7.4 makes it possible to obtain values of γ as functions of both temperature and H_{set} ([Co/Pt] in-plane remanance, M_R). The best fits, based on eqn. 7.1, are shown as the open circles in figures 7.2 and 7.4. The free parameters in the fit are H_{eb}^{e}, $H_{eb}(n=1)$ and γ. For the temperature dependent data, H_{eb}^{e} is constrained to be linear with temperature, based on the loop shift versus temperature data from ref 7.20.

The values for the fitting parameter γ, which contains the interface exchange coupling and the damping constant governing the relaxation dynamics of the AFM spin configuration, as functions of both temperature and M_R are plotted in figures 7.5 and 7.6, respectively. The increasing value of γ with increasing temperature implies that at temperatures close to the blocking temperature there are only small deviations from the equilibrium NiO interface magnetization and that equilibrium is attained more rapidly. At some critical temperature, the training no longer persists and γ drops abruptly to zero. The expected temperature dependence of γ is given by [7.19]

$$\gamma(T,T_B)=C\left(\frac{\eta_e(T)\tanh\left[\frac{T_B\eta_e(T)}{T}\right]}{T\left\{T\left(1+\cosh\left[\frac{2T_B\eta_e(T)}{T}\right]\right)-2T_B\right\}}\right)^2 . \tag{7.2}$$

η_e is the equilibrium order parameter of the AFM given by

$$\eta_e(T)\approx\tanh\frac{T_B}{T}\sqrt{3(T_B-T)/T_B}\ , \tag{7.3}$$

C is a constant, *T* is the measurement temperature and T_B is the blocking temperature (defined in this case as the temperature at which the training effect disappears and γ goes to zero). The line in figure 7.5 represents the best fit to the temperature dependence of γ with two free parameters, *C* and T_B. The blocking temperature obtained from this best fit is 389 K, approximately 150 K above the low set field (250 Oe) blocking temperature of 225 K. Clearly, the magnitude of the set field and the corresponding [Co/Pt] in-plane remanence *significantly* enhances the blocking temperature. Moreover, the blocking temperature so obtained is quite compatible with the experimental data (see figure 7.4); at 375 K the training effect is barely discernible.

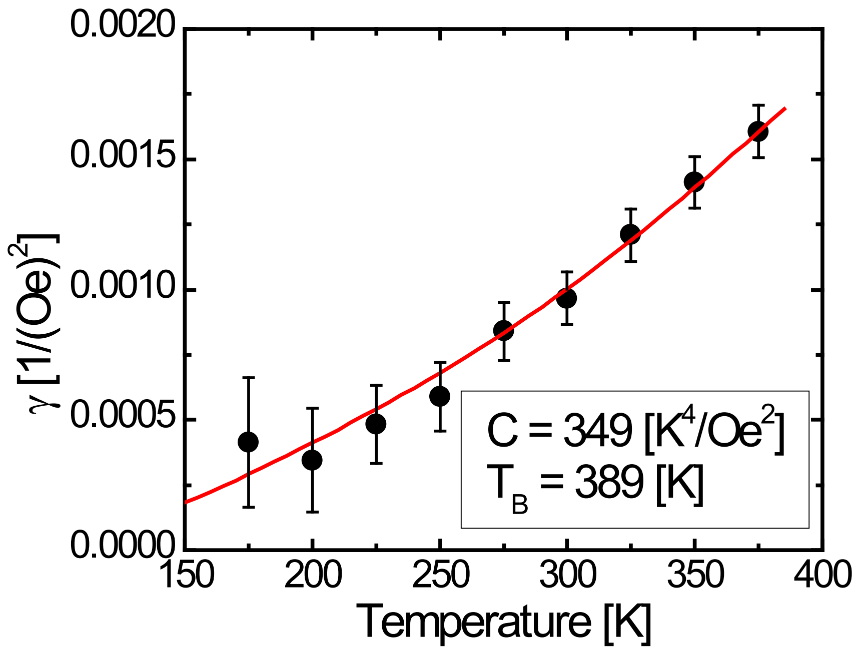

Figure 7.5:

The training effect parameter, γ, as a function of temperature. γ is obtained from fitting eqn. 7.1 to the training data in figure 7.4. The line is a best parameter fit to eqn. 7.2. The fit parameters C and T_B are displayed.

The dependence of γ on M_R, the in-plane remanence of the [Co/Pt], is shown in figure 7.6. For small in-plane remanence (*i.e.* low H_{set}) , the training effect is small (corresponding to a large value of γ); there are only small deviations from the equilibrium NiO interface magnetization and equilibrium is attained rapidly. In contrast, for large set fields the absolute training is larger, but spread out over more cycles. The influence of the [Co/Pt] in-plane remanence on the training parameter γ can be seen quite clearly in the influence of H_{eb}^{e} on M_R, (figure 7.6: inset) $-H_{eb}^{e}$ increases linearly with M_R, with a slope of $k = -0.75\,\mathrm{Oe}/\mu\mathrm{emu}$. To look for effects of M_R that go beyond this H_{eb}^{e} dependence, $4\pi k M_R$ was substituted for H_{eb}^{e} in the expression for γ (eqn. 7.1) and fit

$$\gamma = \frac{A}{\left(B + 4\pi k M_R\right)^3}, \tag{7.4}$$

where A and B are fitting parameters related to $[H_{eb}(n+1) - H_{eb}(n)]$ and $H_{eb}(n)$, respectively. The excellent fit based on eqn. 7.4 is shown in figure 7.6, with an R^2 value of 0.96. It can be concluded from this fit that the sole effect of the [Co/Pt] in-plane remanence, M_R, is to alter the equilibrium loop shift. In the thermodynamic approach described above, this implies that M_R has no effect on the coefficients that relate the change in free energy to the non-equilibrium spin configurations, once again confirming that the training effects are confined to the Co/NiO interface and that the presence of the [Co/Pt] sets only the initial conditions under which the training effects may be measured.

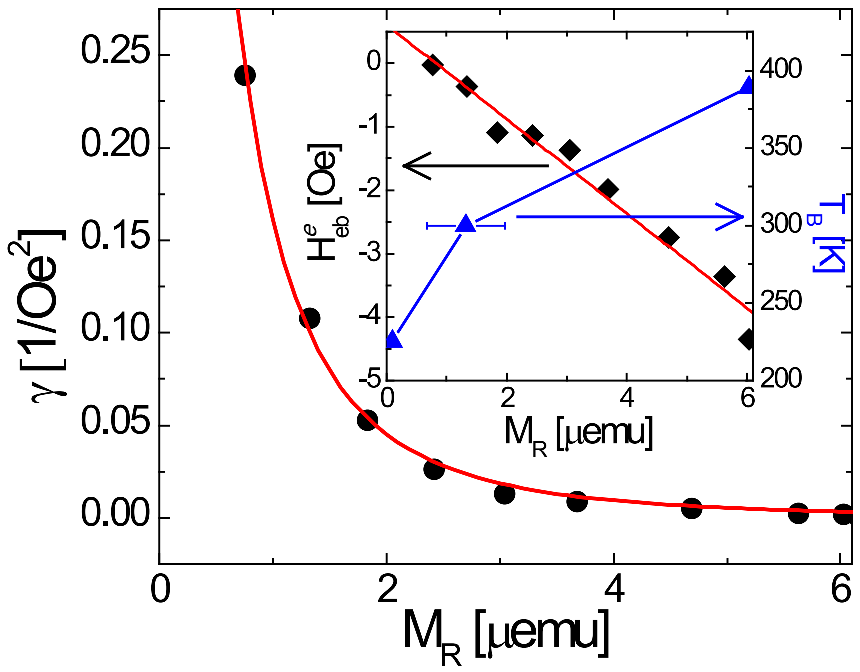

Figure 7.6:

The training effect parameter, γ, vs. [Co/Pt] in-plane remanance, M$_R$. γ is obtained from fitting eqn. 1 to the training data in figure 2. The line represents the best fit to eqn. 4, where fitting parameters are described in the text. **Inset**: The black diamonds indicate the relationship between the equilibrium loop shift, H^e_{eb}, and M$_R$. The red line is the best linear fit to the data, giving a slope of $-0.75\,\mathrm{Oe}/\mu\mathrm{emu}$ with an R^2 value of 0.96. The blue triangles show the relationship between the blocking temperature, T$_B$, and M$_R$. The blue line is a guide to the eye.

The linear relationship between M$_R$ and the equilibrium loop shift (figure 7.6:inset) also implies that the temperature at which H^e_{eb} goes to zero must depend on M$_R$. Increasing the in-plane remanence will increase the coupling energy at the

[Co/Pt]/NiO interface and increase the volume of pinned NiO grains. There are three data points for blocking temperature versus M$_R$: $T_B = 225K$ for $H_{set} = 250$ Oe (previous paper [7.20]), $T_B = 389K$ for $H_{set} = 3.5\ k$Oe (from the calculated value in figure 7.5), and finally $T_B = 300K$ for $H_{set} = \sim 600 - 700$ Oe (based on the n=20 data in figure 7.3). These three points are plotted in the inset to figure 7.6 as a function of the corresponding M$_R$ values (blue triangles). The highest blocking temperature is well above that expected for such a thin NiO film for either in-plane [7.21,7.31] or perpendicular anisotropy [7.32,7.33] and well above the purported Néel temperature of a thin film [7.34]. It may be understood by considering the coupling energy at *both* interfaces. The scenario we envisage is the following. Both the Co and the [Co/Pt]$_3$ are coupled to an array of independent AFM grains with variable volume and net surface magnetization. Simulations in ref. 7.35 describe an effective energy barrier to switching within each AFM grain that depends on the balance between the interface coupling (which lowers the barrier) and the anisotropy energy of the AFM. The distribution of grain sizes and coupling strengths leads to a distribution of energy barriers, and the blocking temperature corresponds to the temperature at which the exchange bias field goes to zero for the median energy barrier. The value of M$_r$ (the in-plane [Co/Pt] remanence) is set at RT and sets the scale for the coupling at the [Co/Pt]/NiO interface. As the in-plane remanence increases, the coupling energy at the [Co/Pt]/NiO interface, given by $J_1\vec{S}_F \bullet \vec{S}_{AF}$, increases the pinning of the AFM grains at this interface and stabilizing the grains against switching. Hence the effect of the increasing in-plane remanence (or alternatively H$_{set}$) is to shift the distribution of energy barriers to higher energies. At the Co/NiO interface the coupling is independent of M$_R$ and much larger than at the [Co/Pt]/NiO interface, since the entire Co moment lies in plane (by contrast, even at the highest achievable remanence, the in-plane value of M_R for the [Co/Pt] layer is only 26% of the saturation magnetization). Hence, the blocking temperature increases with M_R as seen in the inset to figure 7.6, since the median energy barrier is now shifted to higher energies.

In bulk NiO, the temperature dependence of the order parameter as well as the anisotropy constants [7.36] are well known. Isolated thin films of NiO exhibit a much reduced T_N [7.34], but this lower T_N may be enhanced by the presence of a FM [7.36] or ferrimagnetic [7.38] layer in close proximity. The temperature dependence of the in-plane anisotropy, even in bulk single crystals, goes to zero well below the bulk ordering temperature [7.36, 7.39], but the temperature dependence of the anisotropy constant in thin films remains unspecified. Given these uncertainties, it is difficult to give a quantitative estimate of the dependence of the blocking temperature on the in-plane remanence. In the simplest scenario, the additional pinning energy is merely proportional to M_R, shifting the median energy barrier. However, since the AFM anisotropy constant and the coupling energy both change substantially over this large temperature range, a quanitative relationship is too complicated to ascertain.

7.4 Conclusion

The isothermally tunable loops shifts in Co/NiO/[Co/Pt] heterostructures exhibit training effects arising from the relaxation of the NiO domain state towards equilibrium. The existence of a loop shift can be ascribed to the presence of the pinning of AFM domain walls by the normally out-of-plane [Co/Pt] layer. Application of an in-plane field results in a controllable value for the in-plane remanence of the [Co/Pt], which strongly affects the attainable blocking temperature and training effects.

The blocking temperature of 225 K, observed for very low set fields, is related to the large difference in anisotropy constants parallel and perpendicular to the ordered planes in AFM NiO, in conjunction with the presence of an out-of-plane pinning layer [7.20]. In this configuration, the blocking temperature is scaled by the larger out-of-plane anisotropy constant of the NiO, rather than the very small in-plane anisotropy constant. In contrast, the set field dependence (or in-plane [Co/Pt] remanence dependence) of the blocking temperature requires only the manipulation of the in-plane component of a pinning layer. The dependence of the in-plane remanence of the pinning layer on external field will set the scale for the field dependence of the blocking temperature, which ranges from 225 to 389K in this particular heterostructure. Hence, it is advantageous to have the pinning layer easy axis perpendicular to the easy axis of the exchange biased layer. This arrangement may be used to extend the blocking temperature range of any thin AFM and the sensitivity of the blocking temperature to an applied field will depend on the slope of the hard axis loop of the pinning layer. The higher the slope, the greater the enhancement of blocking temperature with set field. This effect is most effective at small thicknesses of the AFM. As the thickness of the AFM increases, the effect of the pinning layer will decrease and at some critical thickness close to the thickness of a domain wall, the pinning of the backside domains in the AFM become irrelevant. Above this thickness the pinning layer remanence will have no effect on the exchange bias.

Along with the manipulation of the blocking temperature, the large training effects observed for each series (both dependent on temperature and set field) have been successfully modeled by considering the relaxation of the AFM surface magnetization according to the discretized LK theory. The presence of the [Co/Pt] stack has a negligible influence on the training behavior, implying that training is purely due to interfacial spins at the Co/NiO interface and that the bulk of the AFM has little to no effect on the training.

With a suitable choice of materials, one can optimize the exchange bias effects needed for a particular application. To increase the low field blocking temperature requires a sandwich of two FM layers with perpendicularly directed anisotropies, coupled to an AFM with highly different in-plane and out-of-plane anisotropies, as is the case in NiO. In contrast, the field controlled blocking temperature requires the presence of magnetic layers with perpendicularly directed anisotropies, but without the requirements of a highly anisotropic AFM. The in-plane magnetization versus applied field slope of the pinning FM will determine the sensitivity of the blocking temperature on H_{set}, and the value of the magnetization will determine the range of blocking temperatures attainable. A variety of materials optimized heterostructures will allow for improved isothermal control of exchange bias effects.

The ability to control both the blocking temperature of an exchanged biased heterostructure as well as the ability to isothermally tune the loop shift may play a large role in future spin-valve devices, where the pinning properties of the hard layer are of great importance. A thorough knowledge of the training effects in these magnetic systems is essential to account for the fundamental relaxation mechanisms that occur with repeated field cycling.

7.5 Acknowledgements

This work was supported by NSF MRSEC DMR-0213808 and 0820521.

7.6 References

7.1. W. H. Meiklejohn and C. P. Bean, Phys. Rev. **105**, 904 (1957).

7.2. J. Nogués and I. K. Schuller, J. Magn. Magn. Mater. **192**, 203 (1999).

7.3. G. A. Prinz, Science 282, 1660 (1998).

7.4. S. S. P. Parkin, K. P. Roche, M. G. Samant, P. M. Rice, R. B. Beyers, R. E. Scheuerlein, E. J. O'Sullivan, S. L. Brown, J. Bucchigano, D. W. Abraham, Y. Lu, M. Rooks, P. L. Trouilloud, R. A. Wanner, and W. J. Gallagher, J. Appl. Phys. 85, 5828 (1999).

7.5. S. A. Wolf, Science 294, 1488 (2001).

7.6. A. E. Berkowitz and K. Takano, J. Magn. Magn. Mater. **200**, 552 (1999).

7.7. A. Hoffmann, Phys. Rev. Lett. **93**, 097203 (2004).

7.8. D. Suess, M. Kirschner, T. Schrefl, J. Fidler, R. Stamps, and J.-V. Kim, Phys. Rev. B **67**, 054419 (2003).

7.9. F. Dorfbauer, D. Suess, J. McCord, M. Kirschner, T. Schrefl, and J. Fidler, J. Magn. Magn. Mater. **290–291**, 754 (2005).

7.10. K. Zhang, T. Zhao, and H. Fujiwara, J. Appl. Phys. **89**, 6910 (2001).

7.11. C. Binek, Phys. Rev. B **70**, 014421 (2004).

7.12. F. Radu, M. Etzkorn, R. Siebrecht, T. Schmitte, K. Westerhold, and H. Zabel, Phys. Rev. B **67**, 134409 (2003).

7.13. T. Hauet, J. Borchers, P. Mangin, Y. Henry, and S. Mangin, Phys. Rev. Lett. **96**, 067207 (2006).

7.14. D. Paccard, C. Schlenker, O. Massenet, R. Montmory, and A. Yelon, Phys. Status Solidi **16**, 301 (1966).

7.15. A. Hochstrat, C. Binek, and W. Kleemann, Phys. Rev. B **66**, 092409 (2002).

7.16. S. G. E. teVelthuis, A. Berger, G. P. Felcher, B. K. Hill, and E. D. Dahlberg, J. Appl. Phys. **87**, 5046 (2000).

7.17. W. T. Lee, S. G. E. teVelthuis, G. P. Felcher, F. Klose, T. Gredig, and E. D. Dahlberg, Phys. Rev. B **65**, 224417 (2002).

7.18. P. Miltényi, M. Gierlings, J. Keller, B. Beschoten, G. Güntherodt, U. Nowak, and K. D. Usadel, Phys. Rev. Lett. **84**, 4224 (2000).

7.19. Christian Binek, Xi He, and Srinivas Polisetty, Phys. Rev. B **72**, 054408 (2005).

7.20. A. Baruth and S. Adenwalla, Phys. Rev. B **78**, 174407 (2008).

7.21. M. Gruyters, J. Magn. Magn. Mater. **248**, 248 (2002).

7.22. M. T. Hutchings and E. J. Samuelsen, Phys. Rev. B **6**, 3447 (1972).

7.23. M.G. Blamire et al PRL, 98, 217202 (2007)

7.24. Note that these samples A and B are the same as samples C and A, respectively, of ref. 20.

7.25. J. Keller, P. Miltényi, B. Beschoten, G. Güntherodt, U. Nowak, and K. D. Usadel, Phys. Rev. B **66**, 014431 (2002).

7.26. C. H. Lai, H. Matsuyama, R. L. White, T. C. Anthony, and G. G. Bush, J. Appl. Phys. **79**, 6389 (1996).

7.27. H. Xi, R. M. White, S. Mao, Z. Gao, Z. Yang, and E. Murdock, Phys. Rev. B **64**, 184416 (2001).

7.28. H. Y. Li, L. Y. Chen, and S. M. Zhou, J. Appl. Phys. **91**, 2243 (2002).

7.29. J. Dho, C. W. Leung, and M. G. Blamire, J. Appl. Phys. **99**, 033910 (2006).

7.30. L. E. Fernandez-Outon, G. Vallejo-Fernandez, S. Manzoor, and K. O’Grady, J. Magn. Magn. Mater. **303**, 296 (2006).

7.31. K. Takano, Ph.D. thesis, Physics Department, University of California at San Diego, San Diego, CA (1998).

7.32. Z. Y. Liu and S. Adenwalla, Phys. Rev. Lett. **91**, 037207 (2003).

7.33. Z. Y. Liu and S. Adenwalla, J. Appl. Phys. **94**, 1105 (2003).

7.34. D. Alders, L.H. Tjeng, F.C. Voogt, T. Hibma, G.A. Sawatzky, C.T. Chen, J. Vogel, M. Sacchi and S. Iacobucci, Phys. Rev. B **57**, 11623 (1998).

7.35. B. Craig, R. Lamberton, A. Johnston, U. Nowak, R. W. Chantrell, and K. O'Grady, J. Appl. Phys., **103**, 07C102 (2008).

7.36. K. Kurosawa, M. Miura and S. Saito, J. Phys. C: Solid St. Phys. **13**, 1521 (1980).

7.37. A. Baruth, D. J. Keavney, J. D. Burton, K. Janicka, E. Y. Tsymbal, L. Yuan, S. H. Liou, and S. Adenwalla, Phys. Rev. B **74**, 054419 (2006).

7.38. P.J. van der Zaag, Y. Ijiri, J.A. Borchers, L.F. Feiner, R.M. Wolf, J.M. Gaines, R.W. Erwin, and M.A. Verheijen, Phys. Rev. Lett. **84**, 6102 (2000).

7.39. Antoine Barbier, Cristian Mocuta, Wolfgang Neubeck, Mattia Mulazzi, Flora Yakhou, Karine Chesnel, Albéric Sollier, Christian Vettier, and François de Bergevin, Phys. Rev. Lett. **93**, 257208 (2004).

This chapter is based on the submitted paper: *Temperature and set field dependence of exchange bias training effects in Co/NiO/[Co/Pt] heterostructures with orthogonal easy axes,* A. Baruth and S. Adenwalla, Phys. Rev. B (2009).

Selected Presentations

Excitation and Study of Magnetization Dynamics in Patterned Thin Films Using Surface Acoustic Waves

March Meeting of the American Physical Society, Pittsburgh, Pennsylvania

March 16th – 20th, 2009

Exchange Coupling at Co/NiO Interfaces: The Origin of Interlayer Exchange Coupling

Invited speaker to University of Minnesota, Materials Research Science and Engineering Seminar, Minneapolis, Minnesota

February 10th, 2009

Isothermal tuning of exchange bias and blocking temperature enhancement in Co/NiO/[Co/Pt] structures with orthogonal easy axes

2008 University of Nebraska Research Fair

* Winner: Graduate Student Research Competition Prize

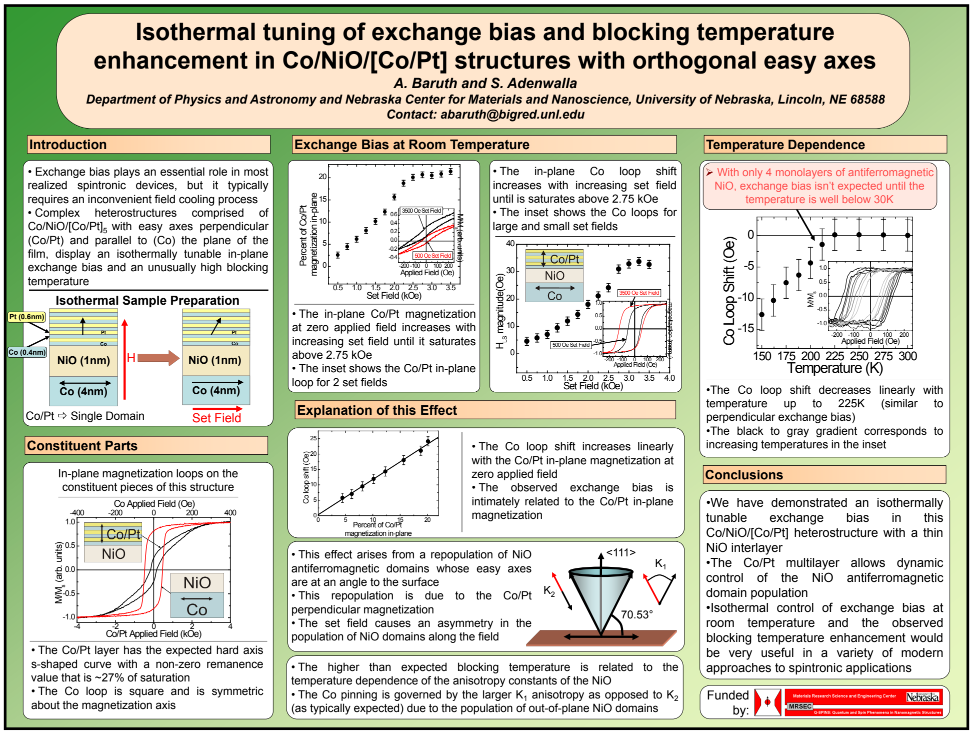

Isothermal tuning of exchange bias and blocking temperature enhancement in Co/NiO/[Co/Pt] structures with orthogonal easy axes

A. Baruth and S. Adenwalla

Department of Physics and Astronomy and Nebraska Center for Materials and Nanoscience, University of Nebraska, Lincoln, NE 68588

Contact: abaruth@bigred.unl.edu

Introduction

- Exchange bias plays an essential role in most realized spintronic devices, but it typically requires an inconvenient field cooling process
- Complex heterostructures comprised of Co/NiO/[Co/Pt]$_5$ with easy axes perpendicular (Co/Pt) and parallel to (Co) the plane of the film, display an isothermally tunable in-plane exchange bias and an unusually high blocking temperature

Isothermal Sample Preparation

Co/Pt ⇨ Single Domain

Set Field

Constituent Parts

In-plane magnetization loops on the constituent pieces of this structure

- The Co/Pt layer has the expected hard axis s-shaped curve with a non-zero remanence value that is ~27% of saturation
- The Co loop is square and is symmetric about the magnetization axis

Exchange Bias at Room Temperature

- The in-plane Co/Pt magnetization at zero applied field increases with increasing set field until it saturates above 2.75 kOe
- The inset shows the Co/Pt in-plane loop for 2 set fields

- The in-plane Co loop shift increases with increasing set field until is saturates above 2.75 kOe
- The inset shows the Co loops for large and small set fields

Explanation of this Effect

- The Co loop shift increases linearly with the Co/Pt in-plane magnetization at zero applied field
- The observed exchange bias is intimately related to the Co/Pt in-plane magnetization

- This effect arises from a repopulation of NiO antiferromagnetic domains whose easy axes are at an angle to the surface
- This repopulation is due to the Co/Pt perpendicular magnetization
- The set field causes an asymmetry in the population of NiO domains along the field

- The higher than expected blocking temperature is related to the temperature dependence of the anisotropy constants of the NiO
- The Co pinning is governed by the larger K_1 anisotropy as opposed to K_2 (as typically expected) due to the population of out-of-plane NiO domains

Temperature Dependence

➢ With only 4 monolayers of antiferromagnetic NiO, exchange bias isn't expected until the temperature is well below 30K

- The Co loop shift decreases linearly with temperature up to 225K (similar to perpendicular exchange bias)
- The black to gray gradient corresponds to increasing temperatures in the inset

Conclusions

- We have demonstrated an isothermally tunable exchange bias in this Co/NiO/[Co/Pt] heterostructure with a thin NiO interlayer
- The Co/Pt multilayer allows dynamic control of the NiO antiferromagnetic domain population
- Isothermal control of exchange bias at room temperature and the observed blocking temperature enhancement would be very useful in a variety of modern approaches to spintronic applications

Funded by: Materials Research Science and Engineering Center MRSEC Nebraska Q-SPINS: Quantum and Spin Phenomena in Nanomagnetic Structures

Domain overlap in antiferromagnetically coupled [Co/Pt]/NiO/[Co/Pt] multilayers.

52nd Conference on Magnetism and Magnetic Materials, Tampa, Florida

November 5th – 9th, 2007

Domain overlap in antiferromagnetically coupled [Co/Pt]/NiO/[Co/Pt] multilayers

2007 University of Nebraska Research Fair

* Winner: Graduate Student Research Competition Prize

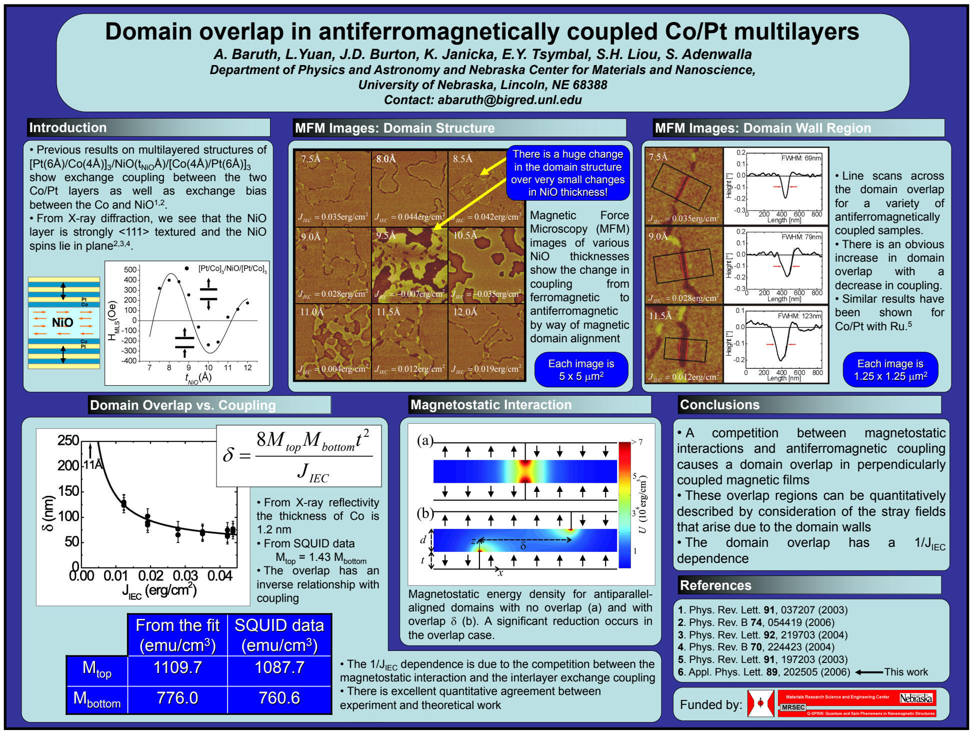

Domain overlap in antiferromagnetically coupled Co/Pt multilayers

A. Baruth, L.Yuan, J.D. Burton, K. Janicka, E.Y. Tsymbal, S.H. Liou, S. Adenwalla
Department of Physics and Astronomy and Nebraska Center for Materials and Nanoscience,
University of Nebraska, Lincoln, NE 68388
Contact: abaruth@bigred.unl.edu

Introduction

- Previous results on multilayered structures of $[Pt(6Å)/Co(4Å)]_3/NiO(t_{NiO}Å)/[Co(4Å)/Pt(6Å)]_3$ show exchange coupling between the two Co/Pt layers as well as exchange bias between the Co and NiO[1,2].
- From X-ray diffraction, we see that the NiO layer is strongly <111> textured and the NiO spins lie in plane[2,3,4].

MFM Images: Domain Structure

There is a huge change in the domain structure over very small changes in NiO thickness!

Magnetic Force Microscopy (MFM) images of various NiO thicknesses show the change in coupling from ferromagnetic to antiferromagnetic by way of magnetic domain alignment

Each image is 5 x 5 μm²

MFM Images: Domain Wall Region

- Line scans across the domain overlap for a variety of antiferromagnetically coupled samples.
- There is an obvious increase in domain overlap with a decrease in coupling.
- Similar results have been shown for Co/Pt with Ru.[5]

Each image is 1.25 x 1.25 μm²

Domain Overlap vs. Coupling

$$\delta = \frac{8 M_{top} M_{bottom} t^2}{J_{IEC}}$$

- From X-ray reflectivity the thickness of Co is 1.2 nm
- From SQUID data $M_{top} = 1.43\, M_{bottom}$
- The overlap has an inverse relationship with coupling

	From the fit (emu/cm³)	SQUID data (emu/cm³)
M_{top}	1109.7	1087.7
M_{bottom}	776.0	760.6

Magnetostatic Interaction

Magnetostatic energy density for antiparallel-aligned domains with no overlap (a) and with overlap δ (b). A significant reduction occurs in the overlap case.

- The $1/J_{IEC}$ dependence is due to the competition between the magnetostatic interaction and the interlayer exchange coupling
- There is excellent quantitative agreement between experiment and theoretical work

Conclusions

- A competition between magnetostatic interactions and antiferromagnetic coupling causes a domain overlap in perpendicularly coupled magnetic films
- These overlap regions can be quantitatively described by consideration of the stray fields that arise due to the domain walls
- The domain overlap has a $1/J_{IEC}$ dependence

References

1. Phys. Rev. Lett. **91**, 037207 (2003)
2. Phys. Rev. B **74**, 054419 (2006)
3. Phys. Rev. Lett. **92**, 219703 (2004)
4. Phys. Rev. B **70**, 224423 (2004)
5. Phys. Rev. Lett. **91**, 197203 (2003)
6. Appl. Phys. Lett. **89**, 202505 (2006) ⟵ This work

Funded by: Materials Research Science and Engineering Center MRSEC Nebraska Q-SPINS: Quantum and Spin Phenomena in Nanomagnetic Structures

Domain overlap in antiferromagnetically coupled [Co/Pt]/NiO/[Co/Pt] multilayers

March Meeting of the American Physical Society, Denver, Colorado

March 5th – 9th, 2007

Magnetic coupling and training effects in Co/NiO/[Co/Pt] structures with orthogonal easy axes

March Meeting of the American Physical Society, Denver, Colorado

March 5th – 9th, 2007

Effects of coupling on domain structure of [Pt(6Å)/Co(4Å)]$_3$/NiO(t$_{NiO}$)/ [Co(4Å)/Pt(6 Å)]$_3$ multilayers with oscillatory coupling

March Meeting of the American Physical Society**,** Baltimore, Maryland

March 13th – 17th, 2006

Oscillatory Coupled Multilayers with a NiO interlayer

Guest speaker at the Advanced Photon Source User Science Seminar, Argonne National Laboratory, Argonne, Illinois

April 13th, 2005

XMCD studies of antiferromagnetically coupled Co/Pt Multilayers

March Meeting of the American Physical Society, Los Angeles, California

March 20th – 25th, 2005

XMCD studies of antiferromagnetically coupled Co/Pt Multilayers

49th Conference on Magnetism and Magnetic Materials, Jacksonville, Florida

November 7th – 12th, 2004

Publications

Temperature and set field dependence of exchange bias training effects in Co/NiO/[Co/Pt] heterostructures with orthogonal easy axes

A. Baruth and S. Adenwalla, submitted to Phys. Rev. B (2009).

Domain size and structure in exchange-coupled [Co/Pt]/NiO/[Co/Pt] multilayers

A. Baruth, S.H. Liou and S. Adenwalla, to be submitted to Appl. Phys. Lett. (2009).

Enhanced blocking temperature and isothermal control of hysteresis loop shifts in Co/NiO/[Co/Pt] heterostructures with orthogonal easy axes

A. Baruth and S. Adenwalla, Phys. Rev. B **78**, 174407 (2008).

Citations: 0 (04/21/09)

Domain overlap in antiferromagnetically coupled [Co/Pt]/NiO[Co/Pt] multilayers

A. Baruth, L. Yuan, J. D. Burton, K. Janicka, E.Y. Tsymbal, S.H. Liou and S. Adenwalla, Appl. Phys. Lett. **89**, 202505 (2006).

Citations: 13 (04/21/09)

Origin of the interlayer exchange coupling in [Co/Pt]/NiO[Co/Pt] multilayers studied with XAS, XMCD, and micromagnetic modeling

A. Baruth, D.J. Keavney, J. D. Burton, K. Janicka, E.Y. Tsymbal, L. Yuan, S.H. Liou and S. Adenwalla, Phys. Rev. B **74**, 054419 (2006).

Citations: 10 (04/21/09)